

# The Fabrication of Thermoelectric Materials Using Functionalised Silicon Nanoparticles



**Shane Ashby**

School of Chemistry

University of East Anglia

Norwich

UK

**2015**

A thesis submitted in partial fulfilment of the requirements for the degree of Doctor of Philosophy of the University of East Anglia.

© This copy of the thesis has been supplied on condition that anyone who consults it is understood to recognise that its copyright rests with the author and that use of any information derived there from must be in accordance with current UK Copyright Law. In addition, any quotation or extract must include full attribution.



---

## **Declaration**

I declare that the work contained in this thesis submitted for the degree of Doctor of Philosophy is my work, except where due reference is made to other authors, and has not previously been submitted by me for a degree at this or any other universities.

**Shane Ashby**

---

## Acknowledgements

Firstly I would like to thank Dr Yimin Chao for his guidance and support and the opportunity to work within his lab. I would also like to thank him for the opportunities he has offered me throughout study.

I would also like to thank my colleges past and present Dr Paul Coxon, Dr Qi Wang, Dr Jayshree Ahire, Rouxi Lui, Frederik Huld, Jason Thomas, Mehrnaz Behray, Tiezheng Bian, Ting Li and Huang Zhen for their hospitality, guidance and friendship.

Thanks to Elliot Lawrence for proof-reading, support and friendship.

In addition I would like to thank all collaborators at NEXUS, Diamond Beamline (B11), MAXlab (Beamline I011), as well as Rick Bryson (TEM, University of Leeds), Tom Pennycook (SuperSTEM, Darsbury), Jorge García-Cañadas and Min Gao (Electrical and Seebeck Coefficient measurement), Huanpo Ning and Michael J Reece (Queen Mary, University of London, Thermal diffusivity measurement), Antony V. Powell (University of Reading, Thermal conductivity measurements).

I would also like to express my gratitude to Professor Hualong Xu and his group for their hospitality and support during my time at Fudan University.

Thank you to my family and friends, especially my wife who has encouraged and supported me throughout.

Finally I would like to thank European Thermodynamics Ltd. and EPSRC for funding.



---

## Abstract

Silicon nanoparticles (SiNPs) can be synthesised by a variety of methods. A one-pot synthesis based on the chemical reduction of inverse micelles has been used to produce SiNPs with ligands of varying alkyl chain length. These particles were characterised to determine how the chain length affects the surface functionalities and particle size. The particles produced show optical properties typical of SiNPs produced by solution methods.

Silicon based materials are a potential alternative to current thermoelectric materials (e.g.  $\text{Bi}_2\text{Te}_3$ ) due to their abundance and low toxicity. Phenylacetylene functionalised SiNPs have been synthesised using a bottom up approach. A cold pressed pellet of this material displays an electrical conductivity of  $18.1 \text{ S m}^{-1}$ , in addition to a high Seebeck coefficient and a low thermal conductivity. These properties combine to give a figure of merit (ZT) of 0.6 at 300 K. This ZT value is significant for a silicon based material, and comparable to that of other thermoelectric materials such as  $\text{Mg}_2\text{Si}$ ,  $\text{PbTe}$  and Si-Ge alloy.

To investigate the effects that the doping of ligands have on the thermoelectric properties of such materials, terthiophene functionalised SiNPs were synthesised and subsequently doped using varying levels of  $\text{NOBF}_4$ . The electrical resistivity shows a decrease of 7 orders of magnitude between the undoped and optimised material although the electrical resistivity is still higher than required for application. In addition, the material produced displays a modest ZT of 0.08.

Top down methods allow control of the carrier concentration of the silicon core, as the material is doped prior to being broken down. Phenylacetylene SiNPs were synthesised using electrochemical etching followed by functionalisation via a two-step chlorination-alkylation process. These particles were characterised and their thermal stability analysed, showing a maximum operation temperature of  $200^\circ\text{C}$ .

---

## Table of contents

Declaration.....	I
Acknowledgements .....	II
Abstract.....	III
Table of contents .....	IV
List of Figures .....	VIII
List of Schemes .....	XIII
List of tables.....	XIV
List of Abbreviations .....	XV
Chapter 1: Introduction.....	1
1.1. Introduction.....	2
1.2. Nanomaterials .....	3
1.2.1. Nanosheets.....	3
1.2.2. Nanowires and Nanorods .....	4
1.2.3. Nanotubes .....	5
1.2.4. Nanoparticles.....	6
1.2.5. Nanostructured Materials .....	7
1.3. Semiconductor Nanoparticles .....	7
1.3.1. Quantum confinement .....	7
1.4. Silicon Nanoparticles .....	8
1.4.1. Methods of Synthesis .....	9
1.4.2. Surface Functionality and Passivation .....	13
1.5. Thermoelectric Effect .....	19
1.5.1. Seebeck Effect.....	19
1.5.2. Peltier Effect .....	20
1.5.3. Thompson effect.....	21

---

1.5.4. Kelvin Relationships .....	21
1.6. Thermoelectric materials.....	21
1.6.1. Power Factor and Figure of Merit (ZT).....	22
1.6.2. Thermal Conductivity and Phonon Scattering .....	22
1.7. Materials .....	23
1.7.1. Bi <sub>2</sub> Te <sub>3</sub> .....	23
1.7.2. Skutlerudite.....	24
1.7.3. Silicides.....	24
1.7.4. Silicon .....	24
1.7.5. Polymers.....	26
1.7.6. Organic-Inorganic Nanocomposites.....	27
1.8. Thesis Overview .....	28
<b>Chapter 2: Methods and Materials .....</b>	<b>31</b>
2.1. Materials .....	32
2.2. Synthetic Procedures .....	32
2.2.1. One-Pot Synthesis of Alkyl Functionalised SiNPs.....	32
2.2.2. Bottom Up Synthesis of Phenylacetylene Functionalised SiNPs.....	33
2.2.3. Bottom Up Synthesis of Terthiophene Functionalised SiNPs.....	34
2.2.4. Top Down approach to Phenylacetylene Functionalised SiNPs.....	36
2.3. Characterisation Techniques .....	37
2.3.1. Chemical Analysis.....	37
2.3.2. Microscopy.....	41
2.3.3. Optical Properties .....	41
2.4. Thermal Analysis and Measurement of Thermoelectric Properties.....	43
2.4.1. Thermal Gravimetric Analysis and Differential Scanning Calorimetry.....	43
2.4.2. Measurement of Thermoelectric Properties .....	43
<b>Chapter 3: One-Pot Bottom Up Synthesis of Alkyl Functionalised Silicon Nanoparticles by Micelle Reduction.....</b>	<b>47</b>

---

3.1. Overview.....	48
3.2. Synthesis of Alkyl Functionalised SiNPs.....	48
3.3. Characterisation of Alkyl Functionalised SiNPs.....	49
3.3.1. Studies of Functionalisation, Oxidation and Incomplete Capping.....	49
3.3.2. Microscopy and Particle Size.....	55
3.3.3. XPS and XAS.....	58
3.4. Optical properties of SiNPs.....	62
3.4.1. Quantum yield.....	64
3.5. Thermal Stability.....	66
3.6. Summary.....	67
<b>Chapter 4: Solution Synthesis of Phenylacetylene Functionalised SiNPs for</b>	
<b>Thermoelectric Applications.....</b>	<b>69</b>
4.1. Overview.....	70
4.2. Synthesis of phenylacetylene Functionalised SiNPs.....	71
4.3. Characterisation of Phenylacetylene Functionalised SiNPs.....	71
4.3.1. FTIR and NMR.....	71
4.3.2. Microscopy.....	73
4.3.3. EDX and XPS.....	75
4.4. Thermal Stability.....	79
4.5. Thermoelectric Measurements.....	80
4.4.1. Electrical Resistivity.....	81
4.4.2. Seebeck Coefficient.....	82
4.4.3. Thermal Conductivity.....	83
4.6. Summary.....	83
<b>Chapter 5: Effects of Ligand Doping on the Thermoelectric Properties of</b>	
<b>Terthiophene Functionalised Silicon Nanoparticles.....</b>	<b>85</b>
5.1. Overview.....	86
5.2. Synthesis of Terthiophene Functionalised SiNPs.....	86

---

5.3. Characterisation of Undoped Terthiophene Functionalised SiNPs.....	87
5.4. Thermal Stability .....	92
5.5. Doping of Terthiophene Functionalised SiNPs.....	93
5.6. Thermoelectric Measurements.....	95
5.6.1. Electrical Conductivity.....	95
5.6.2. Aging of Electrical Conductivity .....	96
5.6.3. Seebeck Coefficient and Power factor .....	97
5.6.4. Thermal Conductivity.....	98
5.6.5. Figure of Merit .....	100
5.7. Summary .....	101
<b>Chapter 6: Electrochemical Etching Approach to the Synthesis of Phenylacetylene Functionalised Silicon Nanoparticles .....</b>	<b>103</b>
6.1. Overview .....	104
6.2. Synthesis of Phenylacetylene Functionalised SiNPs .....	104
6.3. Characterisation of Phenylacetylene Functionalised SiNPs.....	105
6.5. Summary .....	113
<b>Chapter 7: Conclusions and Future Work .....</b>	<b>115</b>
7.1. Conclusions .....	116
7.2. Future Work.....	118
7.2.1. Doping SiNPs .....	118
7.2.2. Ligands and Surface Coverage .....	118
7.2.3. Theoretical Understanding .....	120
<b>References .....</b>	<b>121</b>

---

## List of Figures

Figure 1: a) The Lycugus Cup out of light b) When held to the light. ....	2
Figure 2: STM image ( $1000 \times 1000 \text{ \AA}^2$ ) showing the formation of a graphitic structure on a metal surface; the image was obtained at room temperature after annealing ethylene over Pt (111) at 1230 K. <sup>13</sup> .....	3
Figure 3: Cross-sectional SEM of an electrochemically etched Si nanowire array. <sup>31</sup> .....	4
Figure 4: TEM images of shape-separated 18 aspect ratio gold nanorods. <sup>33</sup> .....	5
Figure 5: SEM images of palladium nanotubes generated by reacting silver nanowires with aqueous $\text{Pd}(\text{NO}_3)_2$ solutions. The nanotubes were broken via sonication for a few minutes to expose their cross-sections. <sup>34</sup> .....	6
Figure 6: Schematic energy diagrams showing the difference between the energy electronic states of bulk semiconductor, semiconductor QDs and molecular species. ....	8
Figure 7: Schematic diagram showing the closed loop used in Thomas Johann's Seebeck experiment. ....	19
Figure 8: Schematic diagram showing a circuit connected to a battery with 2 junctions between two different materials used by Peltier. ....	20
Figure 9: Bright-field TEM image of a section of holey silicon ribbon. The porosity is estimated as $\sim 35\%$ through the entire ribbon. Selected area electron diffraction pattern (inset) indicates its single crystalline nature. <sup>156</sup> .....	26
Figure 10: Annotated photograph of electrochemical etching set up. ....	36
Figure 11: Schematic diagram of processes occurring during EDX. ....	38
Figure 12: Schematic diagram of processes occurring during XPS. ....	39
Figure 13: Schematic diagram showing the hot probe experimental setup. ....	44
Figure 14: Photograph of multifunctional electrical resistivity/ Seebeck coefficient measurement apparatus. <sup>179</sup> .....	45
Figure 15: FTIR of hexyl, octyl, dodecyl and octadecyl functionalised SiNPs when methanol was used as a quenching agent. ....	50
Figure 16: FTIR of hexyl, octyl, dodecyl and octadecyl functionalised SiNPs when ethanol was used as a quenching agent. ....	51
Figure 17: Aging of FTIR spectrum of dodecyl functionalised SiNPs showing Si-H stretch showing the initial and after 7 days spectrum. ....	52
Figure 18: FTIR of dodecyl and octadecyl functionalised SiNPs before and after thermal hydrosilylation with the corresponding 1-alkene. ....	53
Figure 19: $^1\text{H-NMR}$ spectrum obtained from octyl-functionalised SiNPs dissolved in $\text{CDCl}_3$ . ....	54
Figure 20: $^1\text{H-NMR}$ spectrum obtained from dodecyl-functionalised SiNPs dissolved in $\text{CDCl}_3$ . ....	55

Figure 21: Low resolution TEM image showing a)hexyl b)octyl c) dodecyl d)octadecyl functionalised SiNPs synthesised by micelle reduction. ....	56
Figure 22: SuperSTEM image showing the distribution of sizes of alkyl-functionalised SiNPs obtained from the reduction of hexyltrichlorosilane/SiCl <sub>4</sub> micelles, inset: high resolution Z-contrast STEM image of an individual SiNP showing it to be crystalline of alkyl-functionalised SiNPs.....	57
Figure 23: Histogram showing an example size distribution of alkyl-functionalised SiNPs.....	58
Figure 24: XPS spectra obtained from dodecyl functionalised SiNPs showing survey spectrum. Photoelectron spectrum was collected with incident photon energy of 630 eV. ....	59
Figure 25 : High resolution spectrum XPS spectrum obtained from dodecyl functionalised SiNPs showing Si2p region. Photoelectron spectrum was collected with incident photon energy of 630 eV.....	59
Figure 26: High resolution spectrum XPS spectrum obtained from dodecyl functionalised SiNPs showing C1s region. Photoelectron spectrum was collected with incident photon energy of 630 eV.....	60
Figure 27: High resolution spectrum XPS spectrum obtained from dodecyl- functionalised SiNPs showing O1s region. Photoelectron spectrum was collected with incident photon energy of 630 eV.....	61
Figure 28: TEY for thick film of dodecyl-functionalised SiNPs over the Si L absorption edge. The spectrum region from 97–104 eV is overlaid and scaled x 10 .....	62
Figure 29: PL spectra for alkyl functionalised SiNPs. Excitation spectrum (Emission wavelength = 400nm, emission bandwidth = 10nm, excitation bandwidth = 10nm) Black and emission spectrum (excitation wavelength = 340 nm emission bandwidth = 10nm, excitation bandwidth = 10nm) Green .....	63
Figure 30: UV/Vis Spectrum for alkyl- functionalised SiNPs in hexane. ....	63
Figure 31: UV/Vis spectra at varying dilutions of alkyl functionalised SiNPs in hexane .....	64
Figure 32: Emission spectrum; Excitation wavelength = 340 nm excitation bandwidth = 10 nm emission bandwidth = 2.5 nm at varying concentration of alkyl functionalised SiNPs in hexane .....	65
Figure 33: Plotted integrated intensity of emission against absorbance for both alkyl functionalised SiNPs in hexane and quinine sulphate in 0.1 M H <sub>2</sub> SO <sub>4</sub> .....	65
Figure 34: TGA and derivative of dodecyl functionalised SiNPs between 50 and 550 °C at a heating rate of 20 °Cmin <sup>-1</sup> .....	67
Figure 35: FTIR spectrum of phenylacetylene functionalised SiNPs.....	72
Figure 36: <sup>1</sup> H-NMR of phenylacetylene functionalised SiNPs.....	73
Figure 37: <sup>13</sup> C-NMR of phenylacetylene functionalised SiNPs.....	73

---

Figure 38: TEM image and size distribution of phenylacetylene functionalised SiNPs . Inset, size distribution of silicon nanoparticle.....	74
Figure 39: EDX of phenylacetylene functionalised SiNPs. ....	75
Figure 40: XPS survey spectrum for phenylacetylene functionalised SiNPs. Photoelectron spectrum was collected with incident photon energy of 1486.6 eV. ....	76
Figure 41: XPS spectra obtained for phenylacetylene functionalised SiNPs showing high resolution spectrum of Si2p region. Photoelectron spectrum was collected with incident photon energy of 1486.6 eV.....	77
Figure 42: XPS spectra obtained for phenylacetylene functionalised SiNPs showing high resolution spectrum of C1s region. Photoelectron spectrum was collected with incident photon energy of 1486.6 eV.....	78
Figure 43: XPS spectra obtained for phenylacetylene functionalised SiNPs showing high resolution spectrum of O1s region. Photoelectron spectrum was collected with incident photon energy of 1486.6 eV.....	78
Figure 44: TGA and derivative of phenylacetylene functionalised SiNPs.....	79
Figure 45: DSC of phenylacetylene functionalised SiNPs. ....	80
Figure 46: Electrical conductivity measurements of a pellet of phenylacetylene functionalised SiNPs at room temperature initial and after a month.....	81
Figure 47: Seebeck coefficient measurements of a pellet of phenylacetylene functionalised SiNPs at room temperature initial and after a month.....	82
Figure 48: FTIR of terthiophene functionalised SiNPs. ....	88
Figure 49: TEM micrograph of terthiophene functionalised SiNPs.....	88
Figure 50: EDX spectrum of undoped terthiophene functionalised SiNPS.....	89
Figure 51: XPS survey spectrum obtained from undoped terthiophene functionalised SiNPs. Photoelectron spectrum was collected with incident photon energy of 1486.6 eV.....	90
Figure 52: High resolution XPS spectrum obtained from undoped terthiophene functionalised SiNPs showing Si2p region. Photoelectron spectrum was collected with incident photon energy of 1486.6 eV.....	91
Figure 53: High resolution XPS spectrum obtained from undoped terthiophene functionalised SiNPs showing C1s region. Photoelectron spectrum was collected with incident photon energy of 1486.6 eV.....	92
Figure 54: TGA curve and first derivative for terthiophene functionalised SiNPs.....	93
Figure 55: DSC curve of terthiophene functionalised SiNPs.....	93
Figure 56: EDX spectrum of doped terthiophene functionalised SiNPS.....	94



---

Figure 57: XPS survey spectrum obtained from doped terthiophene functionalised SiNPs showing Survey spectrum. Photoelectron spectrum was collected with incident photon energy of 1486.6 eV. ....	95
Figure 58 : Electrical resistivity against doping ratio (Mass Terthiophene functionalised SiNPs/Mass NOBF4) .....	96
Figure 59: Electrical resistivity against time for the doping ratio of 0.4 and 0.5.....	97
Figure 60: Seebeck coefficient and power factor against doping ratio (Mass Terthiophene functionalised SiNPs/Mass NOBF4).....	98
Figure 61: Specific heat and thermal diffusivity against temperature for terthiophene functionalised SiNPs with a doping ratio of 0.5. ....	99
Figure 62: Temperature dependant thermal conductivity of a doped pellet of terthiophene functionalised SiNPs.....	100
Figure 63: ZT against doping ratio (Mass Terthiophene functionalised SiNPs/Mass NOBF4) .....	101
Figure 64: FTIR of phenylacetylene functionalised SiNPs synthesised by electrochemical etching. ....	106
Figure 65: <sup>1</sup> H-NMR of phenylacetylene functionalised SiNPs synthesised by electrochemical etching.....	106
Figure 66: <sup>13</sup> C-NMR of phenylacetylene functionalised SiNPs synthesised by electrochemical etching.....	107
Figure 67: <sup>31</sup> P-NMR of phenylacetylene functionalised SiNPs synthesised by electrochemical etching.....	108
Figure 68: XPS Survey Spectrum of top down phenylacetylene functionalised SiNPs synthesised by electrochemical etching. ....	109
Figure 69: XPS spectra obtained for phenylacetylene functionalised SiNPs showing high resolution spectrum of Si2p region. Photoelectron spectrum was collected with incident photon energy of 1486.6 eV. ....	110
Figure 70: XPS spectra obtained for phenylacetylene functionalised SiNPs showing high resolution spectrum of O1s region. Photoelectron spectrum was collected with incident photon energy of 1486.6 eV. ....	111
Figure 71: TEM image of phenylacetylene functionalised SiNPs synthesized by electrochemical etching. Inset histogram showing particle size distribution .....	112
Figure 72: TGA trace and derivative between 50 and 1000 °C for phenylacetylene functionalised SiNPs synthesized by electrochemical etching.....	113
Figure 73: DSC trace between 50 and 1000 °C for phenylacetylene functionalised SiNPs synthesized by electrochemical etching. ....	113

---

---

Figure 74: SiNPs functionalised with different monomers, a) thiophene b) aniline c)

ethylenedioxythiophene..... 119

---

## List of Schemes

Scheme 1: A typical synthesis of hydrogen terminated SiNPs using galvanostatic electrochemical etching.....	9
Scheme 2: Synthesis of hydrogen terminated SiNPs by reduction of SiCl <sub>4</sub> within an inverse micelle using a metal hydride reducing agent.....	10
Scheme 3: Synthesis of functionalised SiNPs by the reduction of SiCl <sub>4</sub> within an inverse micelle of and alkyltrichlorosilane using a LiAlH <sub>4</sub> reducing agent. ....	11
Scheme 4: Synthesis of chloride terminated SiNPs from the reduction of a micelle of tetrachlorosilane using a non-hydride reducing agent. ....	12
Scheme 5: Pyrolysis of diphenylsilane .....	12
Scheme 6: Laser induced pyrolysis of silane.....	13
Scheme 7: Thermolysis of silicon rich oxide .....	13
Scheme 8: Surface functionalisation of hydrogen and chloride terminated SiNPs <sup>107</sup> .....	15
Scheme 9: Mechanism for radical hydrosilylation. <sup>108</sup> .....	16
Scheme 10: Exciton mediated mechanism for the hydrosilylation of SiNPs <sup>108</sup> .....	17
Scheme 11: Metal complex catalysed hydrosilylation of SiNPs using Speier's catalyst. ....	18
Scheme 12: One pot micelle reduction synthesis of alkyl functionalised SiNPs.....	33
Scheme 13: Hydrosilylation of unreacted Si-H species on the surface of alkyl functionalised SiNPs. ....	33
Scheme 14: Synthesis of phenylacetylene functionalised SiNPs using a bottom up approach.....	34
Scheme 15: Synthesis of terthiophene. ....	35
Scheme 16: Synthesis of terthiophene functionalised SiNPs s using a bottom up approach. ....	35
Scheme 17: Oxidation/doping of terthiophene functionalised SiNPs using a bottom up approach. ....	36
Scheme 18: Functionalisation of hydrogen functionalised SiNPs using a chlorination- alkylation approach. ....	37
Scheme 19: One pot micelle reduction synthesis of alkyl functionalised SiNPs.....	49
Scheme 20: Synthesis of phenylacetylene functionalised SiNPs using a bottom up approach.....	71
Scheme 21: Synthesis of terthiophene functionalised SiNPs using a bottom up approach.....	87
Scheme 22: Functionalisation of hydrogen functionalised SiNPs using a chlorination- alkylation approach. ....	105
Scheme 23: Oxidative polymerisation on the surface of thiophene functionalised SiNPs.....	119

---

## List of tables

Table 1: The mean diameter and standard deviation of SiNPs from a sample of 100 particles. ....	56
Table 2: Thermoelectric measurements of a pellet of phenylacetylene functionalised SiNPs at room temperature. ....	81
Table 3: Seebeck coefficient measurements at different points on pellet .....	97

---

## List of Abbreviations

<b>ATR</b>	Attenuated Total Reflectance
<b>DNA</b>	Deoxyribonucleic Acid
<b>DSC</b>	Differential scanning Calorimetry
<b>EDX</b>	Energy dispersive x-ray spectroscopy
<b>FTIR</b>	Fourier Transform Infrared Spectroscopy
<b>HOMO</b>	Highest occupied molecular orbital
<b>LUMO</b>	Lowest unoccupied molecular orbital
<b>NC</b>	Nanocrystal
<b>NMR</b>	Nuclear magnetic resonance
<b>NP</b>	Nanoparticle
<b>P3HT</b>	Poly(3-hexylthiophene)
<b>PEDOT</b>	Poly(ethyldioxythiophene)
<b>PL</b>	Photoluminescence
<b>PSS</b>	Poly(styrene sulfanoate)
<b>PTFE</b>	Poly(tetrafluoroethylene)
<b>PVDF</b>	Poly (vinylidene fluoride)
<b>QD</b>	Quantum dot
<b>SINP</b>	Silicon Nanoparticle
<b>SuperSTEM</b>	Super Scanning tunnelling electron microscopy
<b>TEM</b>	Transmission electron microscopy
<b>TEY</b>	Total Electron yield
<b>TGA</b>	Thermogravimetric analysis
<b>UV/VIS</b>	Ultra-violet/ visible spectroscopy
<b>XANES</b>	X-ray absorption near edge spectroscopy
<b>XAS</b>	X-ray absorption spectroscopy
<b>XPS</b>	X-ray photoelectron spectroscopy
<b>ZT</b>	Figure of merit

---

# Chapter 1:

## Introduction

## 1.1. Introduction

The prefix *nano* is derived from the Greek word meaning dwarf and in science *nano* means one billionth of or a factor of  $10^{-9}$ . Nanoscience and nanotechnologies deal with materials which possess at least one dimension in the nanoscale. Despite this fundamental similarity nanoscience and nanotechnology are different; this can be seen from the formal definitions of each of these terms:

**Nanoscience** - *The study of phenomena and manipulation of materials at atomic, molecular and macromolecular scales, where properties differ significantly from those at a larger scale.*<sup>1</sup>

**Nanotechnology** - *The design, characterisation, production and application of structures, devices and systems by controlling shape and size at nanometer scale.*<sup>1</sup>

**Nanochemistry** – *The utilisation of chemistry to make nanoscale building blocks of different size shape, composition and surface structure, charge, and functionality.”*<sup>2</sup>

Although historical artefacts such as ‘The Lycugus Cup’(Figure 1)) show use of nanoscience and nanotechnology as far back as 1000 years ago, nanoscience and nanotechnology are relatively new areas of science.



**Figure 1: a) The Lycugus Cup out of light b) When held to the light.**

The movement toward conceptual understanding started with underpinning of the concept in a lecture by Richard Feymann entitled “There’s plenty of room at the bottom”.<sup>3, 4</sup> Where he eluded to the idea of being able to manipulate matter on an atomic scale. Initially he tried to visualise this using the idea of being able to write the entire 24 volumes of the Encyclopaedia Britannica on the head of a needle.<sup>4</sup>



In the past 30 years nanoscience and nanotechnology have come to the forefront of scientific research as a result of the development of the first scanning tunnelling microscope (STM) by Gerd Binnig and Heinrich Rohrer of IBM Zurich in the early 1980s.<sup>5</sup> This key development allowed the direct observation of nanostructures. Since then nanomaterials have shown potential applications in a variety of different areas ranging from biomedicine to engineering.<sup>6-9</sup>

## 1.2. Nanomaterials

Nanomaterials are materials with at least one dimension or feature in the nanoscale. These materials take any number of forms, including materials which have 1, 2 or 3 dimensions in the nanoscale or bulk materials with features within them which show dimensions on the nanoscale, e.g. nanoporous materials.

### 1.2.1. Nanosheets

Nanosheets are a good example of a material with only a single dimension on the nanoscale. When considering the idea of nanosheets it is possible to think of them as a thin film of a material which is under a single micron thick. This is much thinner than the majority of commercial polymer films. Today these types of materials are of great research interest especially graphene,<sup>10</sup> silicene,<sup>11</sup> and phospharene.<sup>12</sup>

Initially synthesised in 2003 by Novoselov *et. al.*,<sup>10</sup> graphene is a hot topic in nanosheet type materials and Geim's original paper has become one of the most cited papers in materials science. Graphene is a layer of graphitic material which is a single atomic layer thick.

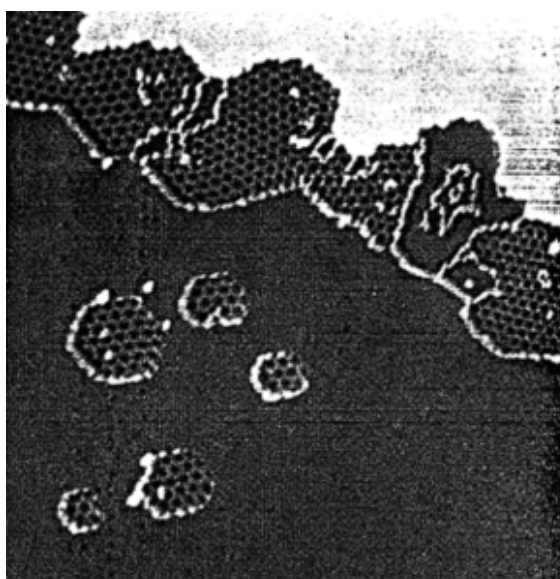


**Figure 2: STM image ( $1000 \times 1000 \text{ \AA}^2$ ) showing the formation of a graphitic structure on a metal surface; the image was obtained at room temperature after annealing ethylene over Pt**

**(111) at 1230 K.<sup>13</sup>**

Since its discovery there have been a high number of publications on its synthesis, isolation, properties and its potential applications.<sup>13-19</sup> Potential applications of graphene include; biosensors,<sup>15, 20, 21</sup> electronics,<sup>14</sup> photonics<sup>22</sup> and optoelectronics.<sup>18</sup>

**1.2.2. Nanowires and Nanorods**

Nanowires have two dimensions in the nanoscale, although nanowires can be less than 100 nm in length. These materials as suggested by the name have long wire-like shapes with a narrow diameter and a considerably longer length. Nanowires like many types of nanomaterial can be synthesised from a variety of different materials, from metals to organics. There are also examples of molecular nanowires such as DNA. Nanowires are currently of interest to the scientific community and a lot of current work in nanowires focuses on semiconductor nanowires, such as zinc oxide, silicon and indium phosphide.<sup>23-26</sup> These display some interesting size dependant properties such as diameter-dependant fluorescence.<sup>24</sup> Their potential applications range from electronics to biomedicine.<sup>27-30</sup>

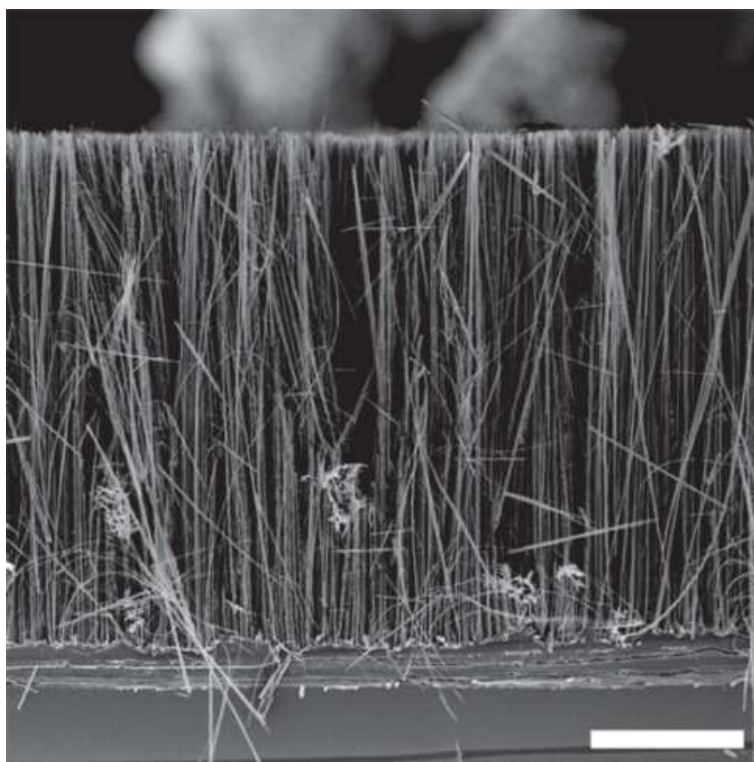


**Figure 3: Cross-sectional SEM of an electrochemically etched Si nanowire array.<sup>31</sup>**

Nanorods differ from nanowires in that they have all 3 dimensions on the nanoscale, although they still have a greater length than diameter as would be expected. The difference lies in the ratio between the length and the diameter being between 3 and 5. So if a rod has a diameter of 2 nm

then the rod should be between 6 and 10 nm in length. Just like nanowires these can be composed of a similarly wide variety of materials.<sup>30, 32</sup>

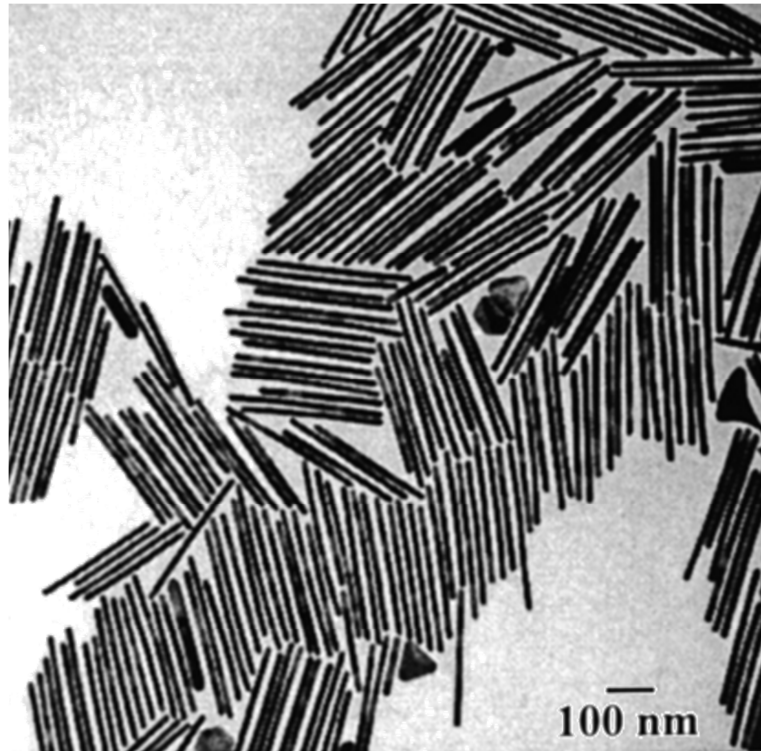


**Figure 4: TEM images of shape-separated 18 aspect ratio gold nanorods.<sup>33</sup>**

### 1.2.3. Nanotubes

Nanotubes are similar to nanowire except for one major difference in that as suggested by the name they are hollow. Nanotubes do however show similar dimensional characteristics generally displaying 2 dimensions in the nanoscale and having a diameter which is greatly exceeded by their length.

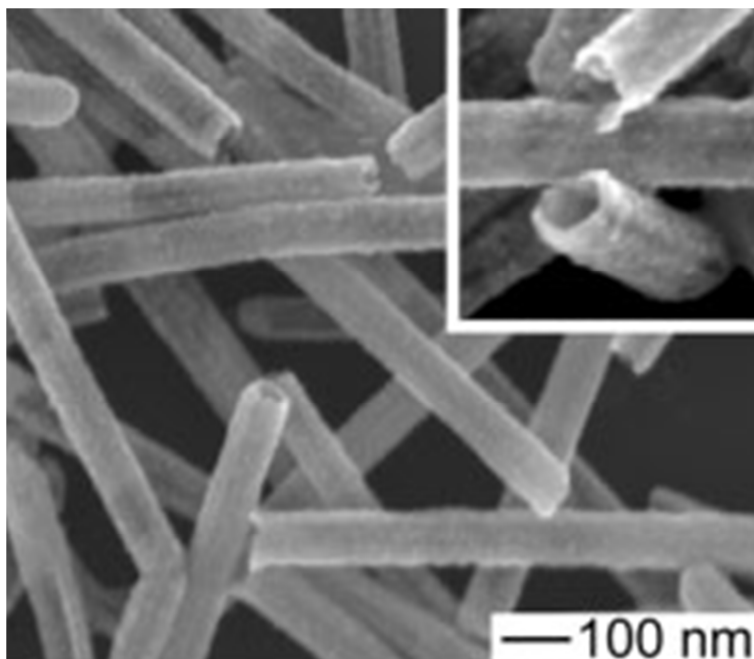


**Figure 5: SEM images of palladium nanotubes generated by reacting silver nanowires with aqueous  $\text{Pd}(\text{NO}_3)_2$  solutions. The nanotubes were broken via sonication for a few minutes to expose their cross-sections.<sup>34</sup>**

An important example of nanotubes is carbon nanotubes. These materials have been of great interest in the scientific community since the reported synthesis by Lijima *et. al.* in 1991.<sup>35</sup> This was not the first synthesis of carbon nanotubes, but this work initiated interest in the scientific community. Today carbon nanotubes have been applied in areas such as mechanical materials and photovoltaic devices.<sup>6, 36, 37</sup>

#### 1.2.4. Nanoparticles

Nanoparticles have 3 dimensions in the nanoscale. Depending on the nature of the material they may also be described as nanocrystals or quantum dots. The terms for each expression are given below:

**'Nanoparticle:** A cluster of atoms or molecules e.g. Si or  $\text{Fe}_2\text{O}_3$  with three dimensions in the nanoscale.'

**'Nanocrystal:** A cluster of atoms or molecules with 3 dimensions in the nanoscale in which the material is crystalline.'<sup>1</sup>

**'Quantum dot (QD):** A cluster of atoms or molecules (generally semiconductors) with 3 dimensions on the nanoscale where the dimensions are of a similar magnitude to the exciton Bohr radius of the material.'<sup>1</sup>

Nanoparticles like nanowires are widely documented for a wide range of materials from metals to polymers each possessing different properties and advantages suitable for different applications.<sup>9</sup>

31, 38-40

### 1.2.5. Nanostructured Materials

Nanostructured materials are more complicated than the other types of nanomaterials to clarify as they can vary greatly in form. A nanostructured material can be defined as:

*‘a bulk material which possesses an aspect of its structure with dimensions on the nanoscale’*

Some examples of nanostructured materials include; porous materials and nanostructured bulk materials i.e. bulk materials made up of Nano sized crystallites. In both cases this has led to the engineering of new materials or materials with very different properties to the bulk material.<sup>41-45</sup>

One example of a nanostructured material is porous silicon, this differs greatly from bulk silicon, most noticeably due to its visible photoluminescence and high surface area.<sup>43</sup>

## 1.3. Semiconductor Nanoparticles

As mentioned previously nanomaterials can be made up of a large range of different materials. One area of particular interest to the scientific community has been semiconductor nanoparticles. This research has generally been centred on semiconductor quantum dots.

Semiconductor quantum dots range from 2 to 20 nm in size depending on the material and display interesting size dependant optical, electronic and physical properties.<sup>46-49</sup> These properties stem from, the surface area to volume ratio and an effect known as the quantum confinement effect. As a result of this, semiconductor nanoparticles have found uses in applications ranging from photoelectronics to bioimaging.<sup>50 51, 52</sup>

### 1.3.1. Quantum confinement

A characteristic feature of semiconductor quantum dots is that their optical and electronic spectra greatly change with particle size. This is due to the quantum confinement effect.<sup>53</sup> This effect is well documented in many different semiconductor quantum dots.<sup>54-57</sup> One of the most simplistic explanations of this effect uses the “electron in the box model” or “potential well”.<sup>58</sup> Quantum confinement is essentially the reduction of the size of the box in 3 dimensions, which gives rise to discrete electronic levels rather than a continuous band as observed in the bulk material. Practically this means that a decrease in the particle size results in an increase in the energy gap between the valence and conduction band.<sup>59-61</sup> This is because as we decrease the size of the particle we increase the certainty of where the electrons are and as a result decrease the

certainty of its energy and/or crystal momentum. This is in agreement with the Heisenberg uncertainty principle.

$$\Delta x \Delta p \geq \frac{\hbar}{2} \quad (1)$$

In terms of the optical properties of semiconductor quantum dots this means that we observe discrete absorption bands and fluorescence. In the bulk material, a series of nearby transitions occur at slightly different energies whereas in QDs transitions are compressed to a single intense transition i.e. a discrete absorption band is observed.<sup>61</sup> In QDs the electron-hole pair produced is delocalised over the interior of the particle and the recombination of the electron and hole results in the emission of a photon which results in fluorescence. This effect is only efficient when the size of the QD is smaller than the exciton (electron-hole pair) Bohr radius.<sup>2, 62</sup>

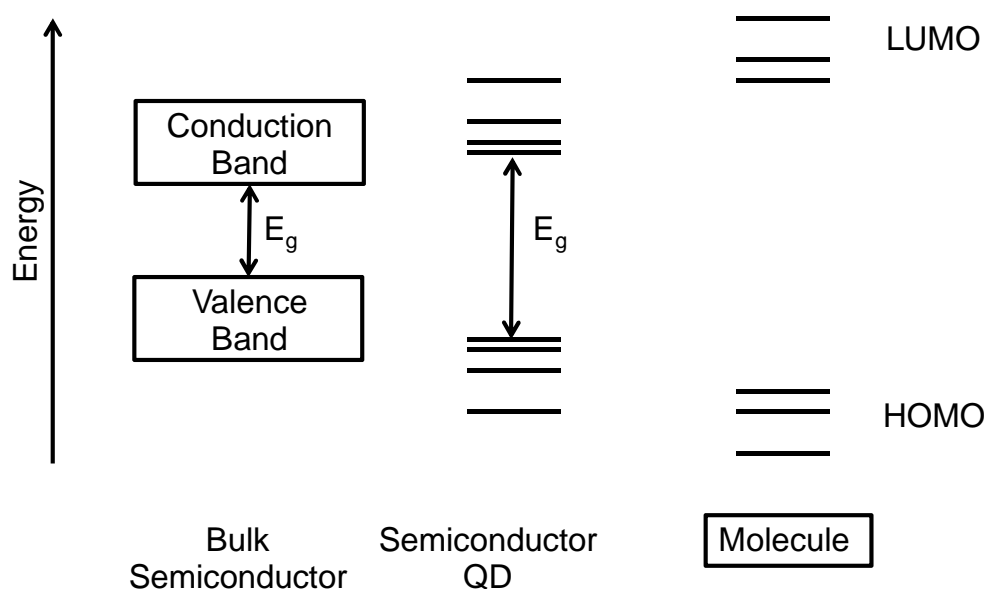


**Figure 6: Schematic energy diagrams showing the difference between the energy electronic states of bulk semiconductor, semiconductor QDs and molecular species.**

#### 1.4. Silicon Nanoparticles

Silicon is used as a primary building block in semiconductor electronics and as a result is widely available, and relatively cheap. Other advantages of silicon include its low toxicity and low environmental impact. These are major factors which have helped drive interest in the synthesis and application of silicon nanoparticles (SiNPs) over the past 20 years.<sup>63, 64</sup> Quantum confinement effects give SiNPs interesting optical, electronic and mechanical properties.<sup>46, 48, 49, 65-68</sup> These are responsible for their wide range of potential applications in electronics, photovoltaics, and bioimaging.<sup>69-75</sup> In addition to this they can be functionalised, which allows the tuning of some of

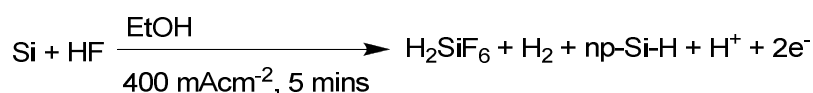
these properties so that they are better suited to the desired application, e.g. polar ligands for water solubility for introduction in to biological systems.<sup>41, 74, 76-79</sup>

#### 1.4.1. Methods of Synthesis

SiNPs can be synthesised by number of different methods. Generally physicochemical and electrochemical methods are utilised. Synthetic methods include; electrochemical etching, micelle reduction, pyrolysis of silane and steel ball milling, amongst others.

##### 1.4.1.1. Electrochemical Etching

Electrochemical etching is generally considered the most reliable way to produce hydrogen-terminated SiNPs.<sup>63</sup> A major reason for this is that they are prepared in HF and as a result the particles surfaces are usually highly hydrogen terminated, crystalline and contain low levels of surface oxide. The synthesis of particles by this method is made up of two steps; electrochemical etching to produce porous silicon followed by a fracturing process in a dry solvent to acquire H terminated SiNPs. Commonly the etching solution used contains a mixture of aqueous HF and ethanol in varying ratios. Typically a 1:1 ratio of 48% aqueous HF and ethanol is used.<sup>41, 80, 81</sup> A typical electrochemically etched particle is synthesised as follows:



**Scheme 1: A typical synthesis of hydrogen terminated SiNPs using galvanostatic electrochemical etching.**

The idea of breaking up porous silicon to produce SiNPs was originally put in to practice by Heinrich *et. al.* in 1992.<sup>80</sup> B-doped and P-doped wafers were etched at a current density between 0.1 to 5 mAcm<sup>-2</sup> for 1 or 6 hours in a HF bath, proceeded by an electropolishing step removing the nanostructured silicon from the surface of the wafer. These particles displayed a visible luminescence in the red region.

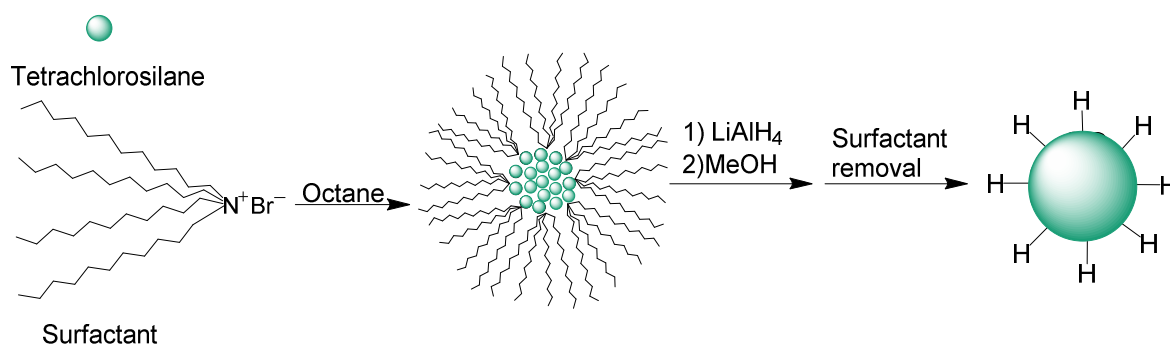
This new method attracted great interest and optimisation of this process was a hot topic during the mid to late 1990s, leading to improvements such as ultrasonic fracturing as opposed to electrochemical polishing to remove the particles from the electrochemically-etched wafer. Bley *et. al.*<sup>82, 83</sup> in 1996, conducted an informative study into the effect of a number of factors on both the optical and physical properties of the resulting particles. This included varying the composition of the HF etching solution, current density, etching time and sonication time. Their study offered better understanding of how to control electrochemical etching to optimise the desired properties of the particles. Later in 2002 Belomoin *et. al.*<sup>84</sup>, by varying the etching time and the current

density, were able to use electrochemical etching to obtain particles with average diameters of 1.0, 1.67, 2.15, and 2.9 nm showing resulting blue, green, yellow and orange luminescence respectively. This demonstrated the ability to achieve more precise control of the particle size using electrochemical methods.

Some recent incarnations of electrochemical etching are documented by Lie et. al. in 2002<sup>81</sup> and Chao et. al. in 2007<sup>85</sup> and 2011<sup>76</sup> showing a method for electrochemical etching which uses a 1:1 mixture of 48% aqueous HF and ethanol as etching solution. The etching solution is placed over silicon wafer in a cell and a current density of 210 – 550 mAcm<sup>-2</sup> is passed through a silicon wafer in a specially designed PTFE cell. This is followed by removal of solvent *in vacuo* and ultra-sonication for 10 mins in dry solvent to give hydrogen terminated SiNPs, ranging from 2-10 nm in size. These methods give hydrogen terminated SiNPs using a synthetic method that uses a low etching time, high current density, and a low sonication time.

#### 1.4.1.2. Micelle Reduction

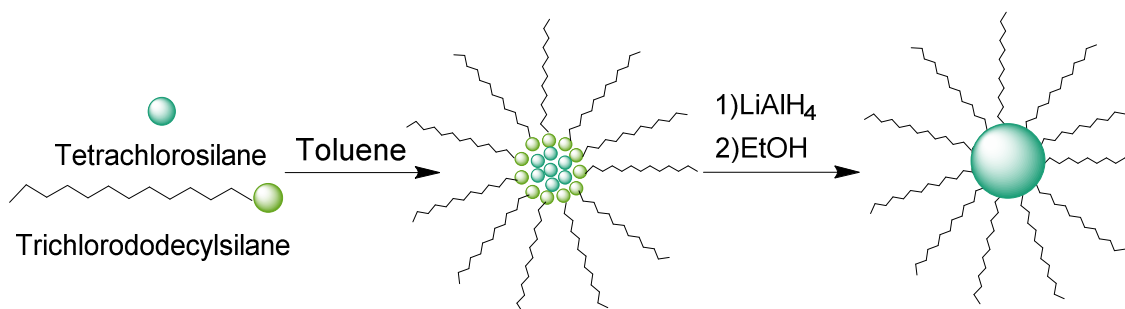
Micelle reduction is a relatively mild chemical - based method for the synthesis of SiNPs. This involves the reduction of micelles of a silicon based precursor (e.g. SiCl<sub>4</sub> or SiBr<sub>4</sub>) using a suitable reducing agent, such as LiAlH<sub>4</sub>, magnesium silicide or sodium phenylacetylide.<sup>78, 86-88</sup> The nature of the reducing agent used has a direct effect on the termination of the silicon nanoparticle produced. This method was first documented by Wilcoxon *et. al.* in 1998 who, based on previous inverse micelle work on gold nanoparticles, produced a method using anhydrous metal hydrides such as LiAlH<sub>4</sub> as a chemical reducing agent to reduce SiX<sub>4</sub> (where X=Cl, Br or I) contained in micelles of non-ionic aliphatic polyethers, or alternatively quaternary ammonium cationic surfactants, to produce hydrogen-terminated SiNPs.<sup>89</sup> This method has been used widely with very few changes in reagents. Such methods have been followed up by functionalisation of the surface, generally using hydrosilylation reactions to introduce Si-C links to the surface.<sup>78 90</sup>



**Scheme 2: Synthesis of hydrogen terminated SiNPs by reduction of SiCl<sub>4</sub> within an inverse micelle using a metal hydride reducing agent.**



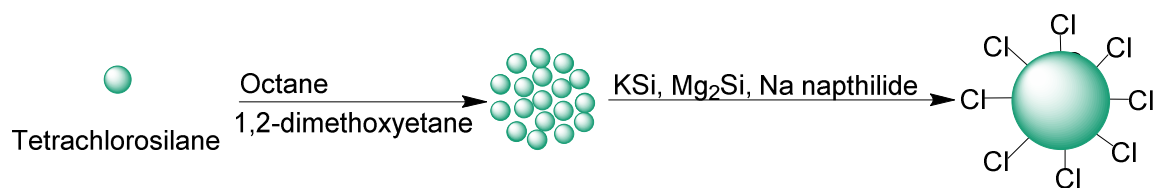
A later method using a metal hydride reducing agent, reported by Wang *et. al.*, bypassed the hydrogen terminated particles by using a  $\text{RSiCl}_3$  based surfactant, where  $\text{R} = \text{C}_6\text{H}_{13}$ .<sup>91</sup> This then becomes part of the particle as well as behaving as a surfactant, resulting in R terminated SiNPs. This method was investigated further using different surfactants including trichlorododecylsilane, trichlorooctylsilane, trichlorooctadecylsilane and trichlorophenylsilane showing the use of this method to yield SiNPs of different and potentially more useful functionality.<sup>92</sup>



**Scheme 3: Synthesis of functionalised SiNPs by the reduction of  $\text{SiCl}_4$  within an inverse micelle of and alkyltrichlorosilane using a  $\text{LiAlH}_4$  reducing agent.**

One issue with such methods is that they produce high levels of surface oxide which can be attributed to the step in which  $\text{LiAlH}_4$  is quenched, where the reaction of the alcohol with some of the available H functionalities on the surface of the particle causes oxidation or alkoxylation of the particle surface. Successful methods of avoiding this have been developed by using  $\text{CuCl}_2$  to quench the  $\text{LiAlH}_4$  but these methods require a more extensive purification procedure than the alcohol quenched reactions.<sup>93</sup>

Another micelle reduction method developed in the early 2000's uses non-hydride reducing agents which produce halide-terminated particles, rather than H-terminated particles. This area has been pioneered by Kauzlarich and co-workers by reducing micelles of  $\text{SiCl}_4$  in 1,2-dimethoxyethane using various non-hydride reducing agents such as  $\text{Mg}_2\text{Si}$ ,  $\text{KSi}$  or sodium naphthalide to give chloride-terminated particles.<sup>86-88, 94</sup> These surfaces are more reactive and are open to a wider variety of surface chemistry compared to hydrogen-terminated particles; as a result these surfaces can undergo nucleophilic substitutions with reagents such as primary alcohols and organometallic nucleophiles.<sup>87, 88, 95, 96</sup>



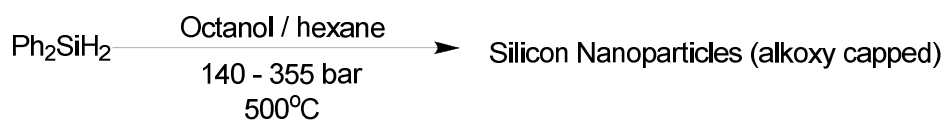
**Scheme 4: Synthesis of chloride terminated SiNPs from the reduction of a micelle of tetrachlorosilane using a non-hydride reducing agent.**

Another more recent method uses even more facile conditions. This synthesis reported by Wang *et. al.* in 2013 uses sodium ascorbate as a reducing agent to reduce aminopropyltriethoxysilane in water at ambient conditions to give water soluble amine terminated SiNPs with an average diameter of 1.5 nm in water.<sup>91</sup>

#### 1.4.1.3. Pyrolysis and Thermolysis

The decomposition of both liquid and gas precursors are an attractive synthetic approach to the synthesis of SiNPs. However the decomposition of gas phase precursors has been the most successful of these approaches.<sup>97</sup> One of the major drawbacks of using liquid precursors is their high decomposition temperature and the susceptibility of the particle surface to react with other solvent borne impurities.

In 2001 Korgel *et. al.* reported an effective method for producing SiNPs *via* the thermal decomposition of a liquid precursor. Diphenylsilane was thermally decomposed in a supercritical solvent mixture of octan-1-ol and hexane at a temperature of 500°C and pressure of 140-345 bar resulting in alkoxy functionalised SiNPs.<sup>98</sup> Additionally a level of size control was also achieved, by varying the octanol:Si ratio, suggesting that octanol acted both as a functionalising and a quenching agent (**Scheme 6**).<sup>99</sup>



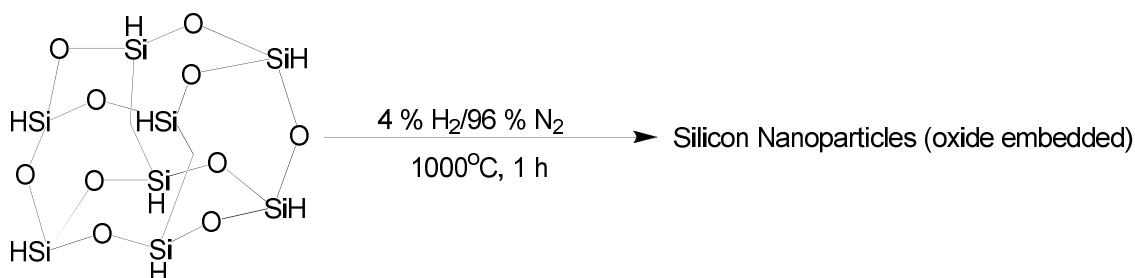
**Scheme 5: Pyrolysis of diphenylsilane**

CO<sub>2</sub> laser-induced decomposition of silane as developed by Li *et. al.* is one of many examples of a synthetic procedure using a gaseous precursor molecule. This procedure shows the potential to be an efficient method of producing large quantities of SiNPs, with reported production rates as high as 200 mg h<sup>-1</sup>, producing particles of approximately 5 nm diameter (**Scheme 6**).<sup>100, 101</sup>



**Scheme 6: Laser induced pyrolysis of silane**

Recently, decomposition of solid precursors such as silicon rich oxides and hydrogen silsesquioxane has been reported as another method for the synthesis of SiQDs.<sup>102, 103</sup> SiQDS can be generated from the pyrolytic decomposition of hydrogen silsesquioxane or other silicon rich oxides by heating at 1000°C in a reductive atmosphere (5% H<sub>2</sub> 95% N<sub>2</sub>) followed by HF etching (**Scheme 7**) to remove silicon oxide.<sup>102, 103</sup>



**Scheme 7: Thermolysis of silicon rich oxide**

#### 1.4.1.4. Ball Milling

Ball milling is a mechanical method by which silicon particles can be ground down in to smaller particles. Typically this method does not produce small quantum dots like the above methods but larger particles in the range of 40 to 800 nm, which contain smaller crystallites within.<sup>104</sup> These particles are still in the range of nanometers but generally do not display the properties that are typically associated with quantum confinement effects; e.g. photoluminescence. However in 2007 work by Heintz *et. al.* showed that it is possible to produce particles which exhibit quantum size effects by using ball milling in tandem with a primary alkene or alkyne base medium. This reacts with the freshly fractured surfaces preventing agglomeration. They observed an average crystal size of 5-10 nm and photoluminescence at 450 nm.<sup>105</sup>

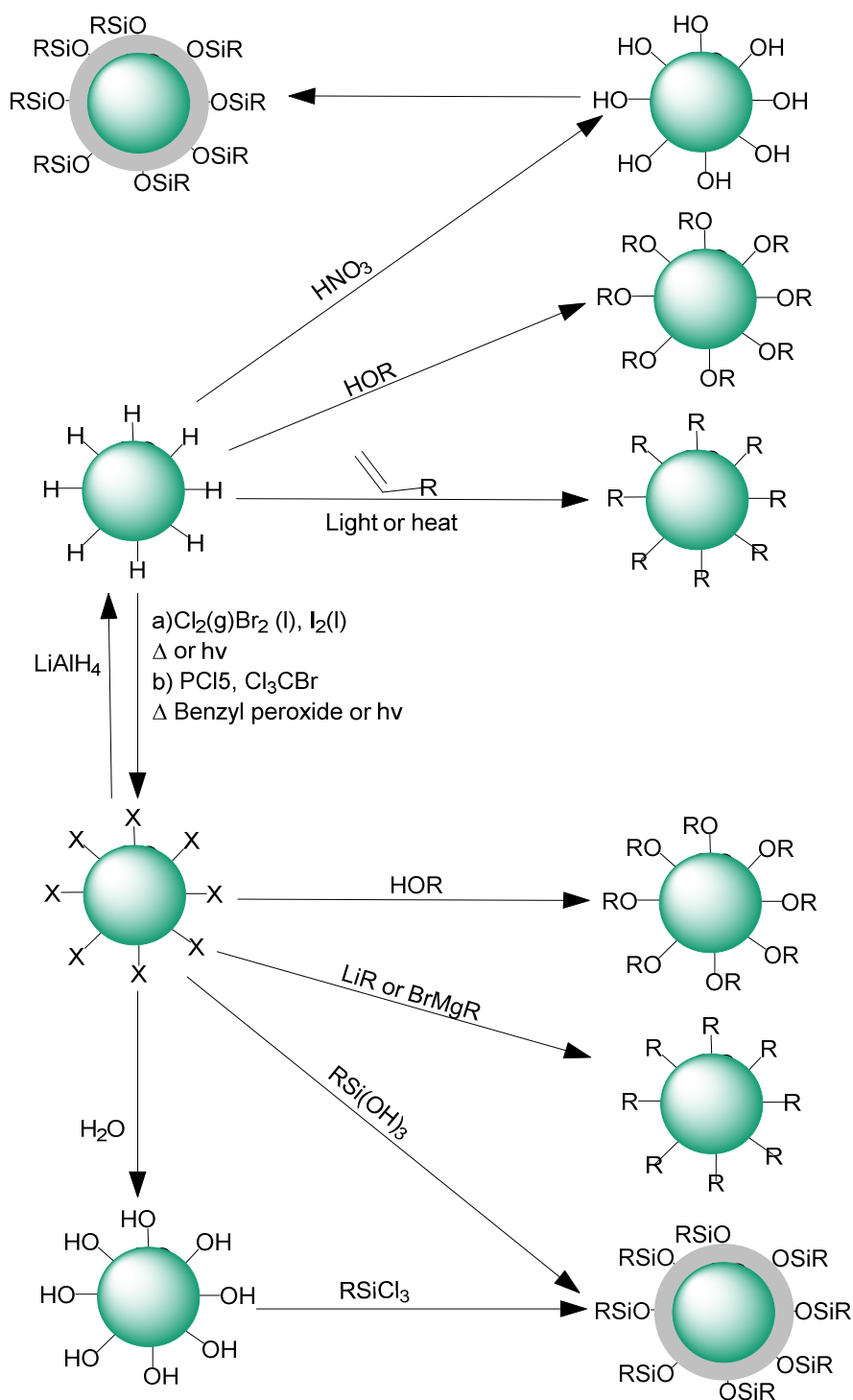
#### 1.4.2. Surface Functionality and Passivation

Generally SiNPs produced by the above methods yield hydrogen terminated surfaces and these surfaces are very sensitive to oxidation, as are chloride terminated surfaces. In many cases a surface with a minimal level of oxidation is desired as the presence of surface oxide can alter the optical properties quite significantly. This is usually indicated by a blue shift in the emission

spectrum. This is particularly an issue for bioimaging applications, where emitters in the orange region are more desirable. One way in which passivation of the surface can be achieved is by the introduction of covalently-bound carbon species.<sup>49, 81</sup>

In addition to the passivation of the particle surface it can be advantageous to functionalise a particle in a way that will alter the way in which it behaves. This is particularly key in obtaining water solubility, introducing more complex functionalization and increasing surface reactivity to particular reagents.<sup>73, 75, 106</sup>

The types of surface functionalisation for SiNPs are wide and varied ranging from alkylation reaction, based on hydrosilylation to radical halogenation. In some micelle reduction methods the surface passivation can be determined prior to particle synthesis by altering the surfactants used. A summary of some methods of functionalization can be seen in **Scheme 8**.

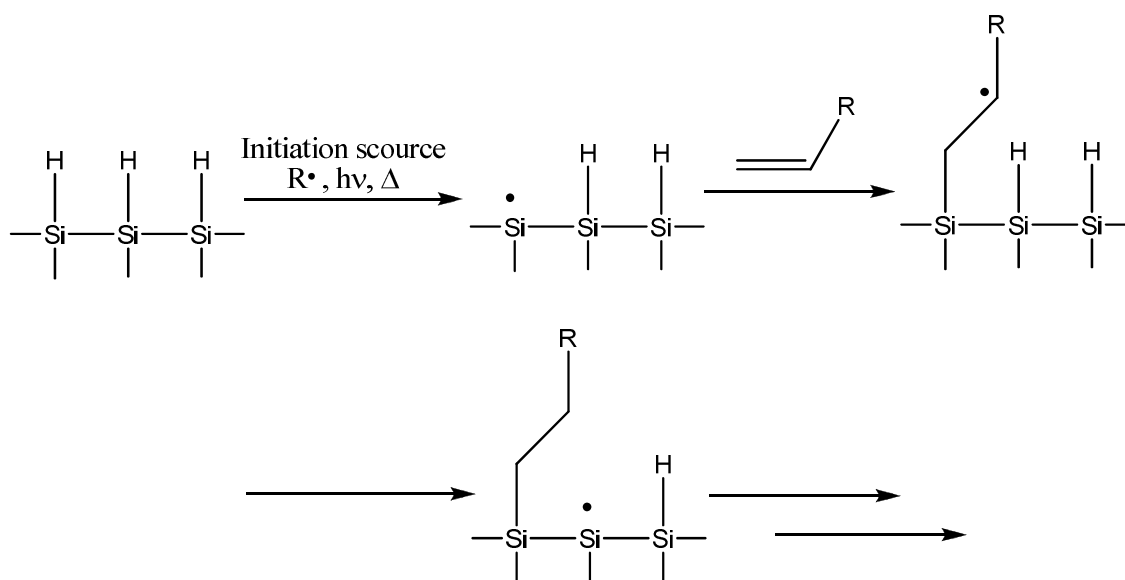


**Scheme 8: Surface functionalisation of hydrogen and chloride terminated SiNPs<sup>107</sup>**

From hydrogen terminated SiNPs the most common functionalization method uses hydrosilylation. This process is initiated by one of four methods; initiation using radical initiator (benzoyl peroxide), thermal initiation, photo initiation and metal complex catalysed (Speier's catalyst).<sup>81, 108 75, 109</sup>

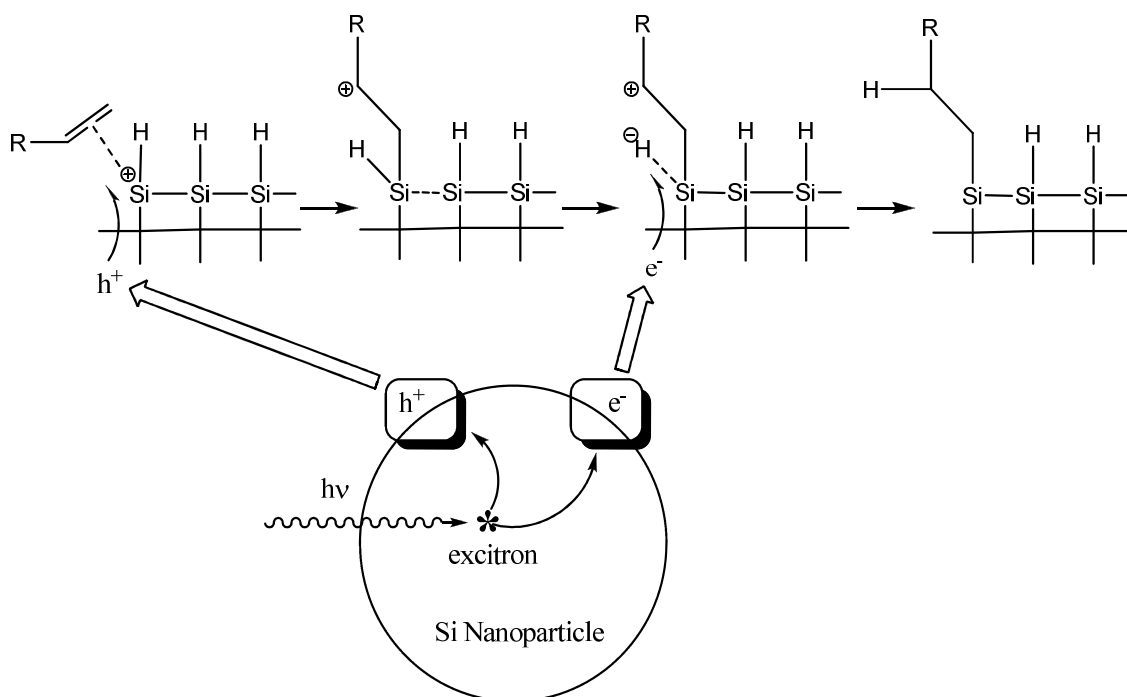
When performing hydrosilylation using a radical initiator, such as benzyl peroxide, either heat or light is used to homolytically split the initiator to generate radicals. These go on to react with hydrogen on the surface of the particle forming a radical site on the silicon surface, this site is then able to react directly with an alkene as shown. This terminates by picking up hydrogen from a neighbouring silicon atom (**Scheme 9**).<sup>108</sup>

The thermally-initiated hydrosilylation is a well-documented method for the functionalization of hydrogen terminated SiNPs. This method is usually carried out in a solvent with a boiling point higher than 100°C such as toluene, which is heated at reflux for several hours with a primary alkene of the desired chain length, to yield alkyl functionalized SiNPs. The mechanism by which this process occurs is still contested, but it is thought that the mechanism is also radical based as shown in **Scheme 9**.<sup>81, {Chao, 2007 #87, 85, 85, 90</sup>



**Scheme 9: Mechanism for radical hydrosilylation.**<sup>108</sup>

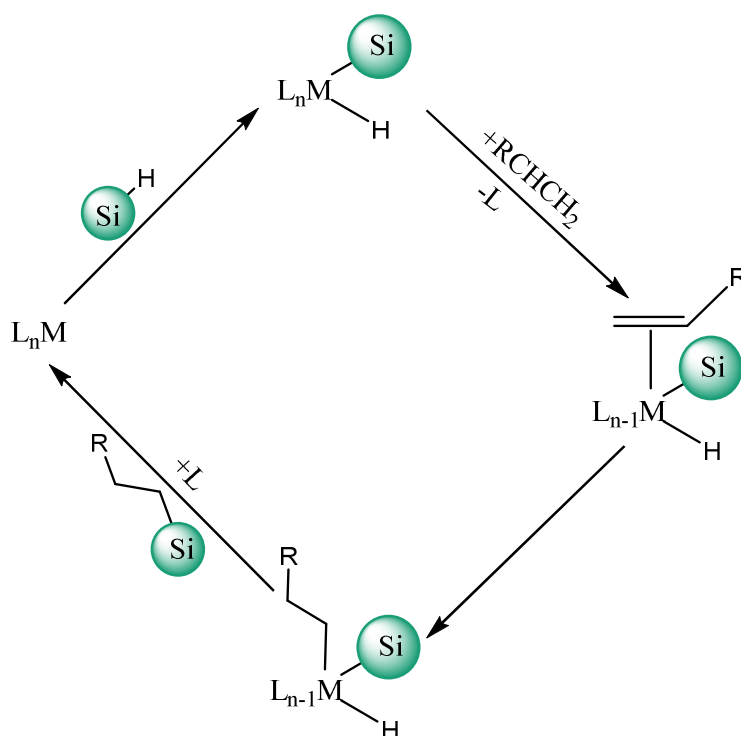
Photoinitiated hydrosilylation reactions can be initiated by UV or white light. Both methods use an intense light source to initiate the reaction. However due to the difference in energy of the photon from each light source the mechanisms for reaction varies slightly from one another.



**Scheme 10: Exciton mediated mechanism for the hydrosilylation of SiNPs**<sup>108</sup>

The UV initiated mechanism proceeds by radical initiation as shown in **Scheme 9**. Alternatively the white light initiated reaction is thought to proceed via an exciton mediated mechanism (**Scheme 10**).

The metal complex catalysed hydrosilylation uses Speier's catalyst ( $\text{H}_2\text{PtCl}_6$ ) and is proposed to proceed through the catalytic cycle shown in **Scheme 11**.



**Scheme 11: Metal complex catalyzed hydrosilylation of SiNPs using Speier's catalyst.**

One drawback with hydrosilylation reactions is that some molecules such as phenylacetylene and other conjugated alkynes, once attached, are able to quench the reactive states.<sup>110</sup> This limits the achievable coverage of the surface and limits the variety of molecules that can be effectively attached using this type of method. However even when using 1-alkenes the surface coverage achieved is modest.<sup>111, 112</sup>

There are two methods in which the potential functionalities attached to the particles can be broadened. One method would be the attachment of a reactive functional group such as an amine or cyanate, which can then go on to react with other molecules to alter the functionality.<sup>31</sup> The other method is to make the surface more reactive using halogenation or by producing halogen terminated particles.<sup>113, 114</sup>

Halogen terminated SiNPs can be synthesised directly by micelle reduction<sup>86-88</sup> or produced from hydrogen terminated particles.<sup>113, 115</sup> Halogenation of hydrogen terminated particles uses a halogenated reagent or solvent such as  $PCl_5$  in chlorobenzene or trichlorobromomethane in the presence of UV light or a radical initiator and heat resulting in more reactive halogenated surfaces. These surfaces can react with a number of nucleophiles such as organolithium/magnesium reagents, primary alcohols and amines. This is a useful reaction as it greatly broadens the variety of functional molecules that can be attached to the surface of these particles.



## 1.5. Thermoelectric Effect

The thermoelectric effect is the effect that allows the production of a voltage directly from a temperature gradient and also the development of a temperature gradient from a voltage. This concept can be manipulated by a range of different devices including temperature sensors, temperature measurement devices and electronic generation.<sup>116</sup> This effect is the combination of three thermodynamically reversible effects the Seebeck effect, the Peltier effect and the Thomson effect.<sup>117</sup>

### 1.5.1. Seebeck Effect

The Seebeck effect is the conversion of a temperature gradient into an electrical potential. It is named after the German physicist Thomas Johann Seebeck, who observed the movement of a compass needle when it was placed in the vicinity of a closed loop of two metals at different temperatures. He described this purely as a magnetic effect called thermomagnetism.<sup>118</sup> However it was observed by a Danish physicist Hans Christian Ørsted that this was an electromagnetic process as a consequence of the production of a potential difference/ voltage.<sup>119</sup> The kind of closed loop used by Seebeck is shown in **Figure 7**.

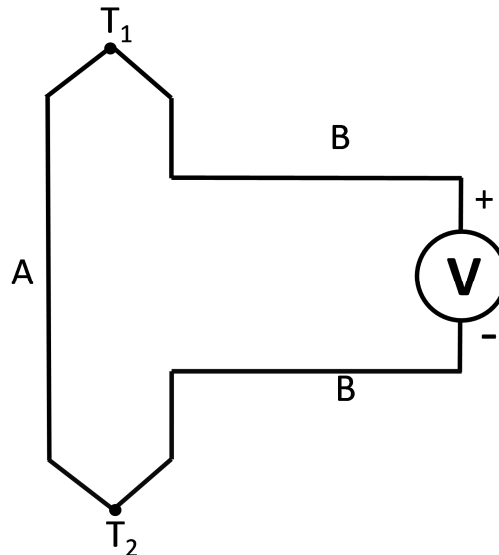


**Figure 7: Schematic diagram showing the closed loop used in Thomas Johann’s Seebeck experiment.**

Using such a system the voltage ( $V$ ) produced can be estimated by the following equation:

$$V = (S_B - S_A) \cdot (T_2 - T_1) \quad (2)$$

Where  $S_A$  and  $S_B$  are the Seebeck coefficients of material A and B and  $T_1$  and  $T_2$  are the temperatures at junctions 1 and 2 as depicted on the diagram.

The Seebeck coefficient or thermopower is a measurement of how much voltage is produced as a result of a change in temperature across a material.<sup>120</sup> This can be defined as follows:

$$S = -\frac{\Delta V}{\Delta T} \quad (3)$$

Where  $\Delta V$  is the change in voltage produced and  $\Delta T$  equals the temperature difference across the material.<sup>117</sup>

### 1.5.2. Peltier Effect

The Peltier effect is the reverse of the Seebeck effect. The phenomenon involves heating at one junction and cooling at another when an electrical current is maintained through two different conducting or semiconducting materials.<sup>121</sup>

This was discovered by the French physicist Jean-Charles-Athanase Peltier in 1834. His experimental work used a circuit made up of two materials, bismuth and copper, with two junctions between the bismuth and copper. An electrical current was maintained using a battery source and it was observed that at the junction where current flows from bismuth to copper the temperature increased, but decreased where current passed from copper to bismuth. The experimental set up is shown in **Figure 8**.<sup>122</sup>

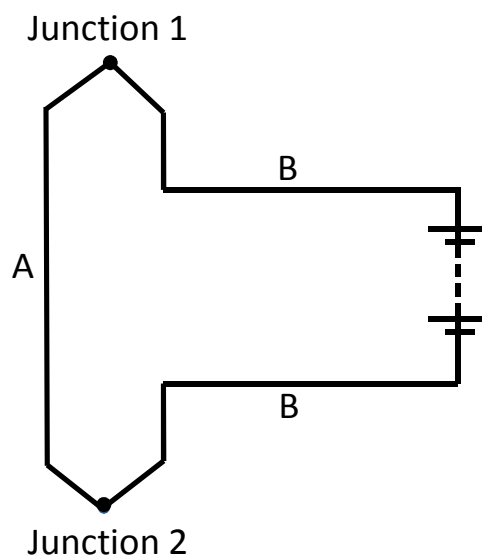


**Figure 8: Schematic diagram showing a circuit connected to a battery with 2 junctions between two different materials used by Peltier.**

The Peltier heat ( $\dot{Q}$ ) absorbed by the lower junction is given as:

$$\dot{Q} = \Pi_{AB}I = (\Pi_B - \Pi_A)I \quad (4)$$

Where  $I$  is the current,  $\Pi_A$  is the peltier coefficient of material A and  $\Pi_B$  is the peltier coefficient of material B. The Peltier coefficient is a measure of the units of heat current produced per unit of charge that passes through a material.<sup>117</sup>

### 1.5.3. Thompson effect

The Thomson effect states that any current carrying homogeneous conductor with a temperature difference between two points will either absorb or emit heat ( $q$ ).<sup>117</sup> Providing that the temperature difference is small  $q$  is given as follows:

$$q = \beta I \Delta T \quad (5)$$

Where  $\beta$  is the Thomson coefficient with units  $V K^{-1}$ ,  $I$  is the current and  $\Delta T$  is the temperature difference.<sup>117</sup>

### 1.5.4. Kelvin Relationships

All of the above effects can be related using the Kelvin relationships. The relationship between the Seebeck and Thomson coefficient is as follows:

$$\beta = T \frac{dS}{dT} \quad (6)$$

Where  $\beta$  is the Thomson coefficient,  $S$  is the Seebeck coefficient and  $T$  is the absolute temperature.

The relationship between the Peltier coefficient and the Seebeck coefficient is as follows:

$$\Pi = T.S \quad (7)$$

Where  $T$  is the absolute temperature,  $S$  is the Seebeck coefficient (calculated using relation above) and  $\Pi$  is the Peltier coefficient.<sup>117</sup>

## 1.6. Thermoelectric materials

Thermoelectric materials are materials that are able to display the effects described above. There are a variety of materials which display these effects, some are well established in the thermoelectric industry such as  $Be_2Te_3$  and silicon germanium alloys, and some less-developed, such as silicon, and polymer based thermoelectric materials. When considering thermoelectric materials there are a number of values which can indicate how well a material will perform.

Typical measurements of a materials suitability for use in thermoelectrics are the power factor and the figure of merit (ZT).

### 1.6.1. Power Factor and Figure of Merit (ZT)

The power factor is a useful indicator of ability of a thermoelectric material to produce a useful electrical output under a given temperature difference. The power factor is defined by the following equation:

$$\mathbf{Power\ Factor = \sigma S^2} \quad \mathbf{(8)}$$

Where  $S$  is the Seebeck coefficient and  $\sigma$  is the electrical conductivity. This value varies quite dramatically between classes of materials. Inorganic materials display power factors of up to  $1 \text{ Wm}^{-1}\text{K}^{-2}$  whereas organic semiconductors typically display power factors of  $1 \text{ }\mu\text{Wm}^{-1}\text{K}^{-2}$  or lower.<sup>123</sup>

One figure that is used as a demonstration of the overall thermoelectric efficiency of a material is the figure of merit (ZT) and can be calculated from the following equation:

$$\mathbf{ZT = \frac{\sigma S^2}{k} T} \quad \mathbf{(9)}$$

Where  $\sigma$  is the electrical conductivity,  $S$  is the Seebeck coefficient,  $k$  is thermal conductivity and  $T$  is temperature. It is also worth noting that the power factor is a constituent of this value. Most commercially available materials give a  $ZT > 1$  and some  $\text{Bi}_2\text{Te}_3$  alloys have been reported to display a ZT as high as 2.5.<sup>124</sup>

It is apparent from the above equation that thermoelectric performance by its nature is a compromise between the Seebeck coefficient and the electrical and thermal conductivity. As a result, this value does not always give the full picture of the materials thermoelectric performance. For example; if the ZT is high as a result of an exceptionally low thermal conductivity but the power factor is also low, then this would not necessarily be a material suitable for use in a thermoelectric device.

### 1.6.2. Thermal Conductivity and Phonon Scattering

Thermal conductivity is the ability of a material to transfer heat energy across a material. In condensed matter physics, thermal conductivity is considered to be the movement of phonons across a material. A phonon is defined as an elementary vibrational mode within a lattice of a material. The thermal conductivity can be calculated using the following equation:

$$\mathbf{k = \alpha C_p d} \quad \mathbf{(10)}$$

Where  $\alpha$  is the thermal diffusivity,  $C_p$  is the specific heat capacity of the material and  $d$  is the density. The thermal conductivity is made up of two contributions. These are the lattice and electronic thermal conductivity. These are related by the following equation:<sup>44, 125</sup>

$$k_{tot} = k_{latt} + k_e \quad (11)$$

Where  $k_e$  is the electronic thermal conductivity and  $k_{latt}$  is the lattice thermal conductivity. The  $k_e$  can be estimated from the electrical resistivity by using the Wiedermann–Franz law:<sup>104</sup>

$$k_e = LT/\rho \quad (12)$$

Where  $L$  is the Lorenz factor,  $T$  is the temperature and  $\rho$  is the electrical resistivity. The electronic contribution is generally negligible and has a small effect on the overall thermal conductivity and as a result a lot of work has been carried out focusing on the reduction of the lattice thermal conductivity.<sup>45, 126, 127</sup>

The lattice thermal conductivity can be reduced by a phenomenon known as phonon scattering which is caused by anharmonicity in the lattice of a material. This causes phonons to disperse and scatter throughout a material. Phonon scattering can be achieved by the following methods:

1. Grain boundary scattering – a phonon being scattered by the boundaries between crystals within the material.
2. Mass defects scattering – a phonon being scattered by an impurity in the system.
3. Phonon-phonon scattering – a phonon splitting or combining with another phonon.

Increasing grain boundary and mass defect scattering can easily be achieved by nanostructuring or the introduction of elements with high atomic mass as dopants, respectively.

<sup>128, 129</sup>

## 1.7. Materials

### 1.7.1. Bi<sub>2</sub>Te<sub>3</sub>

Be<sub>2</sub>Te<sub>3</sub> is a narrow gap, layered semiconductor and is currently the most effective and most widely used material in the thermoelectric industry. This is despite of its disadvantages, such as; the toxicity, and low abundance of the required raw materials. Although a lot of effort has been made in the scientific community to find an alternative to Bi<sub>2</sub>Te<sub>3</sub>, other materials have not been able to match the high ZT values reported for these materials. The highest documented ZT for Bi<sub>2</sub>Te<sub>3</sub> based materials is 2.5 at 300 K for Be<sub>2</sub>Te<sub>3</sub>/Sb<sub>2</sub>Te<sub>3</sub> alloy as reported by Rama Venkatasubramanian *et. al.*<sup>126, 130-133</sup> This value is exceptionally high and Bi<sub>2</sub>Te<sub>3</sub> based materials generally have a ZT in the range of 1 - 2 at 300 K.<sup>134</sup>

### 1.7.2. Skutlerudite

Skutlerudites are another material that shows potential for use in high temperature thermoelectric applications. The first skuttlerudites discovered were based on cobalt arsenide with iron or nickel impurities however cobalt antimonide, which shares its lattice arrangement has shown ZT in excess of 1 in both the n and p- type materials at temperatures ranging from 550 to 800 °C.<sup>135-137</sup>

The highest documented skuttlerudite ZT was reported for the n-type  $\text{Sr}_{0.07}\text{Ba}_{0.07}\text{Yb}_{0.07}\text{Co}_4\text{Sb}_{12}$  by Rogl et. al. in 2011. The ZT of this skutlerudite was 1.4 at 800 K and further work by the same laboratory in 2012 saw this increased to 1.8 using high pressure torsion to introduce lattice defects.<sup>138</sup>

Rogl and co-workers also reported a record high value for a p-type skuterudite of 1.3 at 775 K for  $\text{DD}_y(\text{Fe}_{1-x}\text{Co}_x)_4\text{Sb}_{12}$  where DD stands for didymium, a natural double filler consisting of 4.76% Pr and 95.24% Nd.<sup>136</sup>

### 1.7.3. Silicides

Metal silicide and more specifically magnesium silicide have shown real promise as a thermoelectric material, especially for mid to high temperature applications. It has been thought that magnesium silicide and tin silicide have potential for high ZT materials as they possess large effective masses, high mobilities and relatively low lattice thermal conductivities.<sup>139, 140</sup> One major advantage of metal silicide based materials is the relative abundance of their constituent elements and as a result, these materials are financially viable for mass production and device fabrication. In recent years interest in magnesium silicide based materials has spiked after Fedrov *et. al.* reported a ZT at 775 K of 1.1 in a n-type  $\text{Mg}_2\text{Si}_{0.4}\text{Sn}_{0.6}$  alloy in 2008.<sup>141</sup> This is the highest reported ZT for a metal silicide to date and other alloys have achieved a ZT close to 1 at similar temperatures, e.g. Bux *et. al.* in 2011 documented a ZT of 0.8 at 775 K using  $\text{Mg}_2\text{Si}_{0.85}\text{Bi}_{0.15}$ <sup>142</sup>

### 1.7.4. Silicon

Heavily doped electronic grade bulk silicon has a very low electrical resistivity ( $3.3 \times 10^{-4} \Omega\text{cm}^{-1}$ ) and a relatively high Seebeck coefficient ( $-86 \mu\text{VK}^{-1}$ ) giving it a high power factor. Silicon's high power factor, abundance, low toxicity and low cost makes it an attractive material for use in the thermoelectrics industry. However despite silicon's many advantages it also displays a high lattice thermal conductivity ( $87.3 \text{ Wm}^{-1}\text{K}^{-1}$ ) and as a result bulk silicon has a ZT of approximately 0.01.<sup>104</sup> Despite this, a lot of work has been carried out to try and reduce the thermal conductivity enough so that its potential can be realised.

Silicon nanostructures show much lower thermal conductivities as a result of a more efficient boundary scattering of phonons, which can lead to a marked improvement to the figure of merit.<sup>143</sup> For silicon nanowires, alteration of surface roughness, diameter and doping concentrations of nanowires has resulted in a  $ZT \approx 1$ .<sup>144, 145</sup> Although it is worth noting, this was obtained from a single narrow nanowire, it is not yet demonstrated if the value can be translated into bulk materials. These studies suggest that silicon nanowire arrays could be a potential silicon based thermoelectric material<sup>146</sup> but preparation methods typically use harsh conditions or toxic and expensive reagents, such as trisilane,<sup>147, 148</sup> hydrogen fluoride and silver nitrate.<sup>149</sup>

Another potential silicon based thermoelectric material is nanostructured bulk silicon. The key purpose of this is to increase the phonon scattering effect by increasing the number of grain boundaries and hence lowering the thermal conductivity, ideally without greatly affecting the high power factor associated with the bulk.<sup>132, 145, 150, 151</sup> Theoretical studies suggest the potential for these nanostructured bulk materials to reach a  $ZT$  of 0.3 at ambient conditions and as high as 1 at high temperatures.<sup>132, 152</sup> However this potential has not yet been realised in such materials without the introduction of significant quantities of germanium.<sup>152, 153</sup> There are a number of advantages to such an approach, including low cost of raw materials, relative ease of production and scalability.<sup>154</sup>

In 2010 Tang *et. al.* discussed the potential of porous or holey silicon ribbons (**Figure 9**) as a thermoelectric material.<sup>155</sup> The holey silicon ribbons were prepared by the deep reactive ion etching of silicon-on-insulator substrates masked by a thin chromium layer, templated by self-assembled block copolymer film. This material displayed a  $ZT$  of 0.4 at ambient temperature which is 400 times higher than that of bulk silicon and 4 times higher than has been observed in nanostructure bulk silicon.<sup>152</sup> Although as with silicon nanowires this has only been achieved on a single ribbon and proof of feasibility is yet to be documented.

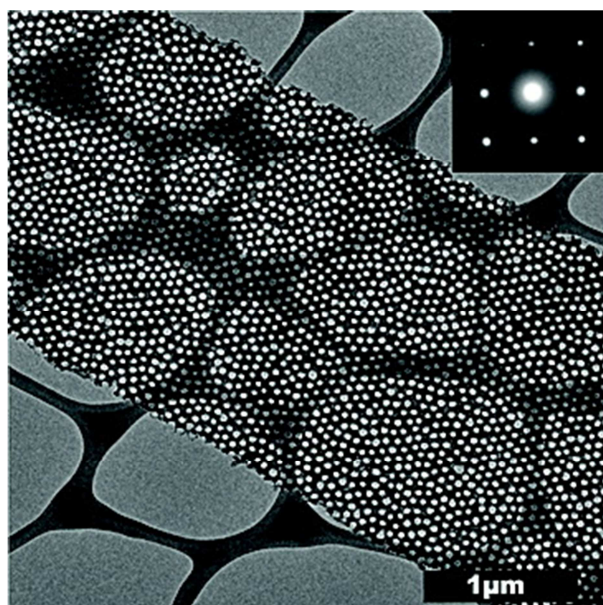


**Figure 9: Bright-field TEM image of a section of holey silicon ribbon. The porosity is estimated as ~35% through the entire ribbon. Selected area electron diffraction pattern (inset) indicates its single crystalline nature.<sup>155</sup>**

### 1.7.5. Polymers

The typical thermal conductivity values for organic semiconductors are generally four to five orders of magnitude lower than that of nanostructured  $\text{Bi}_2\text{Te}_3$  alloys. However unlike inorganic semiconductors like silicon or bismuth telluride, conductive polymers are limited by their low power factors.<sup>156</sup> Polyacetylene is a good example of an organic semiconductor with a high power factor. Work published by Nogami et. al. in 1990 shows that a power factor of  $10^{-4} \text{ Wm}^{-1}\text{k}^{-2}$  can be achieved for a polyacetylene with optimised iodine doping.<sup>157</sup> This is mainly attributed to its high electrical conductivity of  $10^5 \text{ Scm}^{-1}$  but this highly doped conductive form is not very stable.<sup>156, 157</sup> As a result, a lot of time has been invested into other organic semiconductors based on polythiophene or polyanilines.

Polyanilines are attractive polymers for use as thermoelectric materials due to their high environmental stability and the ease in which they can be processed. However to date the highest ZT obtained from a polyaniline based material is 0.01 at 445 K for a multi-layered film of undoped emeraldine and 10-camphorsulfonic acid doped emeraldine salt.<sup>156, 158, 159</sup> This work reported by Toshima *et. al.* demonstrated a power factor six times than that of bulk film 10-camphorsulfonic acid doped of polyaniline.<sup>159, 160</sup>

Another class of polymers that are attractive for use in thermoelectrics are polythiophenes.<sup>161</sup> Two interesting variants of polythiophene applied to thermoelectrics are poly(3-hexylthiophene)(P3HT)<sup>162</sup> and poly(3,4-ethylenedioxythiophene) (PEDOT).<sup>163</sup> In 2010 Xuan *et. al.*



studied the optimisation of the power factor by doping such polymers and although respectable electrical conductivity was achieved the optimum power factor was only  $1.4 \times 10^{-7} \text{ W m}^{-1} \text{ K}^{-2}$ , as a result of a very low Seebeck coefficient. In 2011 Bubnova *et. al.* reported a similar study for PEDOT-toslate with a conductivity of  $300 \text{ S cm}^{-1}$ , they were able to optimize the power factor by gradually reducing the oxidised (p-doped) polymer with tetrakis(dimethylamino)ethylene. The conductivity reduces from  $300 \text{ S cm}^{-1}$  at 36% oxidation to  $10^{-4} \text{ S cm}^{-1}$  at 15% oxidation. The Seebeck coefficient increases by a factor of 20 upon exposing the reduction of the polymer, from  $40 \mu\text{V K}^{-1}$  at 36 % oxidation to a maximum of  $780 \mu\text{V K}^{-1}$  at the low levels of oxidation. As a result of this study the optimum power factor reported is  $324 \mu\text{W m}^{-1} \text{ K}^2$  at 22 % oxidation. With the powerfactor optimised a *ZT* of 0.25 at ambient temperature is obtained making it comparable to other inorganic materials.<sup>163</sup>

### 1.7.6. Organic-Inorganic Nanocomposites

For many years inorganic nanocomposites and alloys have been investigated as a way to improve the efficiency of solid state thermoelectric materials. Recently, organic-inorganic nanocomposites have also been considered. This approach is based on the concept of combining the processability of organic semiconductors with the thermoelectric performance of the inorganics. An organic or polymer can be used to reduce electrical resistance between inorganic nanostructures in addition to maintaining a low thermal conductivity.<sup>123</sup> This is an interesting alternative to nanostructured bulk materials as they do not require the same high temperature processing.<sup>123</sup> As a result these materials are compatible with other low temperature fabrication techniques such as printing.<sup>164</sup>

In 2014 Wang *et. al.* reported a theoretical study to understand the potential of polymer-inorganic nanocomposites to obtain suitably high power factors. In this model they use a semiconductor quantum dot and trapped it between two leads of aligned conductive polymer. The conclusions of the work suggest the potential of using semiconductor quantum dot – polymer. This work also adds some theoretical guidance to the effect of both nanoparticle choice and polymer choice for the design of better inorganic – organic nanocomposite thermoelectric materials<sup>165</sup>

To date there are many examples of polymer-inorganic nanocomposites and their thermoelectric properties. The best of these was reported by See *et. al.* in 2010 using a composite of PEDOT:polystyrenesulfanoate (PSS) and tellurium nanowires. This material is documented to have achieved a *ZT* of 0.1 at ambient temperature.<sup>166</sup>

Another interesting insight into this type of material is highlighted by Zhang *et. al.* In this work a composite of 10% P-type PEDOT:PSS and 90 % n-type  $\text{Bi}_2\text{Te}_3$  nanoparticles was produced.<sup>167</sup> One

surprising insight in this work is that the p-type PEDOT:PSS did not affect the negative Seebeck coefficient of the bismuth telluride particles opening up an attractive method for the development of n-type organic inorganic nanocomposite materials. Although in this study the ZT was not calculated a conservative estimate suggests a ZT of approximately 0.08 at ambient temperature.

123

## 1.8. Thesis Overview

Chapter 2 describes the synthetic procedures for the production of different functionalised SiNPs and describes the techniques used to analyse and characterise the resulting materials. In addition, methods used for the measurement of thermoelectric properties are discussed.

Chapter 3 describes a one-pot synthetic procedure for the synthesis of alkyl functionalised SiNPs using micelle reduction. The material was characterised using a variety of techniques including FTIR, <sup>1</sup>H-NMR, XPS and TEM. To follow this, the photophysics were investigated using UV/Vis and PL as well as chemical stability studies using FTIR and XPS. This chapter is based on work from (Ashby S, Thomas J, Coxon P, et al. The effect of alkyl chain length on the level of capping of SiNPs produced by a one-pot synthesis route based on the chemical reduction of micelle. *Journal of Nanoparticle Research* 2013;15(2): 1-9.) and (Coxon PR, Ashby SP, Frogley MD, Chao Y. Thermal evaporation and x-ray photostability of dodecyl-passivated silicon nanoparticles. *Journal of Physics D: Applied Physics* 2012;45: 355303.)


Chapter 4 discusses the synthesis of phenylacetylene functionalised SiNPs using a solution reduction to produce Cl functionalised SiNPs followed by alkylation using lithium phenylacetylide. The material was characterised using FTIR, <sup>1</sup>H-NMR and <sup>13</sup>C-NMR, TEM, EDS, and XPS. The thermoelectric properties were tested on a consolidated pellet. This chapter is based on work from (Ashby S, Thomas JA, Garcia-Canadas J, et al. FD 176: Bridging Silicon Nanoparticles and Thermoelectrics: Phenylacetylene Functionalization. *Faraday Discussions* 2014) and (Ashby S, García-Cañadas J, Min G, Chao Y. Measurement of Thermoelectric Properties of Phenylacetylene-functionalised Silicon Nanoparticles and Their Potential in Fabrication of Thermoelectric Materials. *Journal of Electronic Materials* 2012: 1-4.)

Chapter 5 discusses the synthesis of terthiophene functionalised SiNPs using a solution reduction to produce Cl functionalised SiNPs followed by alkylation using lithium phenylacetylide. The material was characterised using FTIR, TEM, EDS, and XPS. The thermoelectric properties and thermostability were tested on a consolidated pellet.

Chapter 6 discusses the synthesis of phenylacetylene functionalised SiNPs from electrochemically etched porous SiNPs using a halogenation/alkylation two step functionalisation.

The material was characterised using FTIR,  $^1\text{H-NMR}$ ,  $^{13}\text{C-NMR}$  and  $^{31}\text{P-NMR}$ , TEM, EDS, and XPS. The thermal stability of this material was tested using TGA and DSC. This chapter is based on work from (Ashby S, Chao Y. Use of Electrochemical Etching to Produce Doped Phenylacetylene Functionalized Particles and Their Thermal Stability. *Journal of Electronic Materials* 2014;43: 2006-10.)<sup>168</sup>





# Chapter 2:

## Methods and Materials

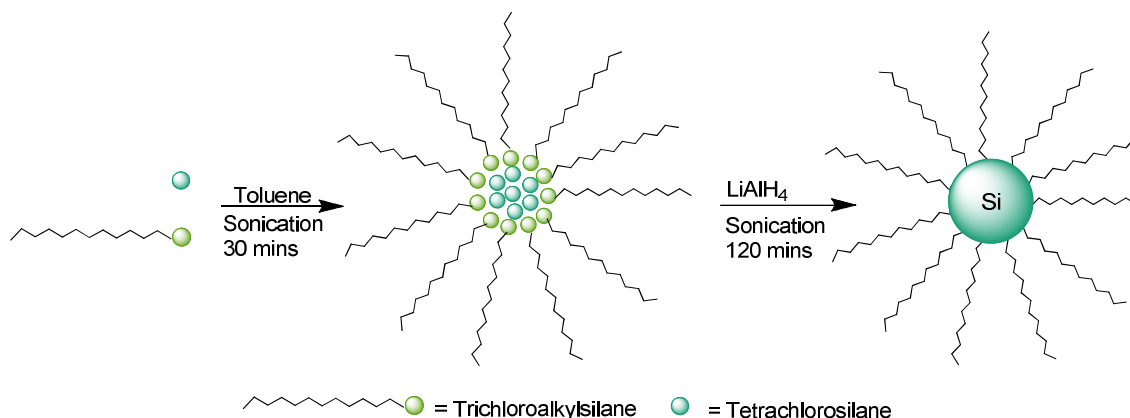
## 2.1. Materials

The following materials reagents and solvents have been used in the following work: Toluene (Fisher Scientific, 99.9 %, dried by reflux over molten sodium and collected by distillation), tetrahydrofuran (Fisher Scientific, 99.5 %, dried by reflux over sodium and benzophenone and collected by distillation), diethyl ether (Sigma Aldrich, 99.5 %, dried by reflux over sodium and benzophenone and collected by distillation), chlorobenzene (Sigma-Aldrich, 99 %, dried by refluxing over calcium hydride and collected by distillation), ethanol (Sigma-Aldrich, 99.8 %), methanol (Fisher Scientific, 99.7 %), dichloromethane (Sigma-Aldrich, 99 %) and hexane (Fisher Scientific, 99.9 %). lithium aluminium hydride solution (Fisher Scientific, 1 M in tetrahydrofuran), silicon tetrachloride (Sigma-Aldrich, 99 %), trichloro(hexyl)silane (Sigma-Aldrich, 97 %), trichloro(dodecyl)silane (Sigma-Aldrich, 95 %), trichloro(octyl)silane (Sigma-Aldrich, 97 %), trichloro(octadecyl)silane (Sigma-Aldrich, 90 %), lithium phenylacetylide (Sigma-Aldrich, 1 M solution in tetrahydrofuran), sodium metal (Acros Organics, 99.8 %), naphthalene (Acros Organics, 99 %), hydrofluoric acid (Acros Organics, 48 % in water), silicon wafer (Compart Technology Ltd., orientation: 111, Resistivity: 10-100  $\Omega$ cm, Type/dopant: n/boron, thickness: 500  $\mu$ m, one side polished), phosphorous pentachloride (Sigma-Aldrich, 99 %), benzoyl peroxide (Luperox A75) (Sigma-Aldrich, 75 %), magnesium turnings (Sigma-Aldrich, 95 %), 2,5-dibromothiophene (Acros Organics, 95 %), 2-bromothiophene (Sigma-Aldrich, 98 %), dichloro(diphenylphosphinopropyl) nickel (Sigma-Aldrich), nitrosyl tetrafluoroborate (Sigma-Aldrich, 95 %) and chloroform-d (Acros Organics, 99.8 atom % D)

## 2.2. Synthetic Procedures

### 2.2.1. One-Pot Synthesis of Alkyl Functionalised SiNPs

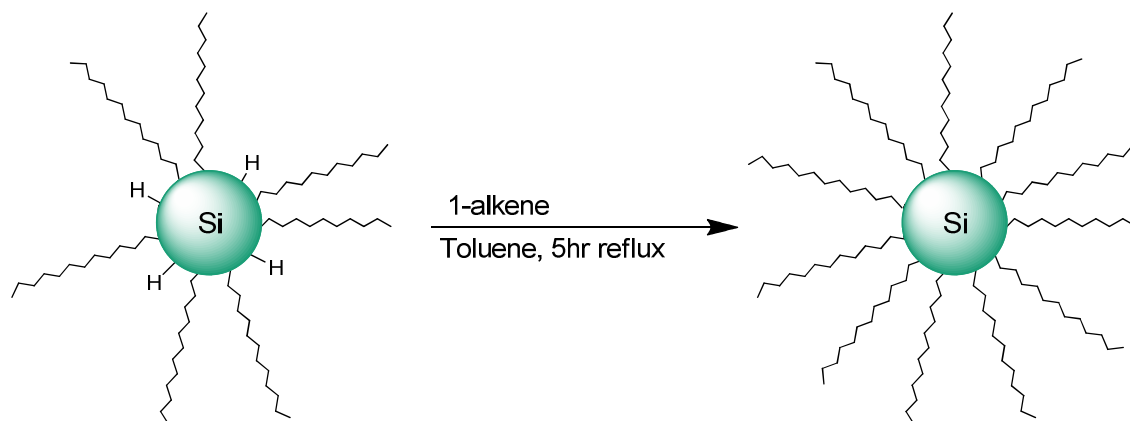
Based on a preparation by Wang *et. al.*<sup>91</sup> dry toluene (50 ml) was degassed by ten repetitions of 1 minute of sonication under vacuum followed by filling the flask with N<sub>2</sub> gas after each repetition. To this an alkyl-SiCl<sub>3</sub> based surfactant (0.7 mmol) and SiCl<sub>4</sub> (0.1 mL, 0.7 mmol) were introduced and dispersed by vigorous shaking for 1 min followed by sonication for 30 mins. This was then reduced using a 1M LiAlH<sub>4</sub> solution in THF (4 mL, 4 mmol) which was added dropwise over 5 minutes followed by ultra-sonication for 120 minutes. Methanol or ethanol (40 mL) was carefully introduced to the reaction mixture, followed by ultra-sonication for 60 minutes to quench the unreacted reducing agent. See reaction **Scheme 12**:



**Scheme 12: One pot micelle reduction synthesis of alkyl functionalised SiNPs.**

All solvent was removed to give a white powder, which contained a mixture of by-product and SiNPs. This was sonicated in hexane (25 ml) for 10 mins, filtered using a polyvinylidene (PVDF) syringe filter (450 nm) and dried *in vacuo* to give a clear pale yellow oil ( $\approx 120$  mg) as the product.

For some samples a further functionalisation step was required using thermal hydrosilylation (**Scheme 13**). The SiNPs produced above were ultrasonicated for 5 minutes in a 0.04 M solution of the corresponding 1-alkene in toluene (10 ml, 0.4 mmol). This mixture was heated at reflux for 5 hours and dried *in vacuo* to give alkyl functionalised SiNPs as clear pale yellow oil.<sup>169</sup>

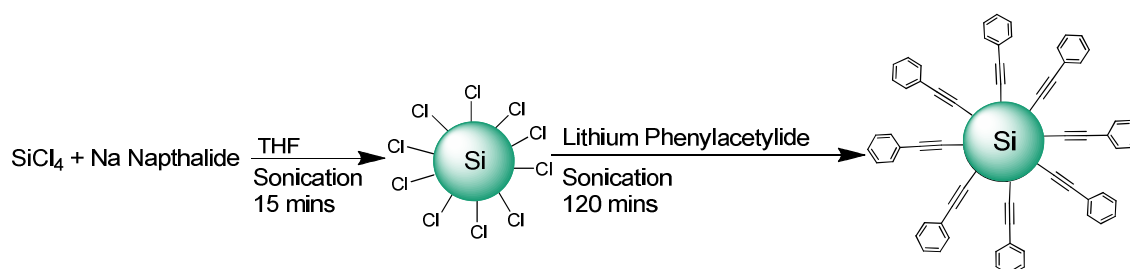


**Scheme 13: Hydrosilylation of unreacted Si-H species on the surface of alkyl functionalised SiNPs.**

### 2.2.2. Bottom Up Synthesis of Phenylacetylene Functionalised SiNPs

Based on a preparation by Baldwin *et. al.*<sup>87</sup> a solution of sodium naphthalide (70 ml) was prepared by sonication of sodium metal (1 g, 43 mmol) and naphthalene (4.3 g, 34 mmol) in dry THF (70 ml) under a nitrogen atmosphere for 2 hr to give a dark green suspension. In a round bottom flask flushed with nitrogen  $\text{SiCl}_4$  (1 ml, 7 mmol) was dispersed in dry THF (200 mL) using an ultrasonic bath for 15 mins. The freshly prepared sodium naphthalide solution was added quickly

through a cannula and the flask placed in an ultrasonic bath for 15 mins, giving a dark brown suspension. To this a solution of lithium phenylacetylide (5 ml, 1 M in THF, 5 mmol) was added slowly over 5 mins and placed in an ultrasonic bath for a further 2 hr, giving an orange/red cloudy suspension. See reaction **Scheme 14**:



**Scheme 14: Synthesis of phenylacetylene functionalised SiNPs using a bottom up approach.**

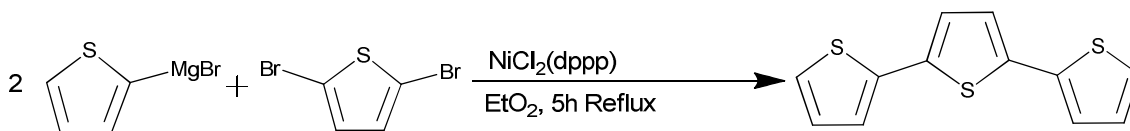
The reaction mixture was quenched with acidified water (50 ml) and extracted with diethylether (100 ml). The organic layer was washed with water (50ml) and brine (50ml). All solvent was removed *in vacuo* and heated to 100 °C under reduced pressure with an inline trap to remove the residual naphthalene, giving phenylacetylene functionalised SiNPs as an orange waxy solid.

### 2.2.3. Bottom Up Synthesis of Terthiophene Functionalised SiNPs

#### 2.2.3.1. Terthiophene

Using a previously published method developed by Smeets *et. al.*<sup>170</sup> magnesium turnings (3 g, 0.12 mol) and a stirrer bar were added to a flask and flushed with nitrogen. Dry diethyl ether (50 ml) was added and the mixture was cooled down to 0 °C in an ice bath. 2-bromothiophene (6.3 ml, 65 mmol) was added slowly and the flask was allowed to warm to ambient temperature for 1 hr. This was used without further purification. The 2-bromomagnesiumthiophene was added over 5 mins to a mixture of 2,5-dibromothiophene (3.6 ml, 32 mmol) and dichloro(diphenylphosphinopropyl) nickel] (60 mg, 0.1 mmol) in dry diethyl ether (20 ml). This was heated at reflux for 5 hr to give a dark orange/red solution. Aqueous HCl (40 ml, 0.1 M) was added to quench the reaction and the mixture was extracted with toluene (50 ml). The organic layer washed with water (40 ml) and brine (40 ml). The organic layer was collected and the volume of toluene was reduced using a rotary evaporator. The product was precipitated by the addition of cold methanol to give an orange solid. This was filtered out to give terthiophene as a green/orange crystalline solid with a 60 % yield. m.p. 94-95 °C;  $^1\text{H}$  NMR ( $\text{CDCl}_3$ , 500 MHz): 7.20 (dd, 2H,  $J= 5.1, 1.2$  Hz), 7.11 (dd, 2H,  $J=3.7, 1.2$  Hz), 7.06 (s, 2H), 7.01 (dd, 2H,  $J= 5.1, 3.7$  Hz).  $^{13}\text{C}$  NMR ( $\text{CDCl}_3$ , 500 MHz): 137.07, 136.14, 127.84, 124.26, 77.00.

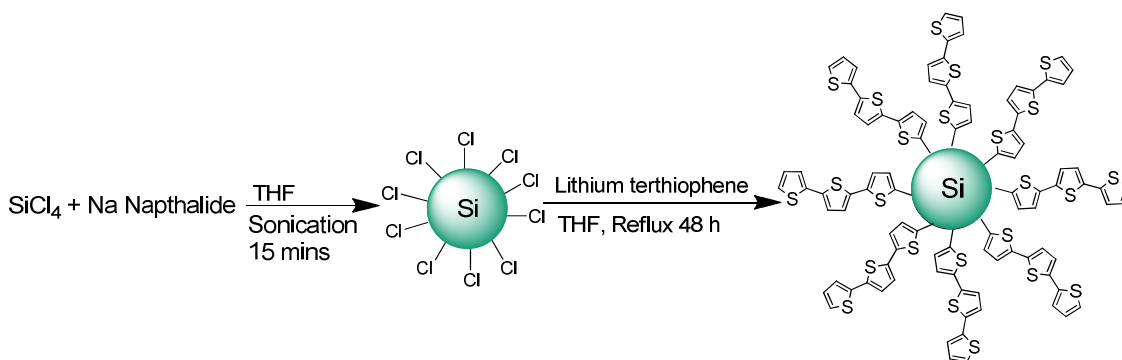




**Scheme 15: Synthesis of terthiophene.**

### 2.2.3.2. Terthiophene Functionalised SiNPs.

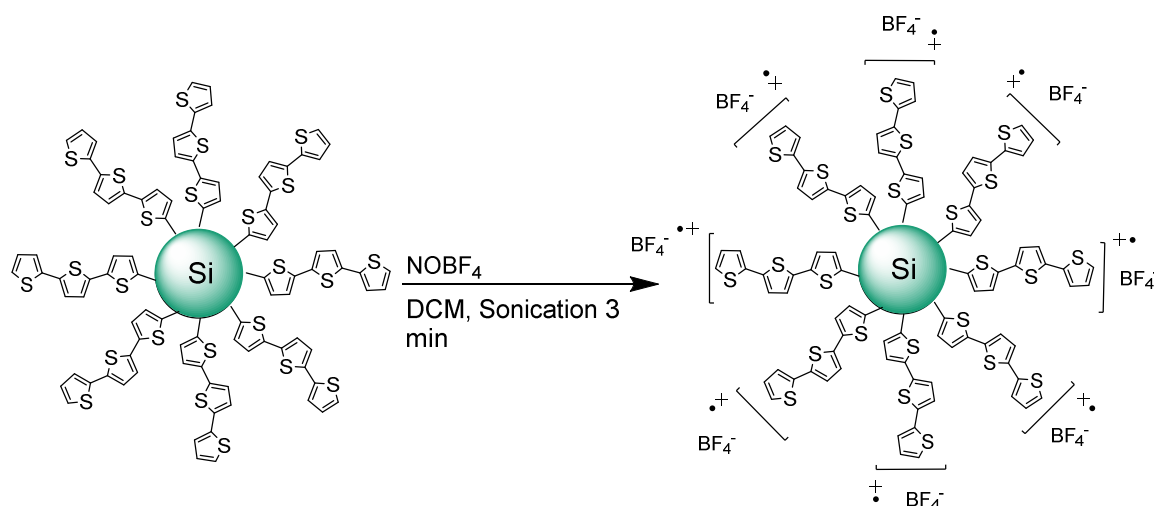
Using the procedure previously described in the synthesis of phenylacetylene functionalised SiNPs, a solution of sodium naphthalide (70 ml) was prepared by sonication of sodium metal (1 g, 43 mmol) and naphthalene (4.3 g, 34 mmol) in dry THF (70 ml) under a nitrogen atmosphere for 2 hr. In a round bottom flask flushed with nitrogen,  $\text{SiCl}_4$  (1 ml, 7 mmol) was dispersed in dry THF (200 mL) using an ultrasonic bath for 15 mins. The freshly prepared sodium naphthalide solution was added quickly through a cannula and the flask placed in an ultrasonic bath for 15 mins, giving a dark brown suspension. Meanwhile terthiophene (0.65 g, 2.6 mmol) was dissolved in dry THF (20 ml) in a flask flushed with nitrogen. This was cooled to 0 °C using an ice bath and *n*-butyllithium solution (2 ml, 1.6 M in hexane, 3.2 mmol) was added dropwise and stirred for 1 hr to give a yellow suspension. This was added slowly over 5 mins to the suspension of chlorine terminated SiNPs and heated at reflux for 48 hr as described by He *et. al.*<sup>171</sup>: see reaction **Scheme 16**:



**Scheme 16: Synthesis of terthiophene functionalised SiNPs s using a bottom up approach.**

The functionalised SiNPs were then washed with acidified water and brine and extracted with diethyl ether. All solvent was removed *in vacuo* and the residue heated to 100 °C under reduced pressure to remove the residual naphthalene, giving terthiophene functionalised SiNPs as a yellow/green crystalline solid.

To oxidise/dope the ligands, terthiophene functionalised SiNPs were dissolved in dichloromethane. To this  $\text{NOBF}_4$  was added. This process was repeated for ratios varying from 0.1 by up to 2 by weight. This was sonicated for 3mins to give a dark green/blue suspension (**Scheme 17**).



**Scheme 17: Oxidation/doping of terthiophene functionalised SiNPs using a bottom up approach.**

The resulting doped and undoped materials were pressed into pellets. Approximately 200 mg of the material was measured in to a hardened steel dye with a diameter of 13 mm and max. pressure of 740 MPa. This was pressed using a hydraulic press at a pressure of 740 MPa for 3 mins to give a solid pellet of thickness 2 mm. This pellet was used for all electrical and thermal measurements.

#### 2.2.4. Top Down approach to Phenylacetylene Functionalised SiNPs

For the initial synthesis of SiNPs by electrochemical etching, a previously documented method was used<sup>73</sup>. Four chips (11 × 11 mm) of boron doped silicon of resistivity 10 Ωcm were electrochemically etched using a 1:1 solution of aqueous hydrofluoric acid and ethanol in a PTFE etching cell designed in house (**Figure 10**).

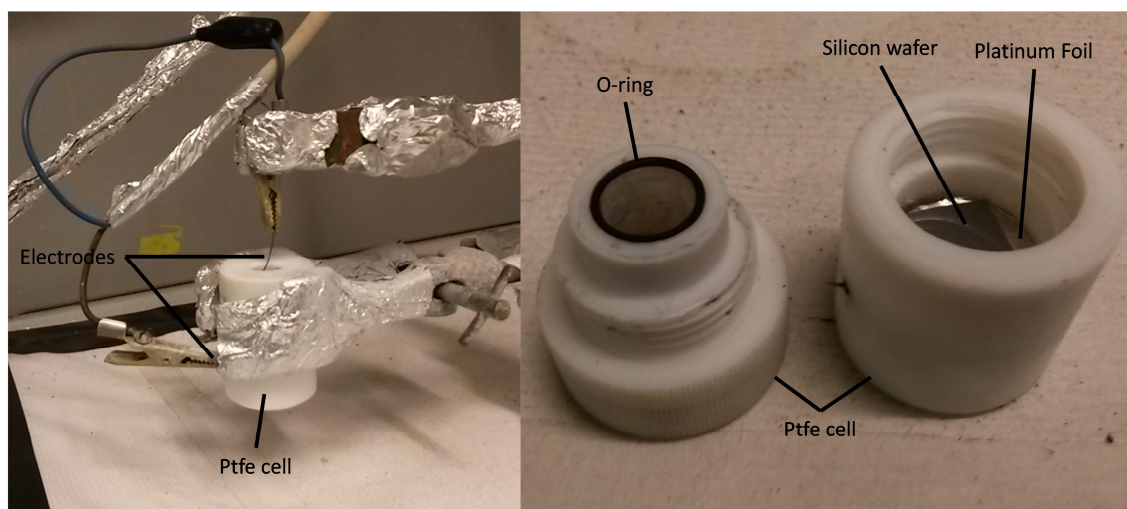
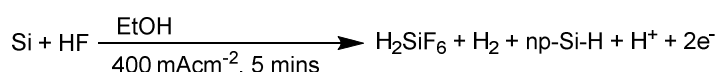


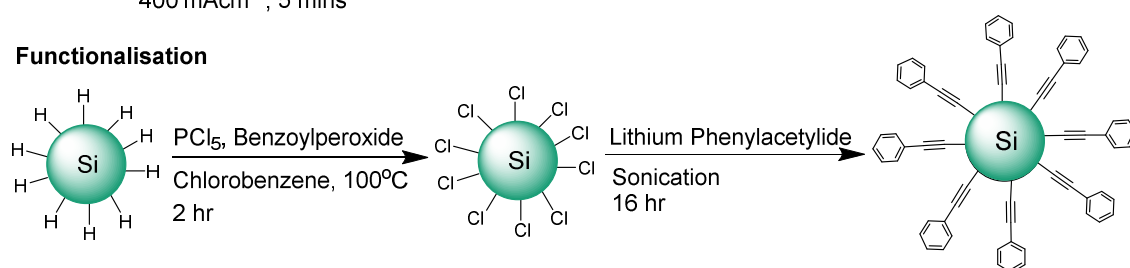
**Figure 10: Annotated photograph of electrochemical etching set up.**

These chips were etched at a current density  $400 \text{ mAcm}^{-2}$ , for 5 min. After etching the chips were dried *in vacuo* to remove residual hydrofluoric acid, and were stored under nitrogen gas until use. Once dried, benzoyl peroxide (0.4 g, 1.6 mmol) and phosphorus pentachloride (1.2 g, 5.8 mmol) were added, followed by dry, degassed chlorobenzene (10 ml). The mixture was sonicated for 10 mins and then heated to  $90^\circ\text{C}$  for 2 h. The solvent was removed *in vacuo* and the product was re-dispersed in dry tetrahydrofuran. To this, lithium phenylacetylide solution (1 ml, 1 M in tetrahydrofuran, 1 mmol) was added. This was heated at  $50^\circ\text{C}$  for 16 h. See reaction **Scheme 18**:

#### Particle Synthesis by Electrochemical Etching



#### Functionalisation



**Scheme 18: Functionalisation of hydrogen functionalised SiNPs using a chlorination- alkylation approach.**

The dark suspension was quenched with dilute hydrochloric acid (10 ml) and extracted with dichloromethane (20ml). The organic layer was washed with water and brine (10ml). The solvent was removed *in vacuo* to give a dark orange solid.

## 2.3. Characterisation Techniques

### 2.3.1. Chemical Analysis

#### 2.3.1.1. Fourier Transform Infrared Spectroscopy

Fourier transform infrared spectroscopy (FTIR) is a particularly useful tool for the identification of a specific functionalisation on the surface of SiNPs s for example; the presence of the ligand, Si-O or even Si-H.

FTIR spectra were recorded using a Perkin-Elmer Spectrum 100 ATR FTIR spectrometer. The initial background was taken on a blank crystal between the range of  $4000$  and  $600 \text{ cm}^{-1}$ , 8 scans. The sample was placed on the crystal and a spectrum was taken between  $4000$  and  $600 \text{ cm}^{-1}$ , 8 scans.

### 2.3.1.2. Nuclear Magnetic Resonance Spectroscopy

Nuclear magnetic resonance spectroscopy (NMR) is an important characterisation technique in the identification of molecular species. However with regards to functionalised SiNPs it can be less useful; especially in solution NMR. In many cases, especially with larger particles (approx. 10 nm) the signals for molecular species on the surface are often broadened and can be invisible to the technique, even when the particles are well dispersed.<sup>172, 173</sup>

$^1\text{H}$ ,  $^{13}\text{C}$  and  $^{31}\text{P}$ -NMR was run on samples dissolved in  $\text{CDCl}_3$  using a Bruker 500MHz NMR spectrometer. These samples were measured relative to chloroform from the lock solvent ( $\text{CDCl}_3$ ).

### 2.3.1.3. Energy Dispersive X-ray Spectroscopy

Energy dispersive X-ray spectroscopy (EDX) useful for analysing the elemental components of a material. This technique uses a high energy electron beam to eject electrons from inner energy levels, which are bound to the nucleus of an atom. EDX detects the energy of the photon emitted as electrons from the outer energy levels fall in to the vacant inner levels. The energy of the X-rays emitted is characteristic of the energy difference between the two levels, and of the atomic structure of the element. As a result the elemental composition can be obtained.<sup>174</sup> However this technique is not particularly sensitive to atomic ratios and the data obtained from this technique is generally indicative.

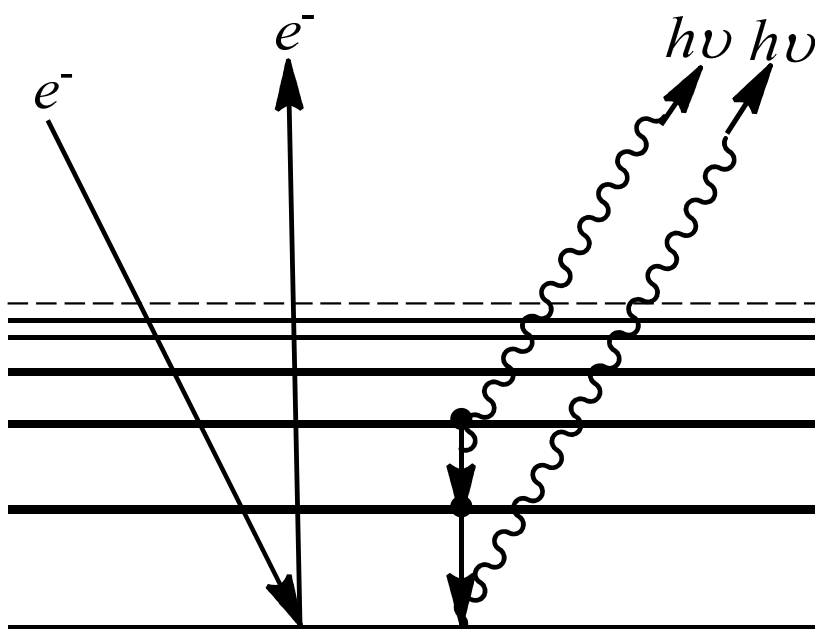


Figure 11: Schematic diagram of processes occurring during EDX.

EDX analysis was performed using a JEOL SEM machine with an attach EDX sensor. Using the SEM, points of interest on the material were identified and an individual spectrum was run for each spot of interest. Gold was used as a reference material for EDX but also to allow conduction away from the surface of the material when observed under the SEM.

#### 2.3.1.4. X-ray Photoelectron Spectroscopy

X-ray photoelectron spectroscopy (XPS) is a useful technique in the analysis of the elemental composition of the surface of materials. This technique compared to EDX is also quantitative and subtle differences in the binding energies gives insight into the bonding environment and surrounding elements. This technique uses a source of x-ray radiation to irradiate the sample with X-rays. All electrons whose binding energy is less than that of the incident x-rays are ejected from the atom. The detector measures the kinetic energy of these electrons. The energy of these electrons is characteristic of specific energy levels, elements and environments. The kinetic energy can then be converted to the binding energy using the following relationship:

$$E_k = h\nu - E_b - \Phi \quad (13)$$

Where  $E_k$  is the kinetic energy,  $h\nu$  is the photon energy,  $\Phi$  is the characteristic work function of the material and  $E_b$  is the binding energy of the electron to the atom.<sup>174</sup>

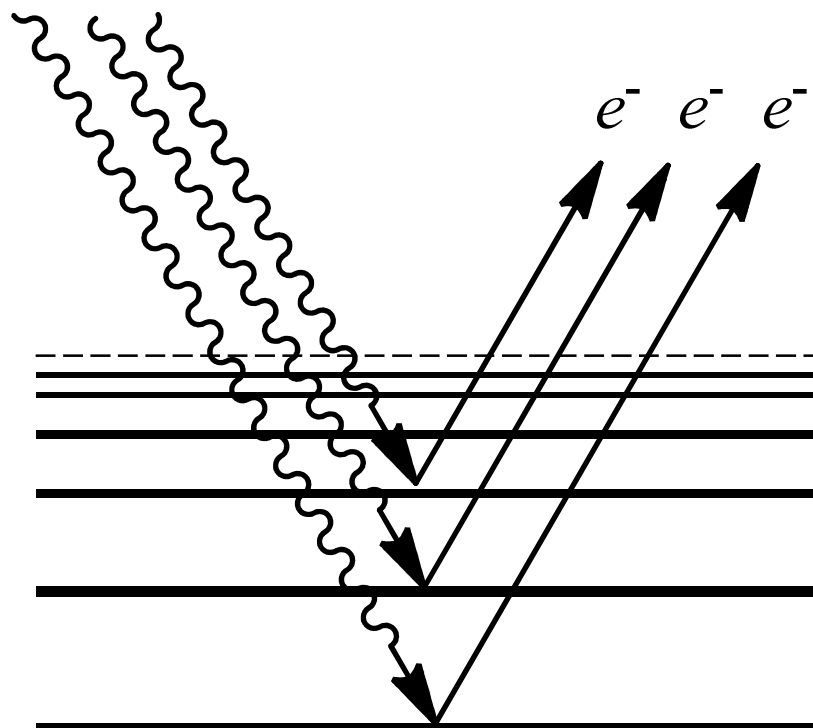


Figure 12: Schematic diagram of processes occurring during XPS.

X-ray photoelectron spectroscopy (XPS) from Beamline D1011, Maxlab, Lund, Sweden was run using a Scienta SES200 electron energy analyser with an energy resolution,  $E/dE$  of  $1.5 \times 10^3 - 1.3 \times 10^4$  running SES analyser control software. A synchrotron light source was used. For core level and valence band XPS spectra acquisition, the analyser pass energy was set at 150 meV with energy steps of 0.05 eV and a dwell time of 1 s. All measurements were carried out at room temperature in normal emission geometry. Measurements were made on both evaporated films and drop cast films on a clean gold foil. To evaporate the SiNPs, the temperature of the crucible was increased to 240 °C. Once reached a target of freshly sputtered Au foil was placed in direct line of the flow of material. XPS data analysis and high resolution peak fitting was performed with CasaXPS software (version 2.3.15).

XPS analysis by NEXUS nanolab was carried out on a K-Alpha XPS instrument (Thermo Scientific, East Grinstead, UK). A monochromatic Al K $\alpha$  x-ray source (1486.6 eV) was used with a spot size of 400  $\mu\text{m}$  diameter. A pass energy of 200 eV and step size of 0.4 eV was used for survey spectra, and a pass energy of 40 eV and step size of 0.1 eV was used for high resolution spectra. Samples were prepared by drop-casting a concentrated dispersion of the sample to produce a thick film on to gold foil (10mm x 10mm). XPS data analysis and peak fitting was performed with CasaXPS software (version 2.3.15).

### **2.3.1.5. X-ray Absorption Spectroscopy**

X-ray absorption spectroscopy (XAS) or X-ray absorption near edge structure (XANES) can be a useful tool for the identification specific elements and the quantity of said element present within a sample. Each individual element has a characteristic set of K, L and M and other absorption edges. As a result the wavelength at which these edges occur can be used to identify the elements present in a sample. It is also possible to use the magnitude of the change to identify the amount of an element present within the sample.<sup>174</sup>

X-ray absorption spectroscopy (XAS) spectra were collected across the silicon *L* edge and the carbon *K* edge in total electron yield (TEY) mode. A synchrotron light source was used. The TEY was recorded by the drain current method measured via a diode coupled directly to the sample holder. Spectra have been normalized to the live current of the beamline D1011 MAXlab, Lund, as measured by a gold grid monitor placed before the sample. The sample was measured on a drop cast film on a clean gold foil substrate (10 mm x 10 mm).

## 2.3.2. Microscopy

### 2.3.2.1. Transmission Electron Microscopy and Super Scanning Tunnelling Electron Microscopy

Particle and crystal size plays a key part in the properties observed in SiNPs and the resulting materials produced. As a result, it is important to be able to measure the particle size and the distribution. Transition electron microscopy (TEM) is the best way to identify this for unsolvated particles. High resolution TEM and super scanning tunnelling electron microscopy (SuperSTEM) are useful tools when identifying if the particles are crystalline, especially when organic impurities are present which are able to affect the result obtained from x-ray powder diffraction.

Low resolution TEM micrographs were taken using a JEOL JEM2000 electron microscope. TEM samples were prepared by drop casting a dilute suspension of the sample dispersed in chloroform onto a 200 mesh copper grid with a holey carbon film. The solvent was evaporated in air for 5 mins before it was attached to the sample holder and inserted into the microscope chamber. TEM micrographs were taken at different spots of the grid. These micrographs were processed and analysed using Image J software. Average diameter of these particles was given by measuring 300 particles manually from different spots on the grid and calculating a mean and standard deviation of the sample.

High resolution TEM studies were performed with a JEOL (JEM- 2000 Ex) microscope and high-resolution TEM was performed with a Philips CM200 FEGTEM microscope. TEM samples were prepared by dipping a carbon-coated 300 mesh copper grid into a filtered solution of SiNPs in water. The solvent was evaporated and TEM micrographs were typically taken at different spots of each grid

Super scanning tunnelling electron microscopy (SuperSTEM) facility at Darsbury was used to obtain atomic number contrast (Z-contrast) STEM images. This was performed on a Nion UltraSTEM 100, operated at 100 kV using a cold field emission electron source, and a corrector capable of neutralizing aberrations up to fifth order. Samples were prepared by drop casting SiNPs solution onto a graphene substrate. The solvent was evaporated and micrographs were taken at different regions of each grid. Samples were baked at 135 °C for approximately 7 h in a turbo backed vacuum oven before SuperSTEM imaging to reduce contamination. The micrographs obtained were analysed and processed using Digital Micrograph software (version 3.5.2).

## 2.3.3. Optical Properties

### 2.3.3.1. Ultraviolet - Visible Spectroscopy

UV/Vis spectroscopy is used to show the maximum absorbance of the materials produced. In SiQDs this is typically seen as a shoulder on the spectrum as the SiNPs scatter shorter

wavelengths. As a result as the spectrum moves towards 200nm the absorbance increases as more scattering occurs.

The UV/Vis absorption spectrum was taken for samples dissolved in a suitable solvent; in a quartz cell (10 mm × 10 mm) were taken using a Perkin-Elmer 35 UV-Vis double-beam spectrophotometer. Scan range was 200-700nm at a rate of 900 nmmin<sup>-1</sup>. The background was corrected by subtracting the spectrum for the blank solvent.

### **2.3.3.2. Photoluminescence Spectroscopy**

Photoluminescence is a key property of semiconductor QDs such as SiQDs. This technique can be used to calculate the emission wavelength and the optimum excitation wavelength. This information is vital in the design of imaging experiments using these materials.

The photoluminescence spectrum was taken for alkyl-functionalised SiNPs dissolved in a suitable solvent; in a quartz cuvette (10 mm × 10 mm), using a Perkin-Elmer LS55 spectrofluorimeter. A background was corrected by subtracting the spectrum of the pure solvent under the same conditions.

### **2.3.3.3. Quantum Yield**

By calculating the quantum yield we are able to estimate the quantum efficiency. This value is a ratio of photons in compared to the photons out. This is particularly important for materials for imaging applications. This can be calculated either as an “absolute” value or a “relative” value. It is typically calculated using the simpler “relative” method where it is compared to a material of known quantum yield.

A reliable “relative” quantum yield can be calculated using a method published by Williams *et. al.*<sup>175</sup> Firstly solutions of the sample at varying concentrations in a suitable solvent were prepared, and the absorbance was measured at the excitation wavelength. For each dilution the emission spectrum was taken and the area under the peak was calculated. Only samples with an absorbance between 0.1 and 0.01 were used. The absorbance was plotted against the area and compared to a reference of known quantum yield (quinine sulphate, 54.6 % at 340 nm excitation). The reference was prepared in 0.5 M H<sub>2</sub>SO<sub>4</sub> solution at different concentrations and the procedure repeated as above. The gradient of both the sample and the reference were used in the following equation to give the quantum yield of the sample. Using the gradient of both of the above plots the following equation was used to calculate the quantum yield.

$$Q = Q_R \left( \frac{Grad}{Grad_R} \right) \left( \frac{\eta^2}{\eta_R^2} \right) \quad (14)$$



Where  $Q$  is the quantum yield,  $Q_R$  is the quantum yield of reference,  $\eta$  = refractive index of sample,  $\eta_R$  = refractive index of reference.

## 2.4. Thermal Analysis and Measurement of Thermoelectric Properties

### 2.4.1. Thermal Gravimetric Analysis and Differential Scanning Calorimetry.

Thermogravimetric analysis (TGA) and differential scanning calorimetry (DSC) are useful techniques when considering the thermal stability of materials produced and the ligand coverage of the silicon particles produced. TGA is a gravimetric trace which gives weight change over both dynamic and isothermal heat programs. DSC gives an indication of the nature of the process for example a trough in the heat flow is associated with an endothermic process such as phase change and a peak in the heat flow an exothermic process such as combustion. Using these two techniques in conjunction gives more information on the process shown in DSC for example a trough in heat flow in DSC with a drop in mass on the TGA is indicative of evaporation however without a drop in weight is indicative of a process such as a glass transition or melting.

TGA and DSC analysis was performed using a METTLER-TOLEDO TGA-DSC1. The solid sample (approx. 5 mg) was placed in a 40  $\mu$ L aluminium pan and measurements were taken while heating the sample between the specified temperature limits. The background measurements were taken while heating the empty pan over the same temperature range.

### 2.4.2. Measurement of Thermoelectric Properties

#### 2.4.2.1. Measurement of Thermoelectric Properties of Phenylacetylene Functionalised SiNPs

A four probe DC current equipment was used to measure the room temperature electrical resistivity. A current  $I = 10$  mA was applied between two probes and the voltage difference  $V$  generated at the other two probes was measured. The resistivity  $R$  was calculated using:

$$R = \frac{V}{I} \times F \times C \times d \quad (15)$$

Where  $F$  and  $C$  are geometrical correction factors and  $d$  the pellet thickness. In both measurements the data was taken at different regions of the pellet. The individual resistivities reported are the average of two measurements with applied electrical current in two opposite directions. The contacts are spring loaded pressure contacts. The influence of the parasitic capacitance is ignored because the measurement was carried out under DC conditions as thermoelectric devices operate in DC mode.

The Seebeck coefficient was measured at room temperature using a hot probe apparatus at Cardiff University.<sup>176</sup> This technique is a relative method and uses a hot and ambient probe to

create a temperature difference. The probes contain a thermo couple so the potential between the hot and ambient probes for both materials in the thermocouple are measured.

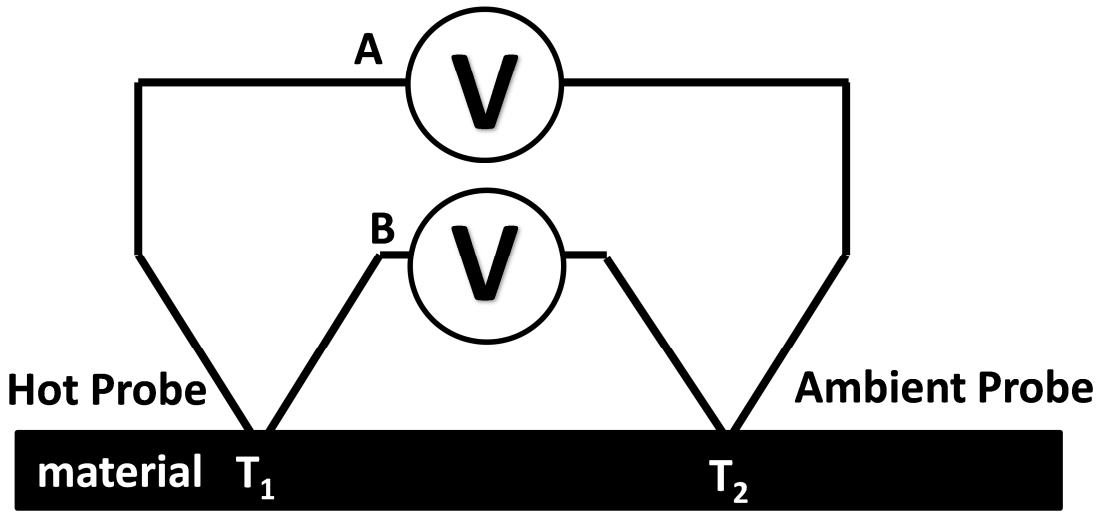


Figure 13: Schematic diagram showing the hot probe experimental setup.

This technique uses the difference in potential between circuit A and B ( $\Delta V$ ) and the difference in temperature ( $\Delta T$ ) between  $T_1$  and  $T_2$  to obtain the Seebeck coefficient ( $S$ ):

$$S = -\frac{\Delta V}{\Delta T} \quad (16)$$

All measurements were taken at different points near the centre of the material.

Thermal diffusivity measurements were performed at 373 K and 423 K using an Anter Flashline 3000 instrument. Measurements were made on pellets of phenylacetylene functionalised SiNPs. This instrument determines both the thermal diffusivity ( $\alpha$ ) and the heat capacity ( $C_p$ ) of the sample. The thermal conductivity ( $\kappa$ ) is calculated from the relationship:

$$\kappa = \alpha C_p \rho \quad (17)$$

Where  $\rho$  is the sample density which was estimated by dividing the mass by the volume calculated from the pellet dimensions. For the determination of the heat capacity, side-by-side testing of a reference material, Pyroceram<sup>TM</sup> 9606, of known heat capacity, was carried out. The procedure used for the determination of the heat capacity has been described in detail.<sup>177, 178</sup>

#### 2.4.2.2. Measurement of Thermoelectric Properties of Terthiophene Functionalised SiNPs

The electrical resistivity and the Seebeck coefficient was measured by a multifunctional apparatus developed by García-Cañadas *et. al*. This apparatus uses 4 multifunctional probes that

comprise of a junction of two conductors at the tip and serve as both thermocouples and electrical contacts. Additionally one of the probes has an inbuilt heater which allows a temperature gradient to be established in the sample for the measurement of the Seebeck coefficient (**Figure 14:**).<sup>179</sup> This technique is not geometry specific and has a maximum experimental error of 4% and 5% for electrical conductivity and Seebeck coefficient respectively. The measurements were taken on pellets 13 mm in diameter and 1.5 mm thick at room temperature.

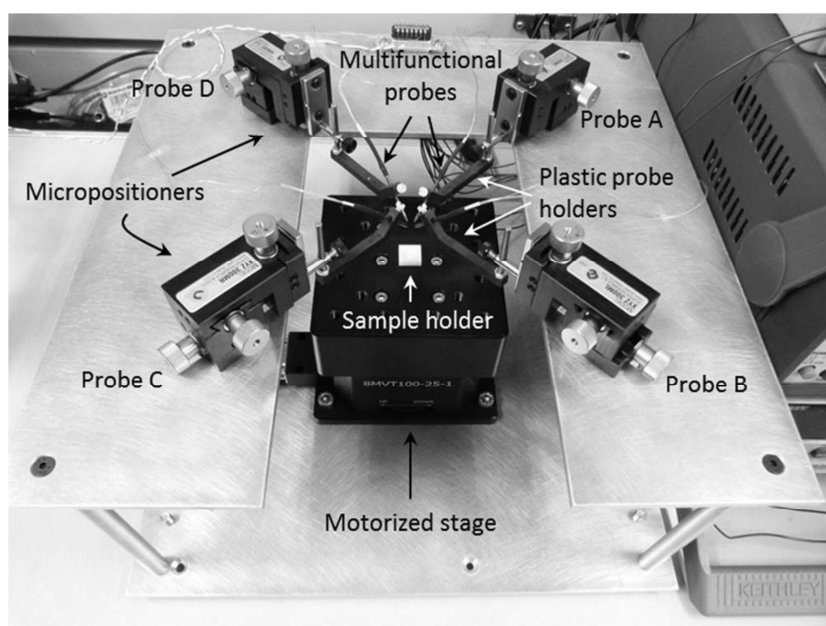


**Figure 14: Photograph of multifunctional electrical resistivity/ Seebeck coefficient measurement apparatus.**<sup>179</sup>

The thermal diffusivity and heat capacity were measured using a Netzsch thermal diffusivity/ conductivity instrument, LFA 447. The materials were run using Pyroceram™ 9606 as a standard so that the heat capacity could be accurately measured. Using **Equation 10** the thermal conductivity is calculated. This apparatus requires a density to calculate the thermal conductivity. The density of the pellet was estimated by dividing the pellet mass by the volume calculated from the dimensions of the pellet. Measurements were taken at 30, 50, 75, 100, 125 and 150 °C and each reported value is the average of 3 measurements.



**Chapter 3:**  
One-Pot Bottom Up  
Synthesis of Alkyl  
Functionalised Silicon  
Nanoparticles by  
Micelle Reduction.

### 3.1. Overview

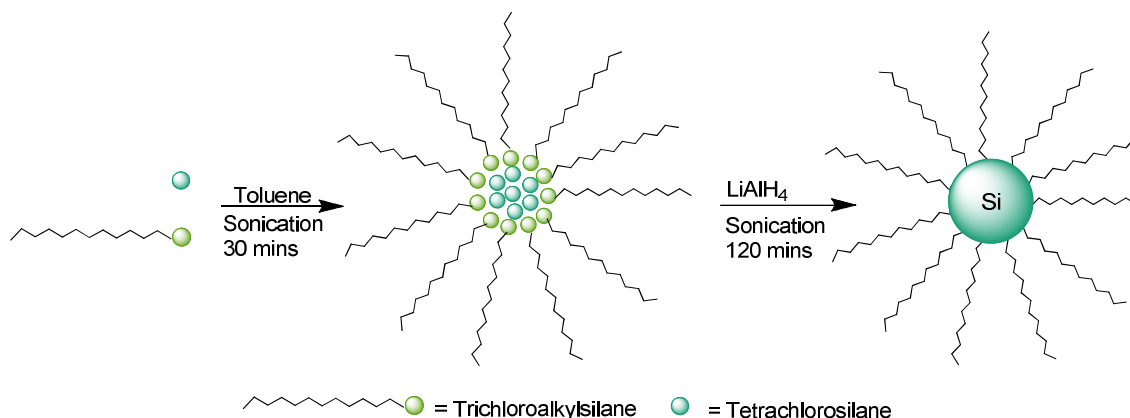
As discussed previously, the key disadvantages of top down methods for the synthesis of SiNPs is scalability and with regards to electrochemical etching, the toxicity of reagents such as hydrofluoric acid. As a result, bottom up synthetic approaches are far more attractive. One such method is the reduction of micelles of a precursor molecule using a suitable reducing agent.<sup>87, 88, 94, 96</sup> Many approaches use surfactants to control the size of micelles and ultimately the size of the resulting nanoparticles.<sup>49, 74, 78, 180, 181</sup> However these processes require a lot of purification to remove surfactants after the passivation step. In 2011 Wang *et. al.* reported a synthetic procedure that used trichloroalkylsilanes as a surfactant. This surfactant was incorporated into the resulting particle to achieve corresponding alkyl functionalisation.<sup>91</sup> This one-pot method removes the extra purification steps required as a result of using a conventional surfactant such as tetraoctylammonium bromide.

In the following study, alkyl functionalised SiNPs were synthesised using surfactants of different alkyl chain length and employing the previously published one-pot micelle reduction method<sup>91</sup>. The surfaces of these particles were studied to understand how the length of the alkyl chain length and how the quenching agent can affect the surface coverage and impurities on the surface. In cases where SiNPs showed hydride functionality, an additional process was introduced to fully cap the surface. Thermal hydrosilylation was run by adding the sample to a mixture of toluene of the corresponding 1-alkene and heating at reflux for 5 hours.<sup>81</sup>

Characterisation shows the successful synthesis of crystalline alkyl functionalised SiNPs and shows changes in surface functionality depending on the quenching agent and the alkyl chain length of the surfactant used. Surface characterisation shows that this is related to variation in the susceptibility of the surface to oxidation by the two quenching agents.

### 3.2. Synthesis of Alkyl Functionalised SiNPs

Based on a preparation by Wang *et. al.*<sup>91</sup> an emulsion of micelles of alkyl-SiCl<sub>3</sub> and SiCl<sub>4</sub> was reduced using LiAlH<sub>4</sub> to form a suspension of alkyl functionalised SiNPs, This method was carried out for 4 different alkyl chain lengths. Hexyl, octyl, dodecyl and octadecyl functionalised SiNPs were produced: primarily to investigate how the surfactant alkyl chain length affected the levels of Si-O observed, but additionally to investigate whether the chain length had any effect on the particle size produced **Scheme 12**. After the reduction step, any excess reducing agent was quenched using either methanol (pK<sub>a</sub>=15.5), as reported in Wang's method, or alternatively ethanol (pK<sub>a</sub> = 15.9), which is less acidic and has more steric bulk. This would limit the level of oxidation caused by the quenching solvent.



**Scheme 19: One pot micelle reduction synthesis of alkyl functionalised SiNPs.**

This synthetic procedure gave a yield of approximately 120 mg of yellow gel like material. This is moderately high when compared to top down methods such as electrochemical etching.<sup>106</sup>

### 3.3. Characterisation of Alkyl Functionalised SiNPs

#### 3.3.1. Studies of Functionalisation, Oxidation and Incomplete Capping

Wang's one-pot method was extended to include surfactants of varying chain length ( $\text{C}_6\text{-C}_{18}$ ), using methanol as a quenching reagent. Additionally, the procedure was modified to explore the use of ethanol as a quenching reagent.

Using FTIR as a spectroscopic tool it was possible to analyse the differences between the surface coverage of different SiNPs samples which were prepared using different trichloroalkylsilane surfactants and/ or quenching agents. Although the alkyl peaks were essentially identical in all samples, the effect on the free Si-H on the surface of the SiNPs differed with varying chain lengths and was highly dependent on quenching agent.

FTIR spectra for each surfactant chain length show a level of alkyl functionalisation irrespective of the quenching method. The spectra are shown in **Figure 15** and **Figure 16** show strong features which are characteristic of alkyl groups, such as three strong sharp peaks at 2980, 2921, and 2852  $\text{cm}^{-1}$ , which are representative of the C-H stretching modes, as well as observed peaks at approximately 1460 and 1261  $\text{cm}^{-1}$ , representing the C-C and Si-C stretching and bending modes respectively. There is also a presence of a peak at 1354  $\text{cm}^{-1}$  which is representative of C-H scissoring. The combination of these peaks shows successful capping on all accounts of this synthetic procedure.

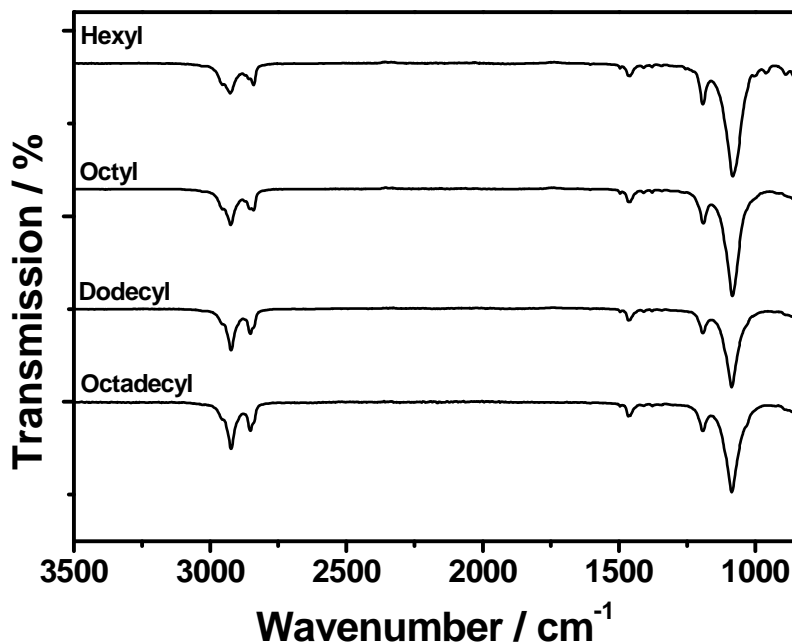
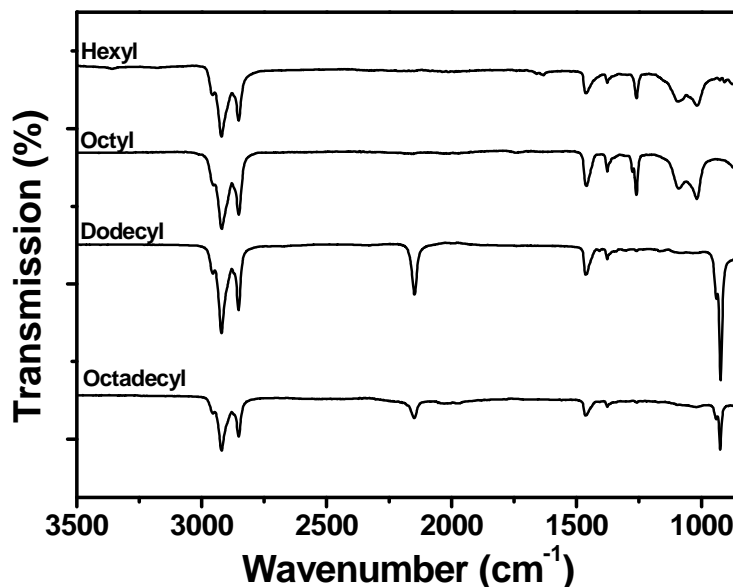


Figure 15: FTIR of hexyl, octyl, dodecyl and octadecyl functionalised SiNPs when methanol was used as a quenching agent.

In addition to the peaks expected for the alkyl functionalisation of silicon, the initial study of this method by Wang *et. al.* described a strong broad peak observed in the region 1100-1000 cm<sup>-1</sup>, with 2 maxima at approximately 1090 and 1020 cm<sup>-1</sup>. This peak shape is characteristic of Si-O-C stretching and therefore highly indicative of surface oxidation.<sup>96</sup> In Wang's method, the oxidation of any unpassivated regions of the SiNPs is likely to occur during the quenching of unreacted LiAlH<sub>4</sub> with excess methanol. The choice of the quenching reagent may have an effect on the level of SiNP oxidation. One way to limit the extent of surface oxidation would be to use a less acidic and more sterically hindered alcohol as a reagent such as ethanol (**Figure 16**) or to use an oxygen free salt such as copper (II) chloride as described by Dung *et. al.*<sup>93</sup> However the use of copper (II) chloride makes the sample more difficult to purify.





**Figure 16:** FTIR of hexyl, octyl, dodecyl and octadecyl functionalised SiNPs when ethanol was used as a quenching agent.

Quenching both the hexyl and octyl functionalised SiNPs with ethanol gave a very similar results to the corresponding SiNPs quenched with methanol. However some significant differences can be observed in the spectra obtained for both the dodecyl and octadecyl functionalised SiNPs. When quenched with methanol the FTIR spectra showed strong Si-O-C peaks. However when quenched with ethanol a significant reduction in the intensity and broadening of the Si-O-C peaks relative to the Si-C and C-C stretch were observed. The peak observed is more characteristic of the native oxide observed in top down approaches to alkyl functionalised SiNPs.<sup>81</sup> In addition to this a sharp peak at 2149 cm<sup>-1</sup> was observed, which is characteristic of Si-H. In both of these samples the Si-H peak remained unchanged when left to age under atmospheric conditions for 1 week (**Figure 17**).

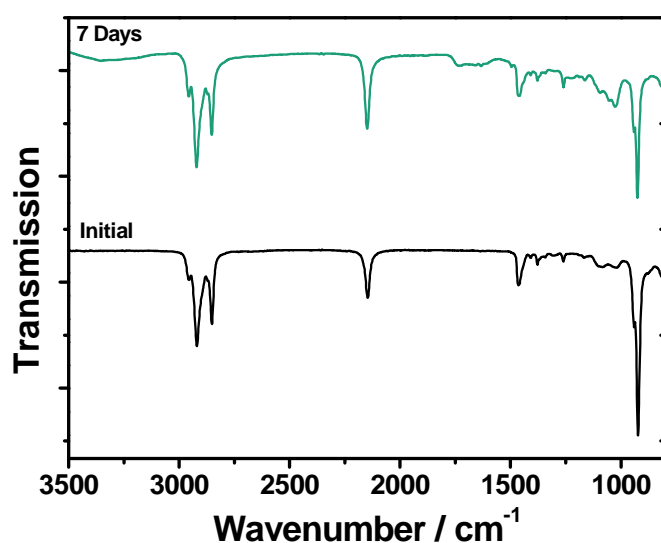


**Figure 17: Aging of FTIR spectrum of dodecyl functionalised SiNPs showing Si-H stretch showing the initial and after 7 days spectrum.**

When the micelle is reduced with  $\text{LiAlH}_4$ , some areas of the particle are not functionalised by the alkyl chain, leaving some areas of the particles terminated with hydrogen. This explains the observation of the Si-H peak at  $2149\text{ cm}^{-1}$  on both dodecyl functionalised samples and the octadecyl functionalised samples but does not explain the lack of a Si-H stretch for the hexyl and octyl samples.

The quenching of the reaction holds the key to explaining this. The quenching of the reaction with a primary alcohol means that the Si-H functionality is susceptible to alkoxylation or oxidation from the solvent. In the samples of dodecyl and octadecyl functionalised SiNPs the steric influence around the particle is high enough to protect the Si-H surface functionality from reaction with ethanol but the octyl and hexyl functionalised particles do not prevent such reactions as they do not display enough steric influence. In the case of methanol this effect is not sufficient on all accounts.

Initial analysis of the products of this method attributed the high oxide levels observed in the hexyl functionalised SiNPs to the Si-H bonds undergoing oxidation with long term exposure to air.<sup>91</sup> The FTIR spectra were taken immediately after drying so there has been minimal exposure to air. In addition FTIR aging of partially passivated SiNPs (dodecyl) shows no significant oxidation of the Si-H functionalities after 1 week (**Figure 17**). However rapid oxidation was observed in the octyl and hexyl samples. It has been shown that the introduction of a protic solvent such as water or a primary alcohol can lead to oxidation.<sup>182</sup> The quenching step of  $\text{LiAlH}_4$  introduced ethanol in to the reaction flask prior to exposure to air. Previous FTIR data of alkoxy SiNPs show a relatively sharp Si-O-C peak, observed at  $1091\text{ cm}^{-1}$ , rather than the typically broad Si-O peak observed in

most alkyl functionalised SiNPs<sup>96, 98, 183</sup>. The spectra for the alkoxy SiNPs have similar-shaped oxide profiles as those for both the hexyl- and octyl- functionalised SiNPs. This suggests that the higher oxide observed in these two samples is a result of the reaction of ethanol with the exposed Si-H surface, which is a consequence of incomplete surface functionalisation. This reaction can occur at room temperature when stirred vigorously.<sup>98</sup> The longer chain capping layers act as a steric barrier to the ethanol preventing reaction with the Si-H sites and thus lower Si-O levels observed.

As a result of these observations, an extra hydrosilylation was carried out on the dodecyl and octadecyl functionalised SiNPs when ethanol was used as a quenching reagent for two reasons; to confirm the presence of Si-H functionality on the surface and to fully passivate the surface of the SiNPs. The use of thermally induced hydrosilylation using the respective 1-alkene resulted in a reduction in the intensity of the Si-H peak relative to the C-C /C-Si stretch at  $1464\text{ cm}^{-1}$  in both cases. Additionally in both cases a slight increase in the relative intensity of the peak corresponding to SiO could be observed.

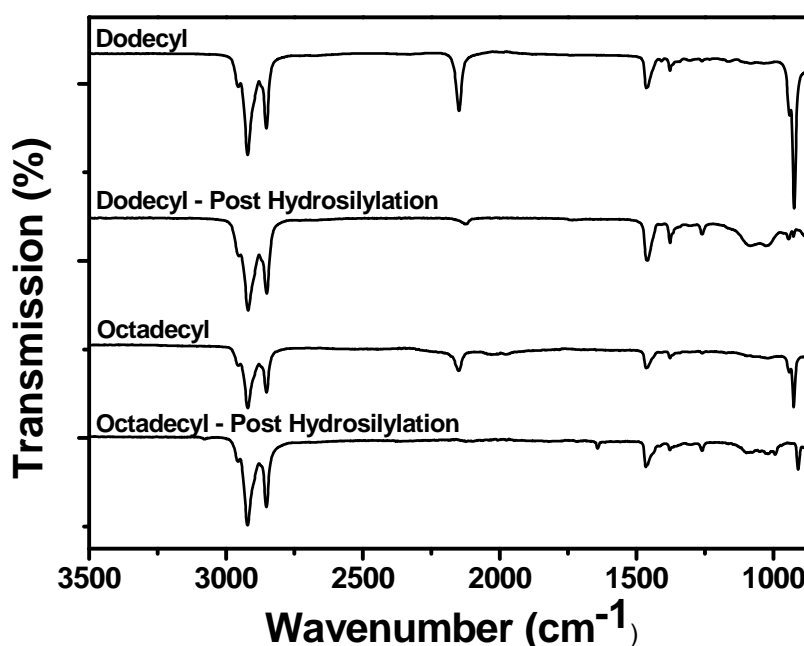


**Figure 18: FTIR of dodecyl and octadecyl functionalised SiNPs before and after thermal hydrosilylation with the corresponding 1-alkene.**

The increase in the relative intensity of SiO after the reflux step cannot be attributed to alkoxy capping due to the absence of a quenching reagent and the shape of the peak, but the increased temperature and the presence of oxygen and contaminants in the reagents and solvents (e.g. water) would lead to further oxidation.

<sup>1</sup>H-NMR was also used to analyse the surface functionalisation of ethanol-quenched octyl and dodecyl functionalised SiNPs. For octyl functionalised SiNPs, the <sup>1</sup>H-NMR spectra display alkyl and

alkoxy functionalisation. In this spectrum a symmetrical multiplet can be observed at 3.66 ppm representing the two CH<sub>2</sub> protons and a small triplet at 0.78 ppm representing the CH<sub>3</sub> protons (**Figure 19**). These features are absent from the NMR spectrum of the dodecyl- functionalised SiNPs. The <sup>1</sup>H-NMR for both the dodecyl and the octyl functionalised samples supports the alkyl capping of SiNPs. These spectra show three proton environments, one at 1.25 ppm which is characteristic of a CH<sub>2</sub> attached to silicon, as it is shifted downfield from the other CH<sub>2</sub> protons which are shown at 1.18 ppm, and the CH<sub>3</sub> peak is observed at 0.55 ppm.

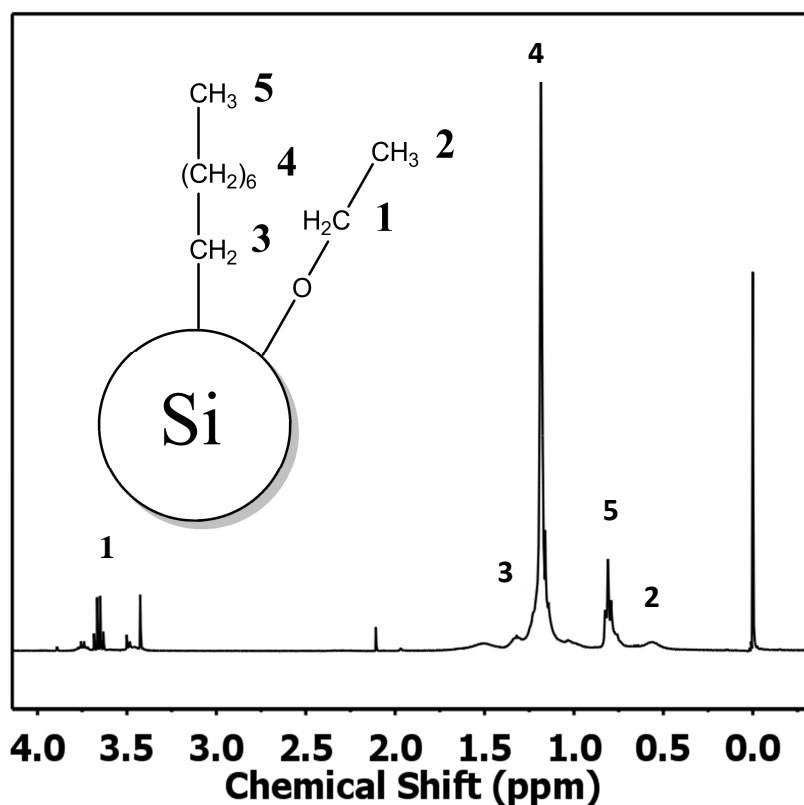


Figure 19: <sup>1</sup>H-NMR spectrum obtained from octyl-functionalised SiNPs dissolved in CDCl<sub>3</sub>.

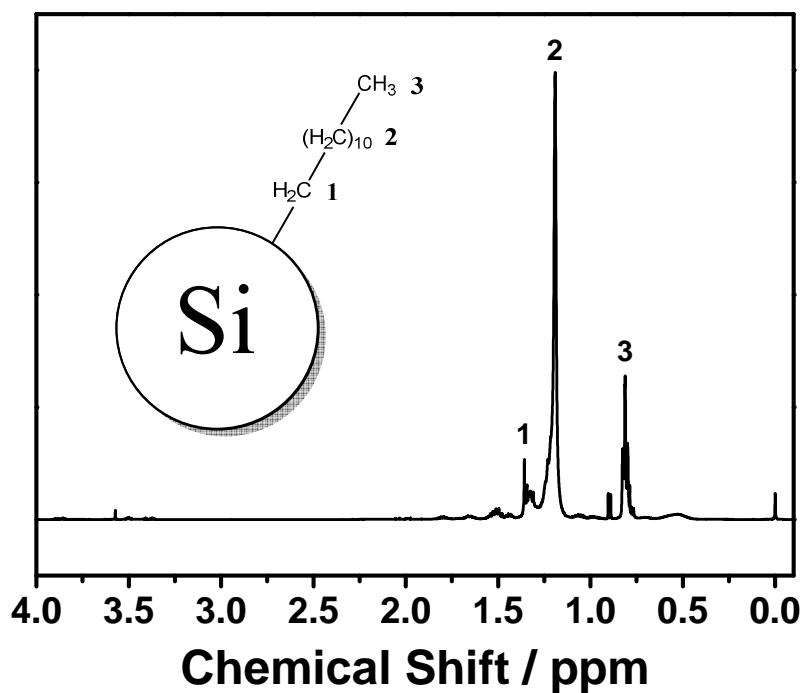


Figure 20:  $^1\text{H}$ -NMR spectrum obtained from dodecyl-functionalised SiNPs dissolved in  $\text{CDCl}_3$ .

### 3.3.2. Microscopy and Particle Size

TEM micrographs for each sample are displayed in **Figure 21**. The mean diameters and standard deviation from the measurement of 100 particles for each functionalisation is given in **Table 1**. The mean diameter differs slightly for each capping agent (surfactant) used and for hexyl, octyl and dodecyl shows a pattern of increasing mean size with increasing chain length. However, the octadecyl surfactant breaks this pattern. It is to be expected that the surfactant will affect the size as shown in the results, but the way in which the increase of alkyl chain affects size requires further study, since these results do not show a definitive pattern and the pattern may be related to inaccuracy in measuring particles using the software

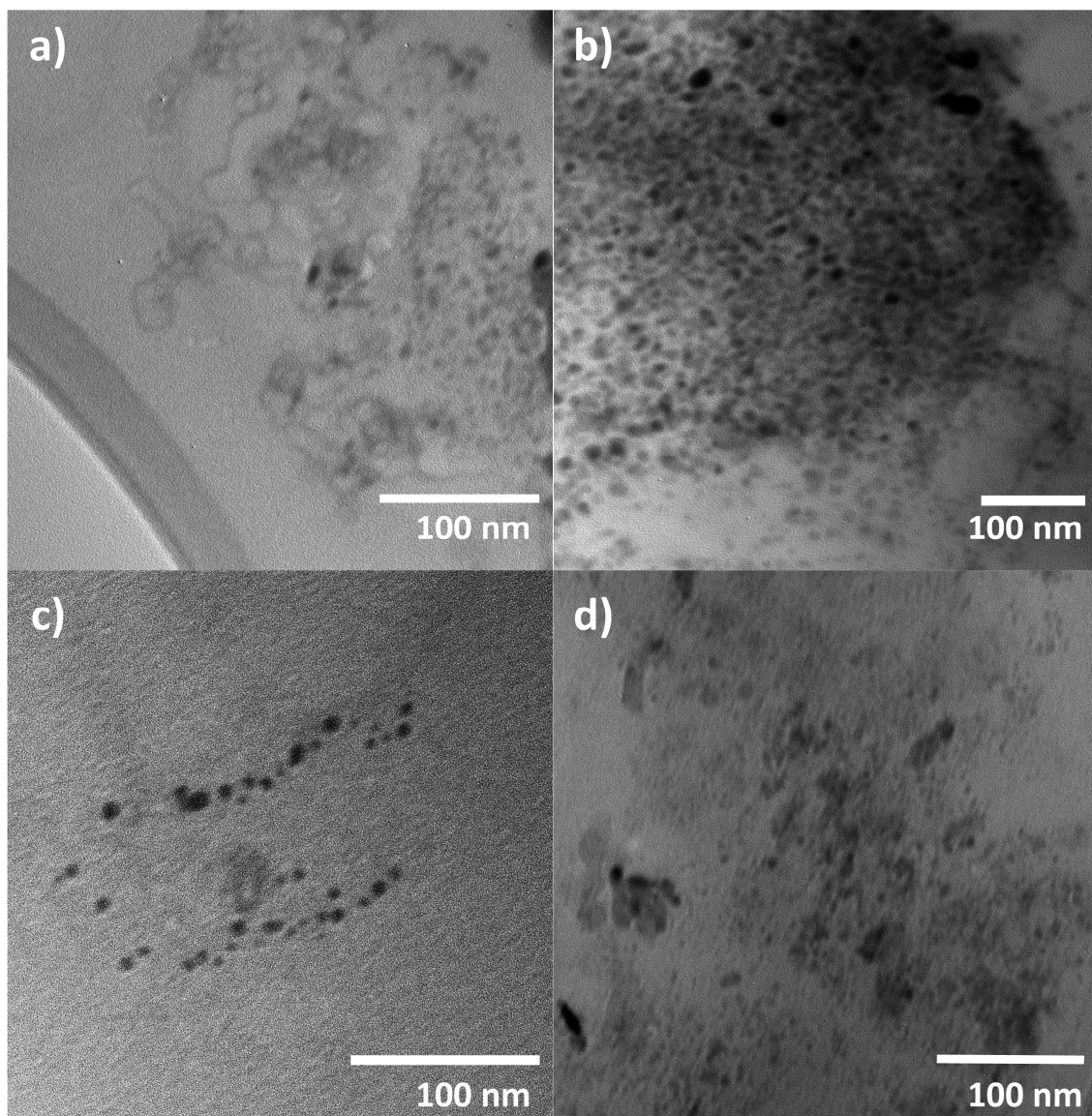
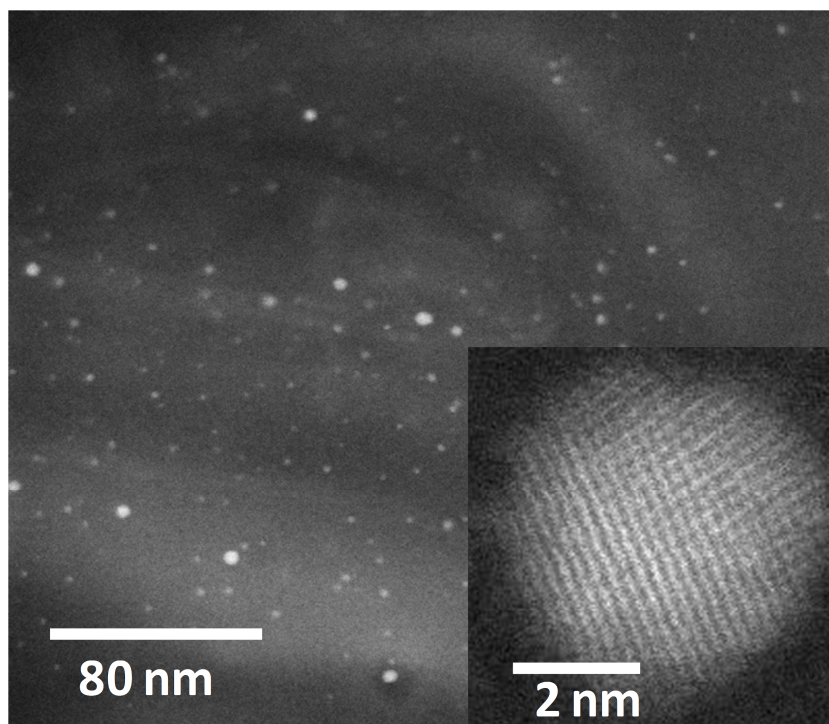


Figure 21: Low resolution TEM image showing a)hexyl b)octyl c) dodecyl d)octadecyl functionalised SiNPs synthesised by micelle reduction.

Table 1: The mean diameter and standard deviation of SiNPs from a sample of 100 particles.

Capping	Mean diameter (nm)	Standard deviation (nm)
Hexyl	6.0	1.60
Octyl	6.3	1.61
Dodecyl	6.5	1.94
Octadecyl	6.2	1.71



**Figure 22: SuperSTEM image showing the distribution of sizes of alkyl-functionalised SiNPs obtained from the reduction of hexyltrichlorosilane/SiCl<sub>4</sub> micelles, inset: high resolution Z-contrast STEM image of an individual SiNP showing it to be crystalline of alkyl-functionalised SiNPs.**



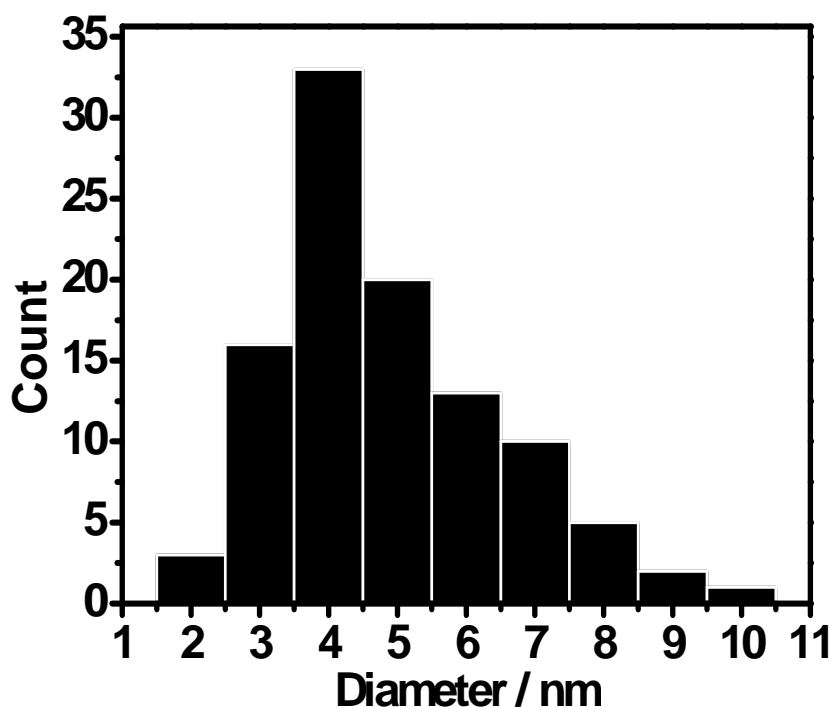


**Figure 23:** Histogram showing an example size distribution of alkyl-functionalised SiNPs.

The Z-contrast STEM image (**Figure 22**) for hexyl functionalised SiNPs also shows well defined SiNPs. These images were used to investigate the monodispersity of the sample. The histogram in **Figure 23** shows the range of 100 particle diameters within the sample. The range is moderately wide with particles varying from 2 to 10 nm being produced. In addition the maximum is at approximately 4 nm which is 2 nm lower than the mean diameter. In addition, high resolution STEM imaging showed that the particles are crystalline in nature and the Z-contrast STEM image shown in the inset of **Figure 22** shows the lattice fringes of the crystalline particle. The measured lattice fringe spacing in these crystalline particles is 0.31 nm, corresponding to the (111) interplanar spacing of the diamond cubic structure of silicon.<sup>184</sup>

### 3.3.3. XPS and XAS

XPS and XAS were used to give an indication of the elemental composition of the silicon particles produced. The peaks observed from each capping layer are very similar. **Figure 24:** is a typical XPS survey spectrum for the alkyl functionalised SiNPs (dodecyl) produced. From this spectrum peaks for O1s C1s Si2p and Si2s can be observed as well as the two peaks for Au4f. All XPS spectra are calibrated to the Au4f peak.



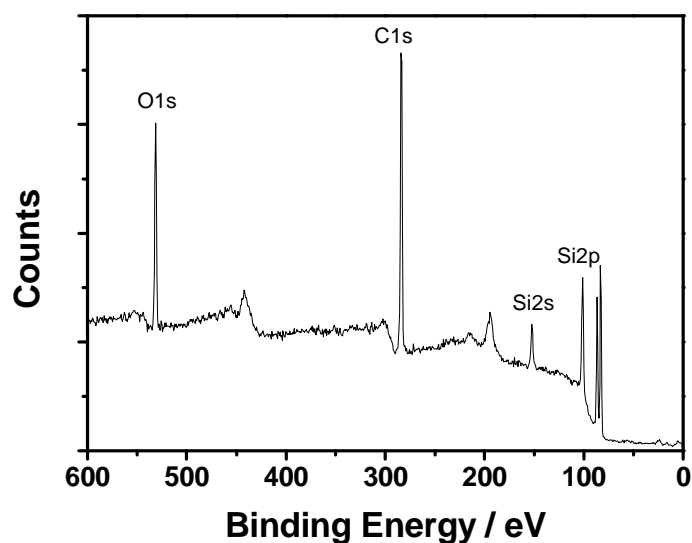


Figure 24: XPS spectra obtained from dodecyl functionalised SiNPs showing Survey spectrum. Photoelectron spectrum was collected with incident photon energy of 630 eV.

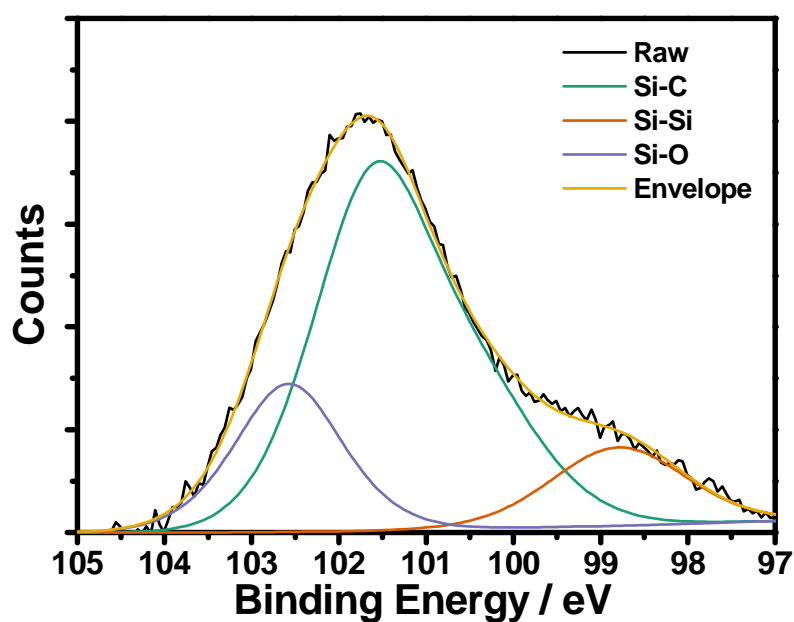
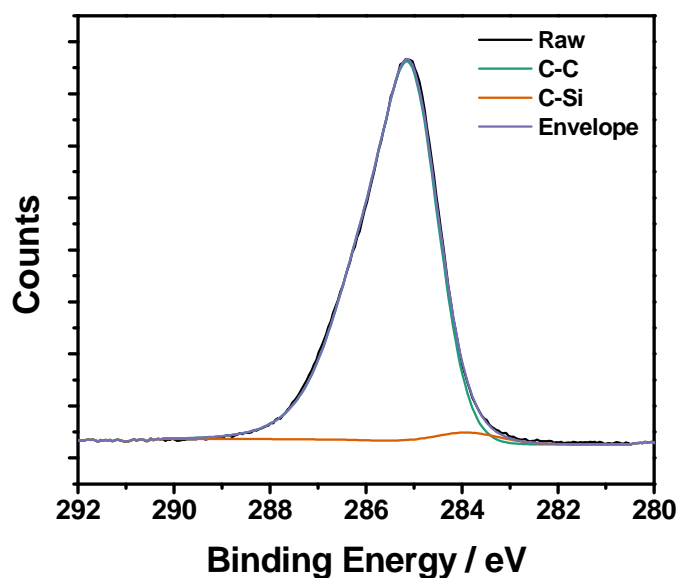


Figure 25 : High resolution spectrum XPS spectrum obtained from dodecyl functionalised SiNPs showing Si2p region. Photoelectron spectrum was collected with incident photon energy of 630 eV.

In **Figure 25**, the Si2p spectrum for dodecyl- functionalised SiNPs is fitted with three components: at 99.92 eV, 101.53 eV, and 102.73 eV representing contributions from Si-Si, Si-C and Si-O respectively.<sup>185, 186</sup> The peak at 99.92 eV representing the Si-Si bonding within the centre of the

nanoparticles contributes 14.2 % of the total spectrum area within the fitted energy window. The remaining 85.8 % is from Si-C and Si-O at the particle surface. Of this remainder 63.8 % is from Si-C and 22 % is Si-O meaning an estimated 75 % of the available surface has undergone alkyl capping. This compares favourably with H-terminated Si (111) surfaces bound by organic monolayers where 50 % surface coverage is typical.<sup>111, 112</sup>



**Figure 26:** High resolution spectrum XPS spectrum obtained from dodecyl functionalised SiNPs showing C1s region. Photoelectron spectrum was collected with incident photon energy of 630 eV.

In **Figure 26**, the C1s spectrum for dodecyl- functionalised SiNPs is fitted with two components: C-C at 284.9 eV and C-Si at 283.9 eV. 91.8 % of the spectrum area is from C-C within the carbon chains and the remaining 8.2% is made up by the Si-C where the passivating layer is bound to the silicon centre. The ratio of the area of the spectrum represented by each component is close to 1:11, which is the exact ratio of Si-C to C-C bonds in the functionalised SiNPs.

In **Figure 27** the O1s spectrum for dodecyl- functionalised SiNPs is fitted with one component; this is a peak representative of Si-O and is in part due to chemical oxidation and in part due to X-ray induced oxidation.

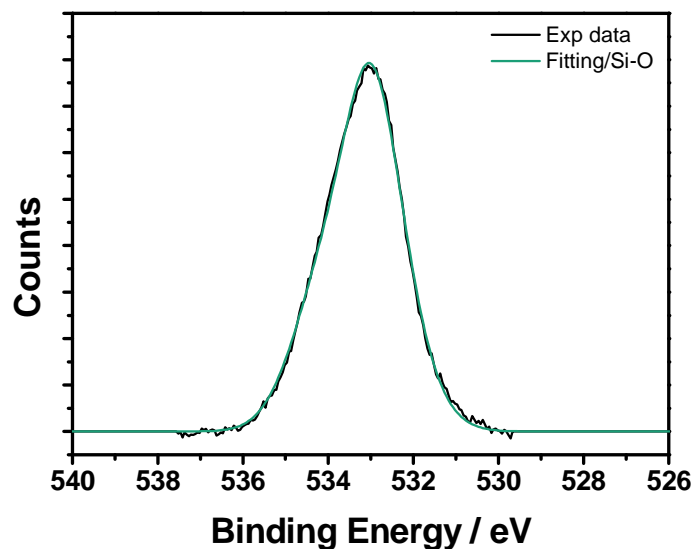


**Figure 27:** High resolution spectrum XPS spectrum obtained from dodecyl- functionalised SiNPs showing O1s region. Photoelectron spectrum was collected with incident photon energy of 630 eV.

**Figure 28** shows the XAS spectrum in total electron yield mode over the Si *L* edge for a thick film of dodecyl functionalised SiNPs prior to x-ray irradiation. The XAS profiles collected over the softer *L* edge allow highly localized chemical and structural information to be obtained thus taking advantage of the narrow spatial separation between the initial photoionization upon X-ray absorption and the final carrier combination events. At the silicon *L*<sub>2,3</sub> edge this spatial-separation is approximately 1 nm,<sup>187</sup> which is smaller than the diameters of the nanocrystals. A general noticeable trend is the increase of the total electron yield towards higher photon energies. This is attributed to the increasing absorption coefficient ( $\mu$ ) as a result of the electron multi-scatterings from high energy photoelectrons into multiple low energy Auger electrons.<sup>188</sup> The doublet peaks at 105.7 and 106.5 eV are strongly characteristic of silicon oxide.<sup>189</sup> Similar doublet features have been observed close to 105 eV and identified as such within porous silicon and in thin (1.1–2.6 nm thick) Si/SiO<sub>2</sub> layers.<sup>190, 191</sup> The broad peak at 115 eV is close to that for silicon oxide at 115.3 eV.<sup>192, 193</sup> At the excitation energies used here, the escape depth of the Auger and low energy electrons detected within the TEY is  $\sim$ 5 nm, thus the effective sampling depth is largely confined to sample surfaces.

At lower energy, much weaker shoulders can be observed in the spectrum: one at 99.9 and one at 100.5 eV, which are characteristic of elemental silicon and SiC respectively.

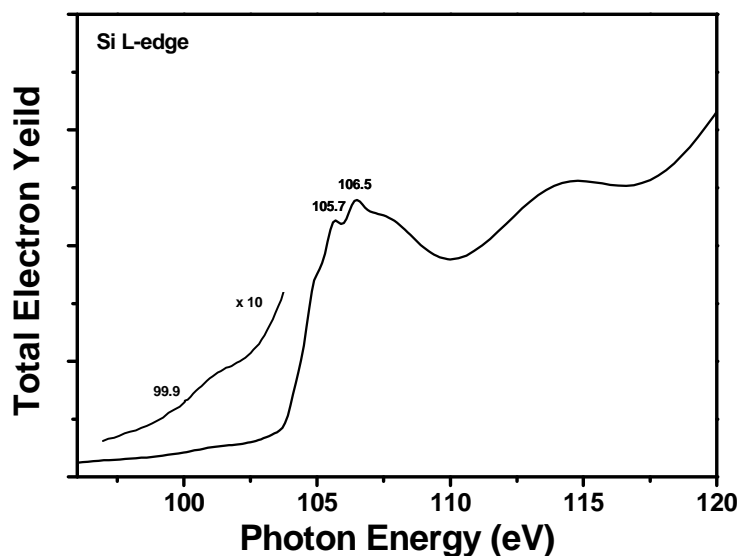


**Figure 28:** TEY for thick film of dodecyl-functionalised SiNPs over the Si L absorption edge. The spectrum region from 97–104 eV is overlaid and scaled x 10

### 3.4. Optical properties of SiNPs

The origin of the photoluminescence observed in **Figure 29** is complicated by the combination of both indirect and direct band gap transitions present in SiNPs.<sup>98</sup> However, there is strong theoretical evidence suggesting that 1-2 nm SiNPs with a hydrogen or carbon-terminated surface have direct band gap optical transitions that lead to photoluminescence in the blue region<sup>78, 194</sup>.

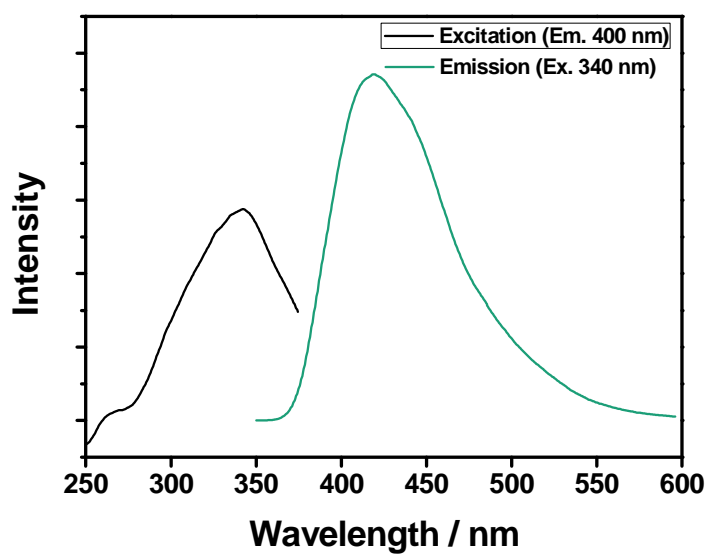


Figure 29: PL spectra for alkyl functionalised SiNPs. Excitation spectrum (Emission wavelength = 400nm, emission bandwidth = 10nm, excitation bandwidth = 10nm) Black and emission spectrum (excitation wavelength = 340 nm emission bandwidth = 10nm, excitation bandwidth = 10nm) Green

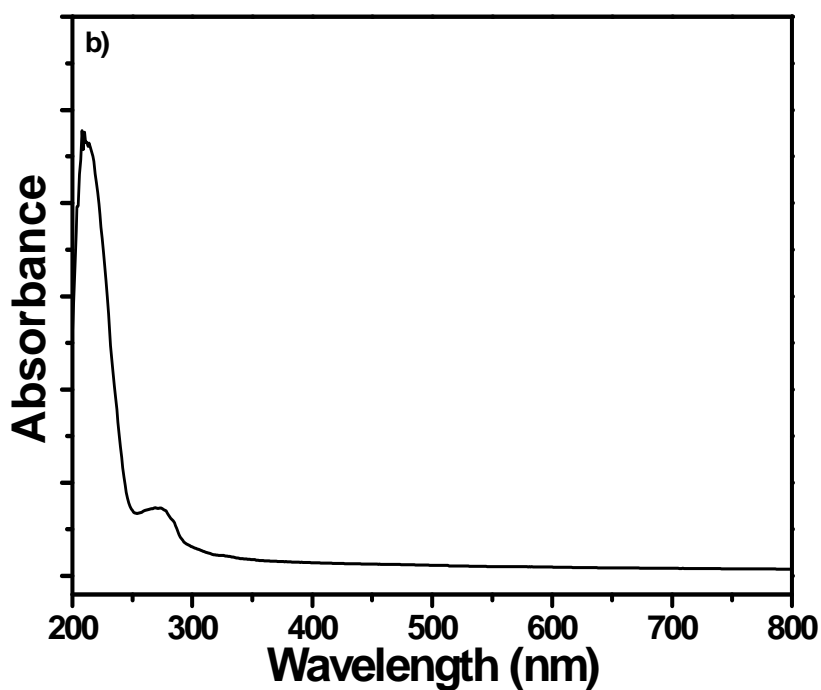


Figure 30: UV/Vis Spectrum for alkyl- functionalised SiNPs in hexane.

**Figure 29** and **Figure 30** show the room temperature PL and UV/Vis spectra respectively. The PL emission shows a broad multi component emission in the blue region with a maximum at 407 nm when excited at the optimum wavelength of 340 nm. The irregular shape of this peak suggests a complex mix of direct and indirect band gap transitions<sup>68</sup>

The UV/Vis spectrum shows a gradual increase in absorbance from high to low wavelengths as a result of increasing levels of scattering, as expected with any dispersions of this nature. However a shoulder is observed at 280 nm which is evidence of an absorption rather than scattering. This is evidence of the successful synthesis of quantum dots.

### 3.4.1. Quantum yield

**Figure 31** and **Figure 32** show the UV/Vis and PL spectra of SiNPs respectively, at different concentrations. Using all spectra where the absorbance at 340 nm is greater than 0.01 and less than 0.1 the integrated intensity has been plotted against the absorbance for both the dodecyl functionalised SiNPs and the quinine sulphate reference as shown in **Figure 33**.

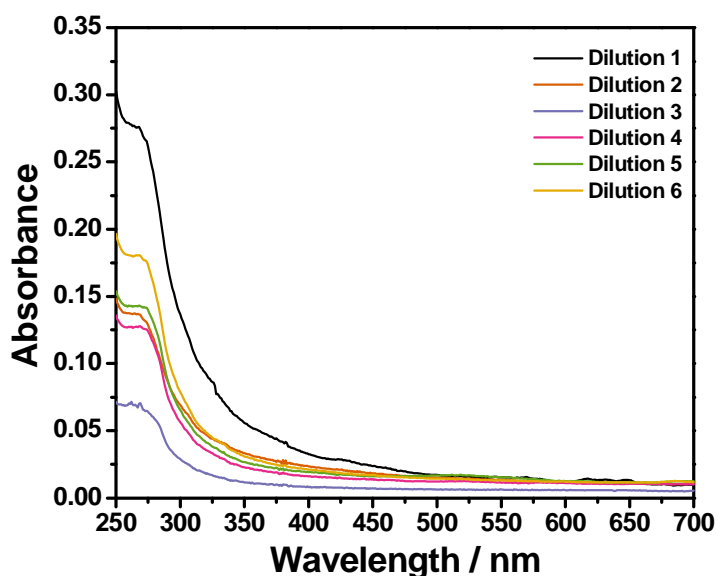


**Figure 31:** UV/Vis spectra at varying dilutions of alkyl functionalised SiNPs in hexane

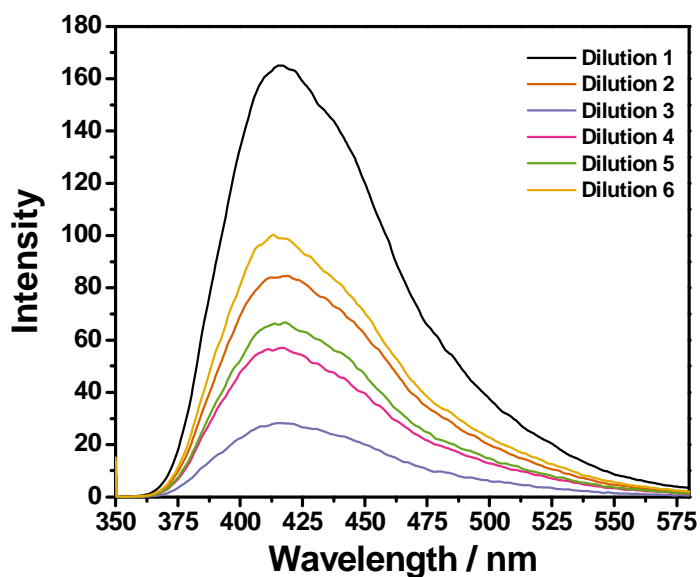


Figure 32: Emission spectrum; Excitation wavelength = 340 nm excitation bandwidth = 10 nm emission bandwidth = 2.5 nm at varying concentration of alkyl functionalised SiNPs in hexane

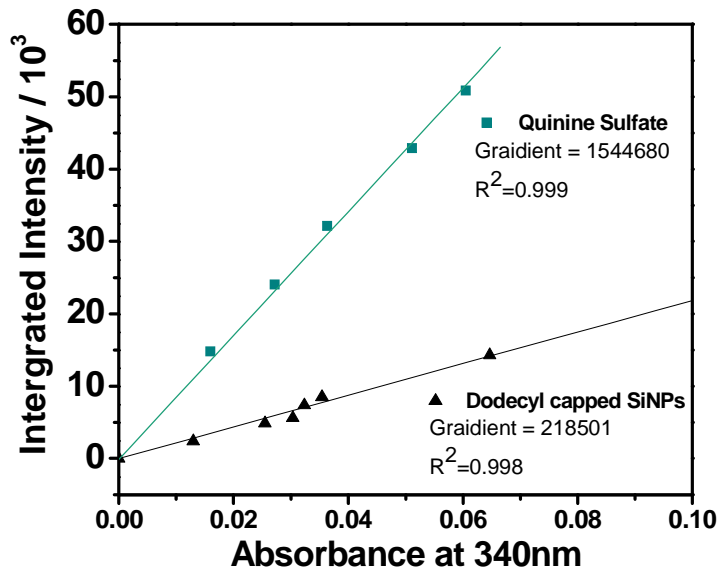


Figure 33: Plotted integrated intensity of emission against absorbance for both alkyl functionalised SiNPs in hexane and quinine sulphate in 0.1 M H<sub>2</sub>SO<sub>4</sub>

Using the gradient obtained from Figure 33 the quantum yield was calculated from the following equation:

$$Q = Q_{Ref} \left( \frac{Grad_{SiNP}}{Grad_{Ref}} \right) \left( \frac{\eta_{Toluene}^2}{\eta_{Ref}^2} \right) \quad (18)$$

Where  $Q_{Ref} = 54.6$ ,  $\eta_{Toluene} = 1.497$  and  $\eta_{Ref} = 1.346$ . A quantum yield of 10.6 % was calculated. . . . .  
Previously reported quantum yields for alkyl functionalised SiNPs typically lie between 4 % and 25 %<sup>73, 91, 195</sup>.

Interestingly, the differences in capping layer did not greatly affect the optical properties or the size of the SiNPs. Each sample shows an identical UV/Vis absorption peak at 280 nm and in each case the PL emission spectrum shows emission in the blue region at a wavelength of between 400 and 407 nm under excitation of 340 nm, Figure 5a). This shows there are no significant changes in optical properties between the differing lengths of the capping layers used. This is unsurprising due to the similar nature of the functionalisation.

### 3.5. Thermal Stability

The thermal stability of SiNPs was analysed by TGA. **Figure 34** shows the TGA curve and its first derivative for dodecyl functionalised SiNPs as they undergo heating from 50 to 550 °C with a heating rate of 20 °Cmin<sup>-1</sup> under a nitrogen atmosphere. For undecyl functionalised SiNPs produced via electrochemical etching/ hydrosilylation the onset of the mass drop occurs at approximately 200 °C. However for dodecyl functionalised SiNPs produced using the described solution reduction, the onset is at approximately 240 °C. The form is typical for a volatile melt with an ultimate mass loss of approximately 27%. This increase in desorption temperature may be due to the greater length of the hydrocarbon chain and/ or the higher surface coverage, both of which can stabilise the structure against evaporation due to the presence of a greater number of Van Der Waals attractions. The weight derivative of the TGA curve illustrates the transition temperature where the greatest mass loss occurs. The rest of the material decomposes between 270 and 550 °C. The peaks in the 300-350 °C range can be assigned to decomposition and desorption of Si-C from the passivating layer which is stable up to temperatures of 310 °C.<sup>196</sup> The intermediary peaks up to 550 °C may be indicative of the presence of potential sample impurities or by-products, or the removal of bound functional groups from the silicon surface.



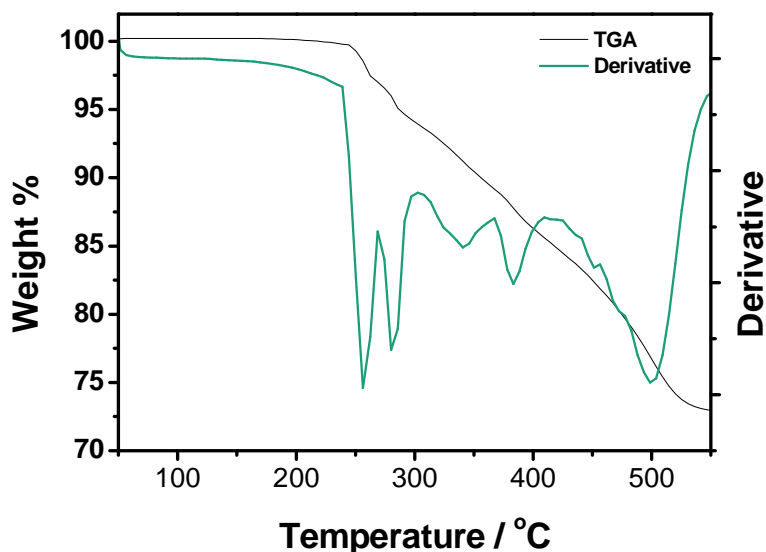


Figure 34: TGA and derivative of dodecyl functionalised SiNPs between 50 and 550 °C at a heating rate of 20 °Cmin<sup>-1</sup>

### 3.6. Summary

The successful one-pot synthesis of alkyl-functionalised SiNPs for four different ligands systems shows that this method is viable for a wide range of different functionalising agents (surfactants). This offers a wide range of potential functionalisations such as amine or allyl end groups. In this work the level of alkyl capping, despite initial appearances, is broadly consistent for all capping layers, although some experiments show a raised level of Si-O. This is because the quenching solvent used in this method reacts with the unfunctionalised Si-H on the surface of the particle. It has been shown that the SiNPs produced by this method are silicon rich, crystalline, luminescent, and functionalised with alkyl chains. Additionally these particles can be produced in higher yields and with higher surface coverage than those produce by other methods and as a result make them a more viable candidate for the mass production of functionalised SiNPs.



**Chapter 4:**  
Solution Synthesis of  
Phenylacetylene  
Functionalised SiNPs for  
Thermoelectric  
Applications.

## 4.1. Overview

As discussed there are a number of different approaches to silicon based thermoelectrics such as SiNWs and nanostructured bulk silicon.<sup>31, 106, 152, 153</sup> However these processes either require high temperature processing, are difficult to produce in bulk, or uses toxic reagents in their preparation. Solution approaches are a good way to produce low dimension silicon nanostructures, with the potential to scale up as well as offering an aspect of size control.<sup>89, 181</sup> One issue of avoiding high temperature processing to produce a bulk material is that the porous nature of the material makes it a poor electrical conductor which compromises the reduction in thermal conductivity.<sup>197</sup>

The attachment of a conductive or conjugated ligand has the potential to improve the electrical conductivity between particles.<sup>103</sup> In addition, organic molecules and polymers are generally poor thermal conductors so the attachment of such a ligand would not increase the thermal conductivity.<sup>134, 158</sup> Additionally, recent theoretical studies suggest that once optimised, a system made up of ligands/organics and quantum dots have great potential for use as thermoelectric materials.<sup>165</sup>

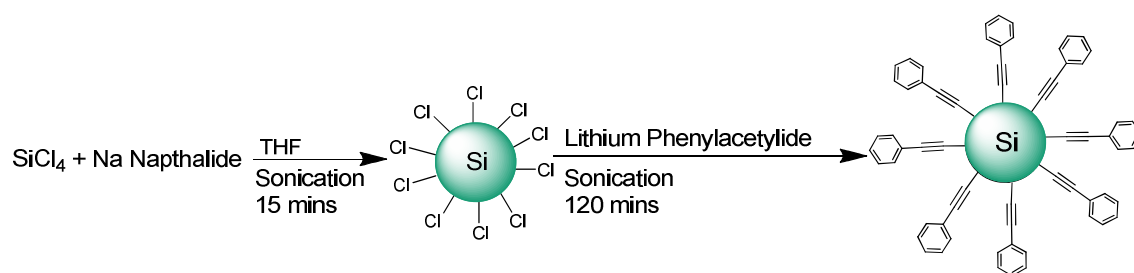
By attachment of conjugated molecules to the surface of silicon particles it has been observed that there is a flow of current to the chains from the SiNP surface<sup>198</sup> and it has also been observed that small conjugated molecules attached to the surface of silicon such as; phenylacetylene, can improve the efficiency of semiconductor-metal junctions.<sup>199</sup>

In the following study, phenylacetylene functionalised SiNPs were produced via a solution reduction method. Micelles of  $\text{SiCl}_4$  were reduced using sodium naphthalide to produce chlorine terminated SiNPs followed by the reaction of this surface with an organolithium reagent to functionalise them.<sup>87</sup> The resulting material was characterised using FTIR,  $^1\text{H-NMR}$ ,  $^{13}\text{C-NMR}$ , EDS, XPS and TEM. The thermal stability was studied using TGA and DSC.

Phenylacetylene functionalised SiNPs were pressed into a pellet and the electrical conductivity and Seebeck coefficient were measured at ambient temperature. The thermal conductivity was measured at 100 and 150°C. These measurements were then used to work out the figure of merit ZT to give a measure of thermoelectric performance. These were carried out to help identify the potential of SiNPs functionalised with conjugated molecules for thermoelectric applications and to determine if charge can be transported from particle to particle through conjugated organic molecules attached to the surface.

## 4.2. Synthesis of phenylacetylene Functionalised SiNPs

Using a method outlined by Baldwin et. al.<sup>87</sup> a dark brown suspension of chlorine terminated SiNPs was produced by reducing micelles of  $\text{SiCl}_4$  with a solution of sodium naphthalide. These particles were then functionalised using lithium phenylacetylide to give the desired surface functionalization. After washing and removal of residual naphthalene by heating under reduced pressure, approximately 500-750 mg of phenylacetylene functionalised SiNPs were obtained as an orange waxy solid. See reaction **Scheme 14**:



**Scheme 20: Synthesis of phenylacetylene functionalised SiNPs using a bottom up approach.**

## 4.3. Characterisation of Phenylacetylene Functionalised SiNPs

### 4.3.1. FTIR and NMR

The FTIR spectrum (**Figure 35**) shows peaks that are characteristic of phenylacetylene functionalised SiNPs. The spectrum shows peaks at  $3051\text{ cm}^{-1}$ , representative of aromatic C-H, and at  $1596$  and  $1487\text{ cm}^{-1}$  which are representative of aromatic C-C bonds. Also, a sharp peak is observed at  $2161\text{ cm}^{-1}$ , which is characteristic of the  $\text{C}\equiv\text{C}$  stretching mode. This, combined with the absence of a sharp peak at  $3300\text{ cm}^{-1}$ , which would correspond to alkyne C-H stretching, suggests that the terminal side of the alkyne is attached to silicon. This is also supported by the  $\text{Si-C}\equiv\text{C}$  peaks at  $1441$  and  $1221\text{ cm}^{-1}$ . The Si-O peak between  $1100$  and  $1000\text{ cm}^{-1}$  is observable but is broad and weak when compared with the sharp peaks at  $1068$  and  $1026\text{ cm}^{-1}$  which are characteristic of phenylacetylene.

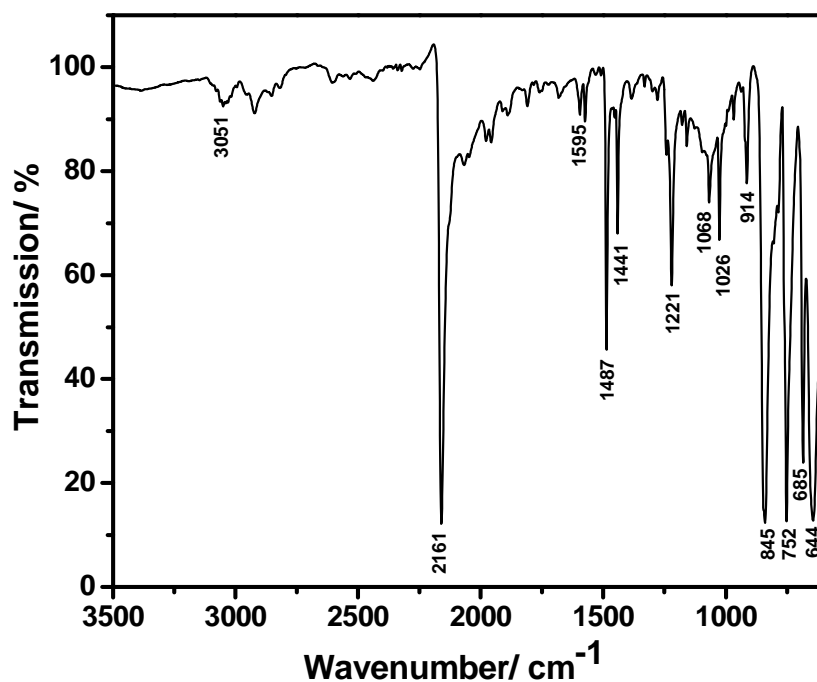
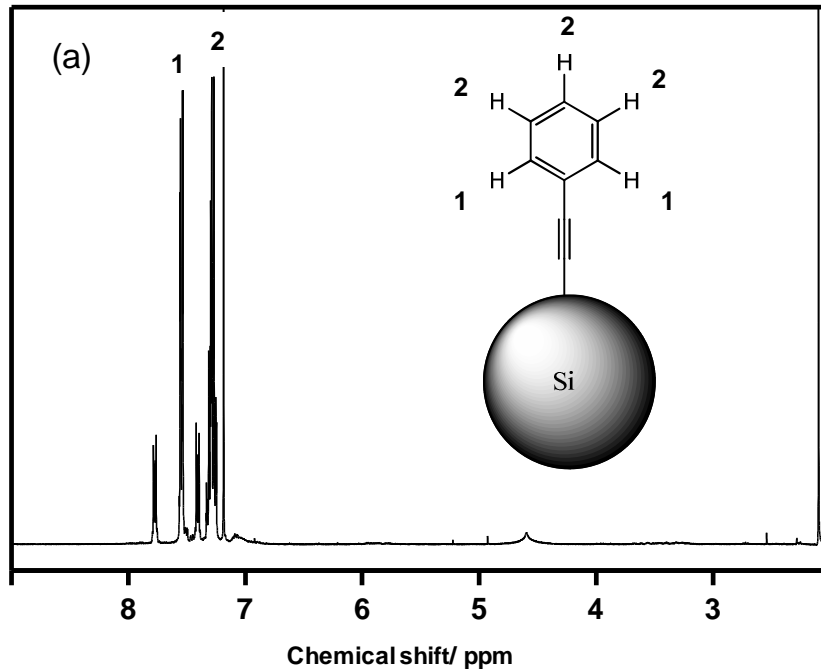


Figure 35: FTIR spectrum of phenylacetylene functionalised SiNPs

Further evidence of phenylacetylene functionalisation is given by the <sup>1</sup>H-NMR **Figure 36** and <sup>13</sup>C-NMR **Figure 37** spectra. <sup>1</sup>H-NMR shows two multiplet peaks at 7.53 and 7.30 ppm with an integration of 2:3 respectively, characteristic of the phenyl protons of phenylacetylene. Also, there was no presence of the peak expected for a terminal proton on the alkyne at 3 ppm. These features are evidence of the molecule being bound to the SiNPs.

The <sup>13</sup>C-NMR shows the four peaks for the phenyl carbons at 132, 129, 128 and 121 ppm and 2 peaks for the alkyne at 106 and 86 ppm, characteristic of the carbon closest to the phenyl and the silicon respectively. In both the <sup>1</sup>H-NMR and <sup>13</sup>C-NMR the peaks for residual naphthalene can be observed at 7.47, and 7.84 and at 127, 125, and 133 respectively.

Figure 36:  $^1\text{H}$ -NMR of phenylacetylene functionalised SiNPs.Figure 37:  $^{13}\text{C}$ -NMR of phenylacetylene functionalised SiNPs.

#### 4.3.2. Microscopy

The TEM micrograph shows that SiNPs have been synthesized (Figure 38). The SiNPs show a wide distribution of particle diameters from 2 to 10 nm (inset Figure 38). The mean diameter of the nanoparticles produced is 6 nm with a standard deviation of 1 nm, obtained from the

measurement of the diameter of 150 particles from different regions of the grid. The high standard deviation and wide size distribution can be explained by the lack of controlling influence on the micelle size, i.e. lack of use of surfactants.<sup>91</sup>

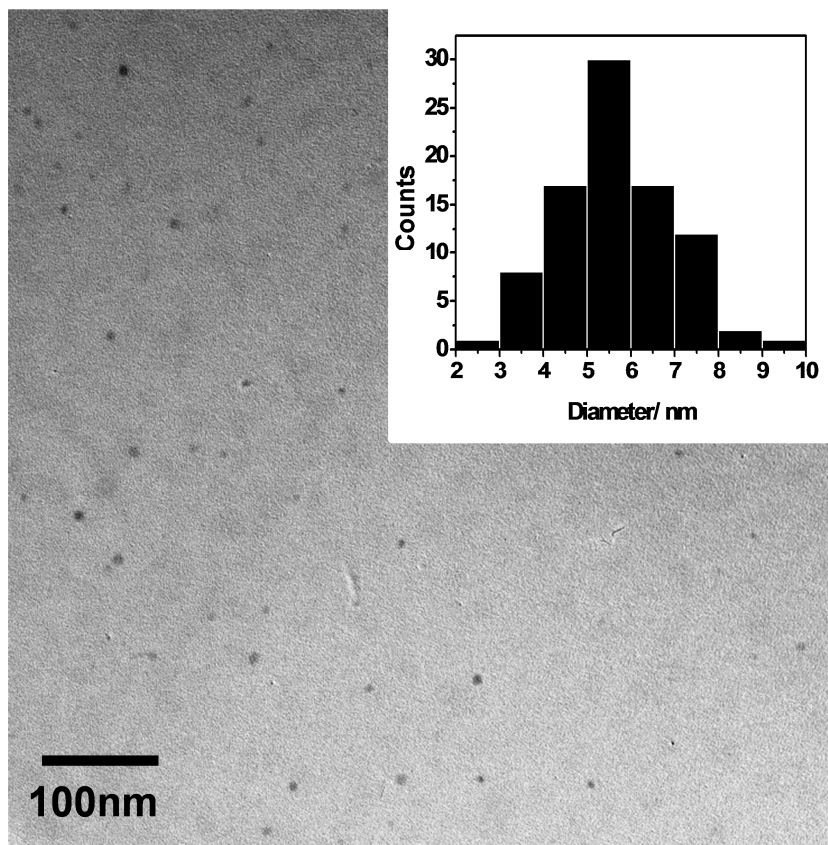
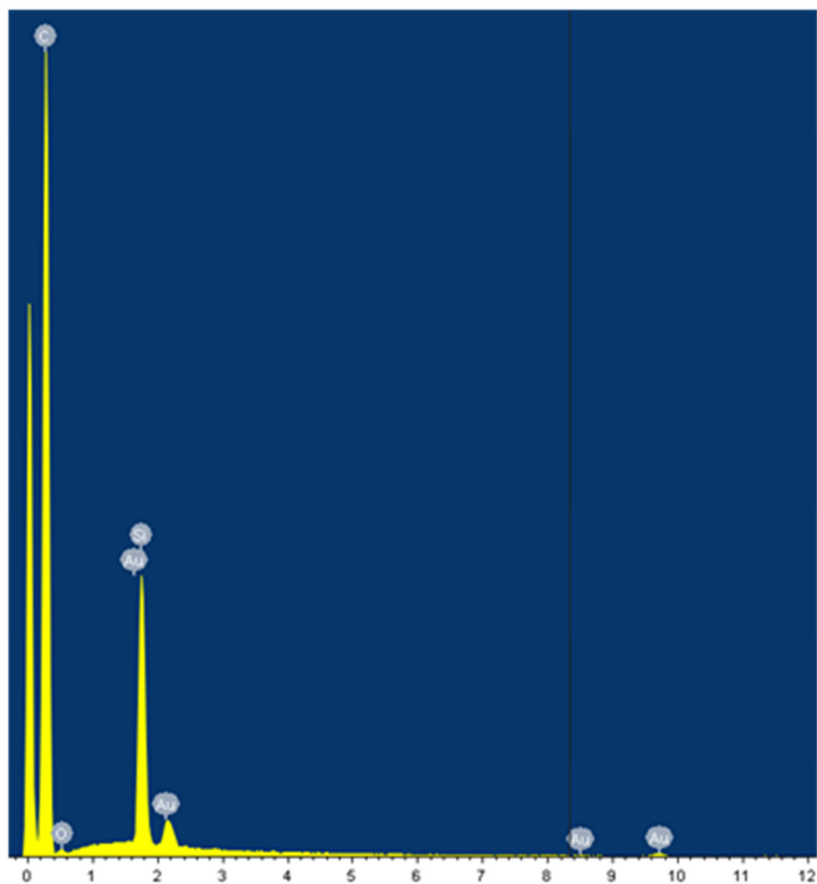


Figure 38: TEM image and size distribution of phenylacetylene functionalised SiNPs . Inset, size distribution of silicon nanoparticle.



### 4.3.3. EDX and XPS



**Figure 39: EDX of phenylacetylene functionalised SiNPs.**

The phenylacetylene functionalised SiNPs are rich in both silicon and carbon. This can be observed in the EDX spectrum obtained from a number of spots on the material. EDS shows the elemental components of the material to be silicon, carbon and oxygen (**Figure 39**).

This can also be observed from the XPS survey spectrum of the SiNPs (**Figure 40**). This spectrum shows an elemental composition ratio of Si:C:O of approximately 1:7:2.7. The level of oxygen observed in this material is considerably higher than expected, however lower levels of oxygen were observed on EDX (**Figure 39**). The increased oxygen level observed using XPS is typical of the X-ray induced oxidation of SiNPs as described in chapter 3.<sup>185, 200</sup> Additionally, XPS does not show any signals from elemental impurities of potential by-products such as sodium, lithium and chlorine. Individual fittings for the Si2p C1s and O1s give a better grasp on the elemental ratios of the material, however the silicon signal is lower than would be expected. This is likely to be due to the shallow penetration depth of the technique.

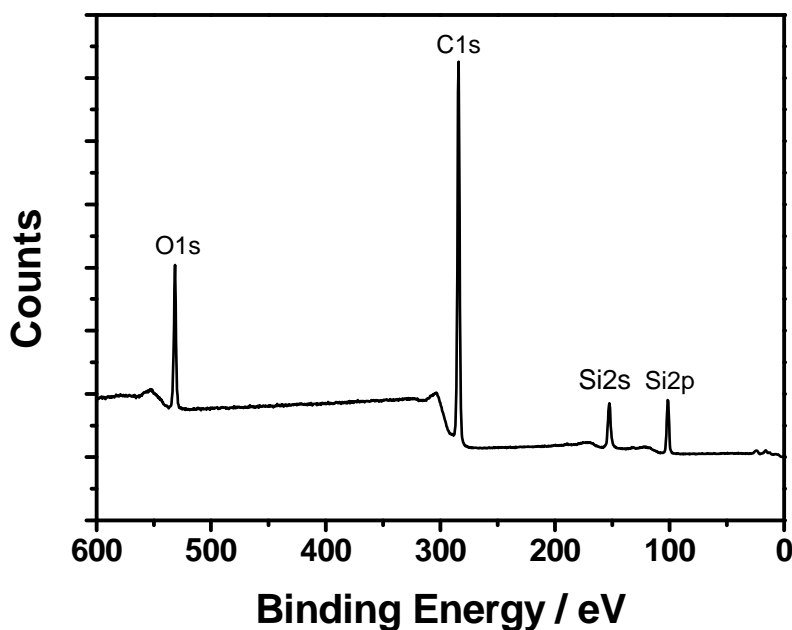


**Figure 40:** XPS survey spectrum for phenylacetylene functionalised SiNPs. Photoelectron spectrum was collected with incident photon energy of 1486.6 eV.

In **Figure 41**, the Si2p spectrum for phenylacetylene functionalised SiNPs is fitted with three components: at 99.9 eV, 101.5 eV, and 102.3 eV representing contributions from Si-Si, Si-C and Si-O respectively<sup>185, 186</sup>. The peak at 99.9 eV representing the Si-Si within the centre of the nanoparticles contributes 2 % of the total spectrum area within the fitted energy window. The remaining 98 % is from Si-C and Si-O at the particle surface. Of this remainder, 78 % is from Si-C and 20 % is from Si-O. This shows an estimated 79.5 % of the available surface has undergone functionalisation. This compares favourably with H-terminated Si(111) surfaces bound by organic monolayers where 50 % surface coverage is typically obtained<sup>111, 112</sup>.

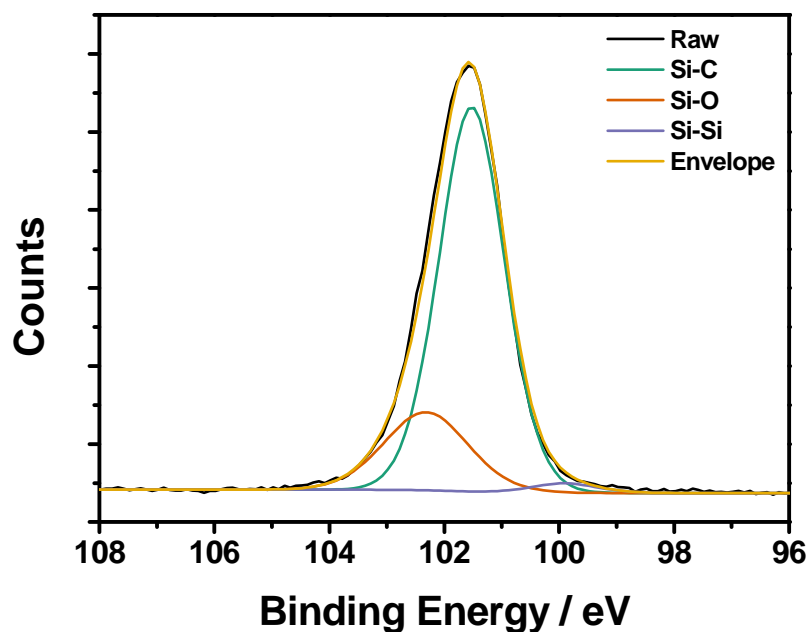


**Figure 41:** XPS spectra obtained for phenylacetylene functionalised SiNPs showing high resolution spectrum of Si<sub>2p</sub> region. Photoelectron spectrum was collected with incident photon energy of 1486.6 eV.

In **Figure 42**, the C<sub>1s</sub> spectrum for phenylacetylene functionalised SiNPs is fitted with three components: at 283.3 eV, 284.4 eV and 285.3 eV representing contributions from C-Si, C-C (aromatic) and C-C (aliphatic) respectively. 92 % of the spectrum area is from the peaks representing C-C within the carbon chains and the remaining 8 % is made up by the Si-C where the passivating layer is bound to the silicon centre. The ratio of the area of the spectrum represented by each component is close to 1:11.5, which is higher than the expected ratio of Si-C to C-C bonds in the phenylacetylene functionalised SiNPs. However some of this may be related to unbound carbon impurities such as naphthalene.

In **Figure 43**, the O<sub>1s</sub> spectrum for phenylacetylene functionalised SiNPs is fitted with one component at 531.8 eV, which makes up 100 % of the spectrum and represents Si-O.

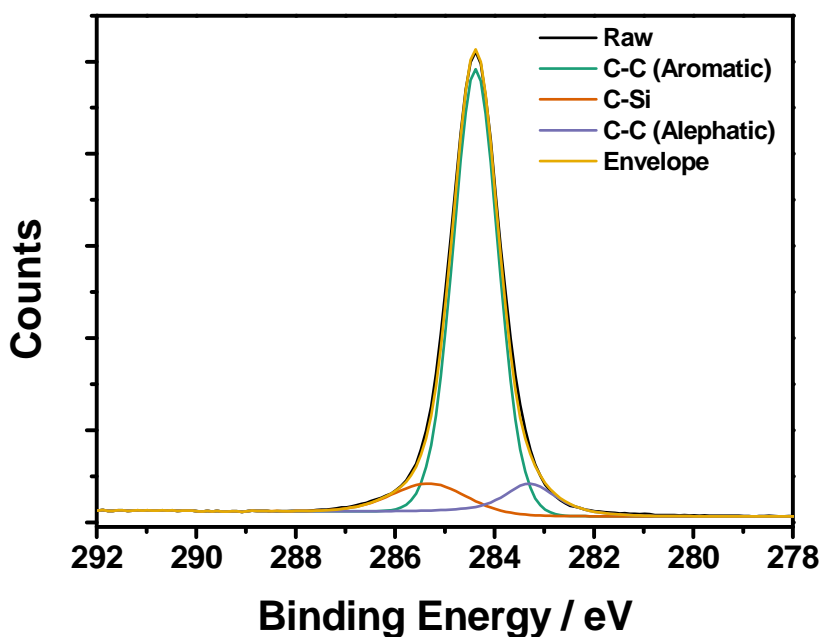


Figure 42: XPS spectra obtained for phenylacetylene functionalised SiNPs showing high resolution spectrum of C1s region. Photoelectron spectrum was collected with incident photon energy of 1486.6 eV.

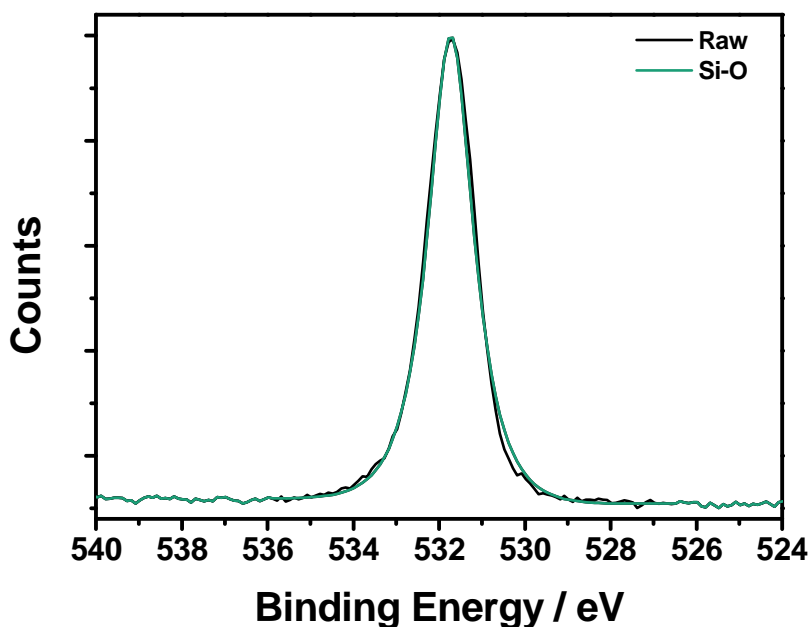
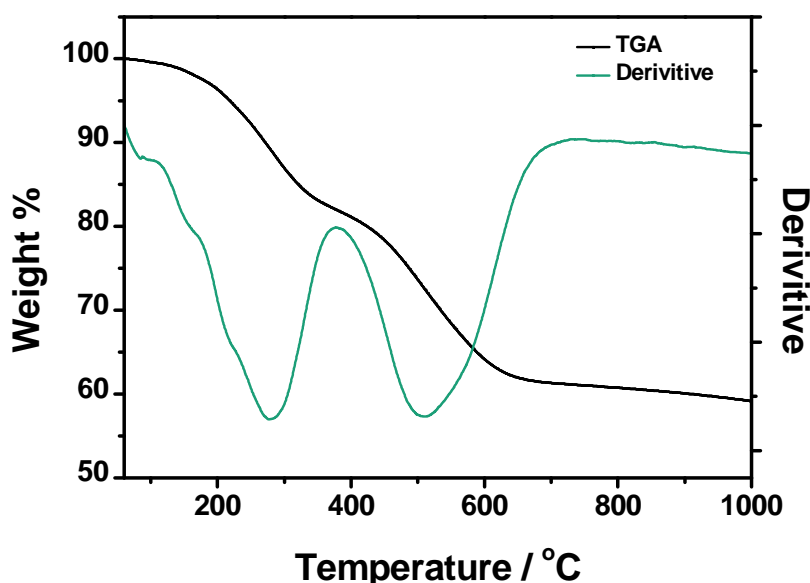


Figure 43: XPS spectra obtained for phenylacetylene functionalised SiNPs showing high resolution spectrum of O1s region. Photoelectron spectrum was collected with incident photon energy of 1486.6 eV.

#### 4.4. Thermal Stability

The DSC trace (**Figure 45**) begins at a flat level of heat flow before a negative peak can be observed at 165°C, representing a solid-liquid phase transition. Meanwhile, the weight on the TGA trace (**Figure 44**) remains close to 100 %. After this feature the heat flow into the sample begins to decrease relatively rapidly, which suggests that the sample is beginning to undergo degradation. In this region a minimum is observed in the derivative of the TGA, showing a higher rate of weight loss at this point. The DSC trace reaches a maximum at 320 °C showing completion of the initial degradation. After 330 °C the heat flow into the sample increases again, the TGA trace shows that the weight continues to decrease; becoming more rapid at approximately 500 °C, as depicted by another minimum on the derivative. This is likely to be due to continued degradation. This corresponds to a shoulder in the DSC. After 650 °C, little change in weight occurs on the TGA which suggests that degradation is complete, however a small peak in the DSC trace suggests that an exothermic process occurs. The overall percentage weight loss at 1000 °C is 40 %. Assuming that all remaining material is silicon as a result of heating in an inert atmosphere, the initial ligand to silicon ratio of the phenylacetylene functionalised SiNPs is 1 to 5. However this is a rough estimation of the coverage as it assumes all remaining material is solely silicon and all weight loss is as a result of degradation of ligands, which may also be related to other processes such as desorption of physisorbed ligands and the evaporation of functionalised SiNPs.<sup>85</sup> In this respect XPS offers a more accurate and complete estimation of surface coverage.



**Figure 44: TGA and derivative of phenylacetylene functionalised SiNPs**

The DSC and TGA traces are useful as they show at what temperature a material produced from phenylacetylene functionalised SiNPs can be processed, tested or used. The observation of a

solid to liquid phase transition at 175 °C suggests that the material could only be used up to approximately 150°C, before the melting process begins warping the material. Thus, the material would only be suitable for low temperature thermoelectric applications. Examples include: energy scavenging from hot water/cooling water outflow from a plant or thermal spring, or the conversion of heat from light harvesting.

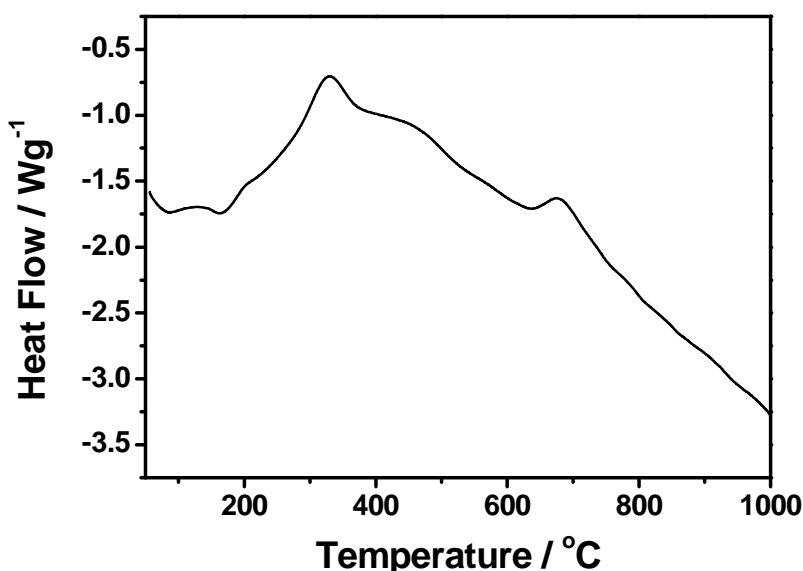


Figure 45: DSC of phenylacetylene functionalised SiNPs.

#### 4.5. Thermoelectric Measurements

The initial and aged thermoelectric measurements for a pellet made up of phenylacetylene functionalised SiNPs are given in **Table 2**. The measurements obtained at ambient temperature show that the material produced has an exceptionally high Seebeck coefficient and a low thermal conductivity. These two values offset the low electrical conductivity in the equation for the figure of merit (ZT). The ZT of approximately 0.6 at ambient temperature is comparable to many better established materials. However after 1 month this value has reduced by an order of magnitude, which points toward significant stability issues. Closer inspection of the individual components within the calculation for ZT reveals that there is clearly room for further reduction in the electrical resistivity. This could be achieved by optimising the doping of the system although in this system there are two components that must be considered, the ligand and the SiNP.

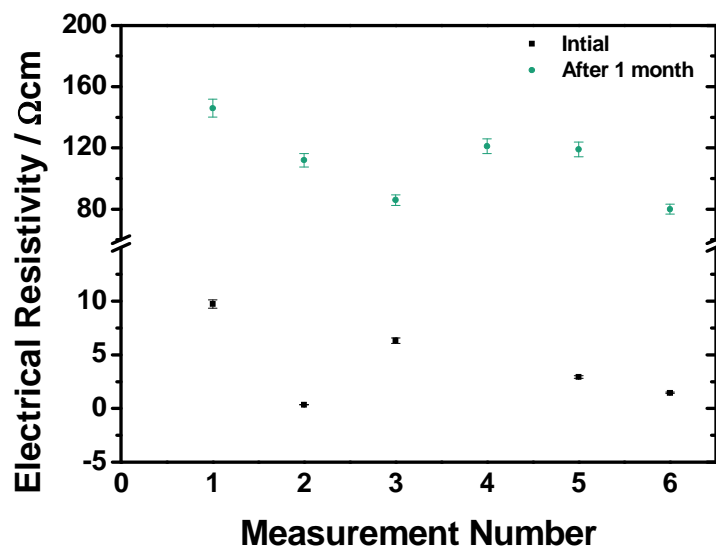
**Table 2: Thermoelectric measurements of a pellet of phenylacetylene functionalised SiNPs at room temperature.**

Age of Pellet	$\rho$ [kg m <sup>-3</sup> ]	$\sigma$ [S m <sup>-1</sup> ]	$S$ [ $\mu$ V K <sup>-1</sup> ]	$\kappa$ [W m <sup>-1</sup> K <sup>-1</sup> ]	ZT
Initial	1022	18.1	3228.8	0.1	0.6
1 month	1022	0.85	-1765	0.1	0.03

#### 4.4.1. Electrical Resistivity

The electrical resistivity of this material as given in table 1 is an average of 6 measurements at different points on the pellet. These points are plotted in **Figure 46**. Relative to other silicon materials of similar porosity, the electrical conductivity of a pellet of phenylacetylene SiNPs is significantly large.<sup>31, 201, 202</sup> However, when compared with materials typically involved in thermoelectric applications, the electrical conductivity is not high enough.<sup>132, 151</sup> This conductivity could however be optimized through the doping of the SiNPs or the doping of the ligands in order to increase the charge carrier concentration.

Measurements taken 1 month later (**Figure 46**) show an increase in the electrical resistivity by an order of magnitude. Suggesting that stability of the material is another weakness that would need to be addressed in order to make it a suitable material for thermoelectric applications.

**Figure 46: Electrical conductivity measurements of a pellet of phenylacetylene functionalised SiNPs at room temperature initial and after a month.**

#### 4.4.2. Seebeck Coefficient

The Seebeck coefficient of this material as given in table 1 is an average of 4 measurements at different points on the pellet. Each of these are plotted in **Figure 47**. The magnitude of the Seebeck coefficient is much higher than that documented for other silicon based materials.<sup>106, 152</sup> This can be attributed to the low carrier concentration and high resistivity, as discussed previously. If the charge carrier concentration is optimised, the Seebeck coefficient would be expected to become reduced by a factor of 10 to 100, based on previous work regarding silicon based materials.<sup>106, 152</sup> Optimization of doping would result in a compromise between the magnitude of the electrical conductivity and the Seebeck coefficient, which in practical terms would make for a more useful material but may alter the ZT positively or negatively.

In addition to this, individual measurements greatly fluctuate in value between different points on the pellet (**Figure 47**). This fluctuation suggests a high level of inhomogeneity in the sample as a result of it being made up of more than one component.

After 1 month there was no significant change observed in the magnitude of the Seebeck coefficient, however a change in sign was observed. This result is unexpected for a number of reasons. Firstly, with the greatly increased electrical resistivity it would be expected that an increase in the magnitude of the Seebeck coefficient would be observed. Secondly, the change in sign would typically be representative of doping, p or n type. However this has not been actively pursued. A reason for these two observations may lie in the inhomogeneity of the sample, as suggested by the observed variation in the measured Seebeck coefficient values.

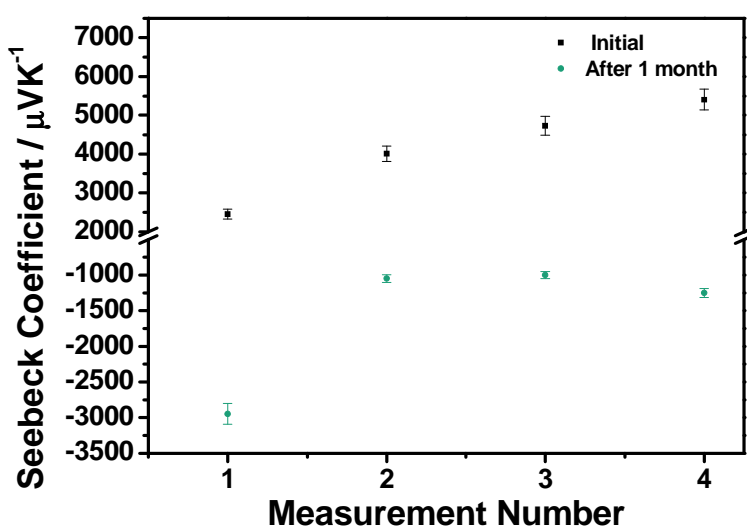


**Figure 47: Seebeck coefficient measurements of a pellet of phenylacetylene functionalised SiNPs at room temperature initial and after a month.**



### 4.4.3. Thermal Conductivity

The thermal conductivity was measured at 373 K and 423 K, and the values were 0.15 and 0.19 W m<sup>-1</sup> K<sup>-1</sup> respectively. The listed value in **Table 2** is an extrapolated value expressed to one decimal place. This gives an ambient temperature ZT of 0.6. This value is comparative to other materials under investigation in thermoelectrics.<sup>144, 145</sup>

The low thermal conductivity values may be in part due to the low density. As the samples were simply cold pressed, the density might be well below the theoretical (crystallographic) value. The effect of densification on thermal conductivity ( $\kappa$ ) is of the form below.<sup>203, 204</sup>

$$\frac{\kappa_{porous}}{\kappa_{dense}} = 1 - \frac{4}{3}\phi \quad (19)$$

where  $\phi$  is the porosity and is defined as

$$\phi = 1 - \frac{\rho_{porous}}{\rho_{dense}} \quad (20)$$

Where  $\rho_{porous}$  is the density of the sample and  $\rho_{dense}$  is the theoretical density of the dense material

Unfortunately, given the presence of the organic capping agents, the calculation of the theoretical density is difficult. If the organic component is neglected, then the density is expected to be that of silicon, which is 2329 kg m<sup>-3</sup>. The measured density is approximately 1022 kg m<sup>-3</sup>. This suggests, compared to pure silicon, the sample is approximately 44% dense. Of course this is a gross approximation as it ignores the organic component completely, but it does suggest that the sample is quite porous and that  $\kappa$  is well below that of the dense material.

## 4.6. Summary

Phenylacetylene functionalised SiNPs have been successfully synthesised using a solution reduction method to produce chlorine terminated SiNPS and an organometallic for surface functionalization. This opens up the potential for a number of other conjugated ligands such as oligothiophenes.

Although the material after the processing is not suitable for use in a device in its current state as a result of its thermal stability and high resistivity, some key advancements have been made. Firstly the ability to produce a pellet which shows higher conductivity than purely silicon materials of comparable porosity is an encouraging sign. This has been achieved without any control of charge carriers which would allow further optimisation of the system. Additionally the thermal

conductivity has been reduced to a level comparable with organic materials. Both of these are useful developments.

Further to the work performed here it is important to find a way in which control of the charge carriers can be achieved. However this material has two components, an organic and an inorganic component. To understand this system it is important that we understand exactly how the doping of each of these components affects the thermoelectric properties of organic-SiNP nanocomposite materials.

# Chapter 5:

Effects of Ligand Doping  
on the Thermoelectric  
Properties of  
Terthiophene  
Functionalised Silicon  
Nanoparticles

## 5.1. Overview

Chapter 4 shows that the use of a suitable ligand could aid the thermoelectric performance of silicon materials processed at much lower temperatures and open them up to similar processing techniques to polymers e.g. inkjet printing. Phenylacetylene functionalised SiNPs synthesised by a bottom up method, gave a ZT at ambient temperature of 0.57 for a cold pressed pellet. The main reason for this was its very low thermal conductivity, comparable to that of some polymers. This is to be expected due to its organic characteristics. However, the material's major downfall was that, although the electrical conductivity was high compared to materials of similar porosity, it was too low to be suitable in electronic devices. This can be attributed to the low concentration of charge carriers.

The doping of ligands can be considered to be similar to that of polymers. An oxidant is used to remove electrons from the organic molecules to form a hole in the material allowing it to carry charge. Polythiophene based polymers are very common commercial conductive polymers e.g. PEDOT and have also been used widely in the development of organic thermoelectrics.<sup>156, 163</sup> The doping approaches with such polymers are very well documented.<sup>205-209</sup> Moreover oligothiophenes can be easily attached to silicon surfaces in a similar way to phenylacetylene and the longer chain results in a better potential for chain overlap.<sup>171</sup>

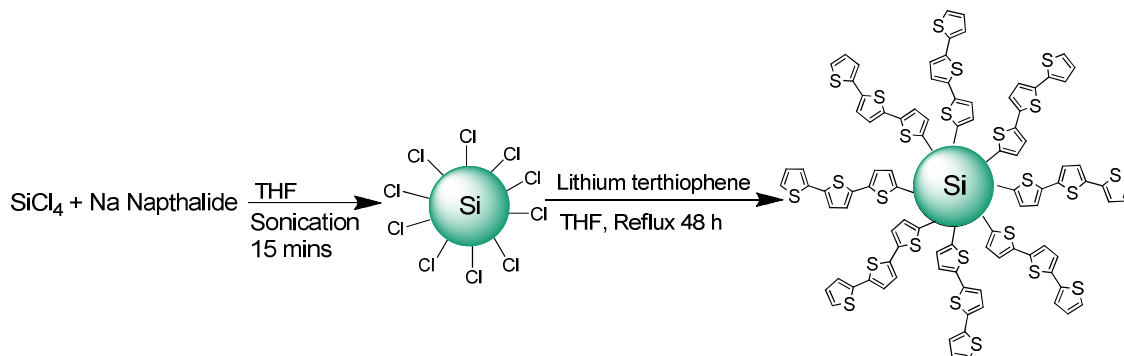
In this study terthiophene functionalised SiNPs have been synthesised via the micelle reduction method (described in chapter 4) and characterised using FTIR, TEM, EDX and XPS. Additionally the thermal stability of the undoped material was analysed using TGA and DSC.

The terthiophene units on the surface of these particles have then been doped using different mass ratios of  $\text{NOBF}_4$  as an oxidant (+1.00 V vs.  $\text{Cp}_2\text{Fe}^{0/+}$ ).<sup>210</sup> After oxidation the elemental composition was investigated using EDX and XPS to indicate the presence of the counter ion  $\text{BF}_4^-$ . Cold pressed pellets of the resulting materials were produced and electrical resistivity, Seebeck coefficient and thermal conductivity were measured at room temperature to investigate the effects of the level of doping of the ligand on the thermoelectric properties of these materials. Additionally the stability of the electrical resistivity was monitored over one month.

## 5.2. Synthesis of Terthiophene Functionalised SiNPs

Using a method outlined in Chapter 4, a dark brown suspension of chlorine terminated SiNPs was produced by reducing an emulsion of micelles of  $\text{SiCl}_4$  with a solution of sodium naphthalide. These particles were then heated to reflux in THF for 48 hr with lithium terthiophene to give the desired surface functionalization. This procedure was based on a procedure described by He *et al.*<sup>171</sup> for functionalising silicon surfaces with thiophene oligomers. After washing and removal of

residual naphthalene by heating under reduced pressure, approximately 500 mg of product was obtained as a yellow/green solid.



**Scheme 21: Synthesis of terthiophene functionalised SiNPs using a bottom up approach.**

### 5.3. Characterisation of Undoped Terthiophene Functionalised SiNPs

FTIR gives evidence of successful capping of SiNPs with terthiophene. FTIR (**Figure 48**) shows a peak at  $3065\text{ cm}^{-1}$  which is characteristic of aromatic C-H stretching as well as peaks at  $1490$  and  $1420\text{ cm}^{-1}$  which are characteristic of aromatic C=C stretching. The peak at  $1490\text{ cm}^{-1}$  is characteristic of the asymmetric stretch of C=C in thiophene oligomers. A peak representing Si-C can also be observed at  $1203\text{ cm}^{-1}$ . Peaks at  $829$ ,  $791$  and  $687\text{ cm}^{-1}$  are characteristic of the CH deformation with the most intense peak at  $791$  being characteristic of a 2, 5-substituted thiophene. Despite of evidence of successful capping of the surface with terthiophene there was still a high level of Si-O on the surface as indicated by the strong broad peak between  $1100$  and  $1000\text{ cm}^{-1}$ . This indicates a moderately low surface coverage, suggesting that further optimisation of the surface coverage may be possible. However increasing the reaction temperature and time had little effect on the intensity of this peak which suggests that the low surface coverage may be related to the steric bulk of the terthiophene.

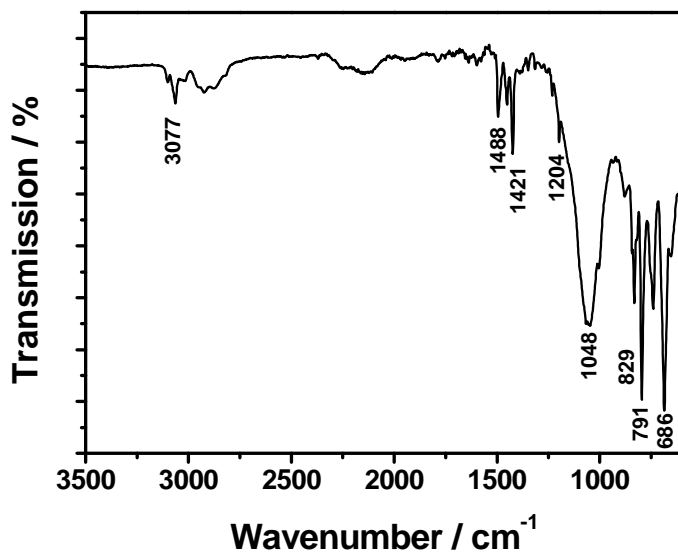


Figure 48: FTIR of Terthiophene functionalised SiNPs.

TEM micrographs (Figure 49) of the freshly prepared silicon quantum dots show particles ranging from 2 to 10 nm and an average particle size of 5.6 nm, with a standard deviation of 1.25 nm obtained from the measurement of the diameter of 150 particles from different regions of the grid. The sample was not very monodisperse, however this is to be expected as no surfactant was introduced to control the particle size distribution.

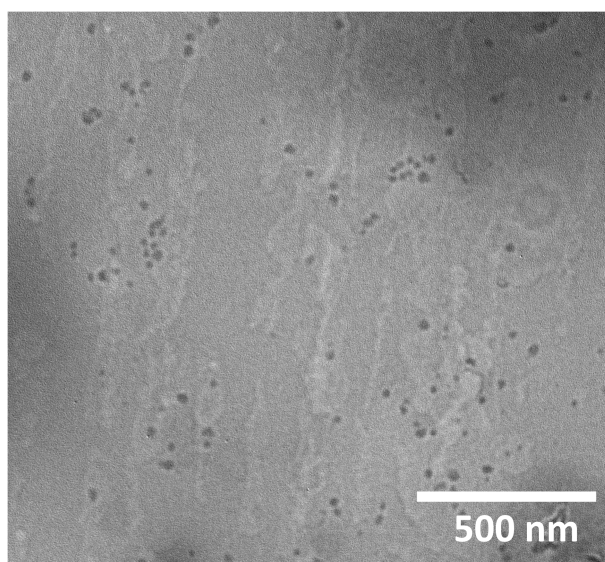


Figure 49: TEM micrograph of terthiophene functionalised SiNPs

The EDX (Figure 50) spectrum for the undoped product shows the presence of silicon, oxygen, carbon and sulphur as would be expected for terthiophene functionalised SiNPs indicating a favourable elemental composition. This is also supported by the XPS survey spectrum (Figure 501)

as peaks for Si2p and Si2s, C1s, O1s, and S2p and S2s can be observed, indicating the presence of the expected elements at the surface of terthiophene functionalised SiNPs.

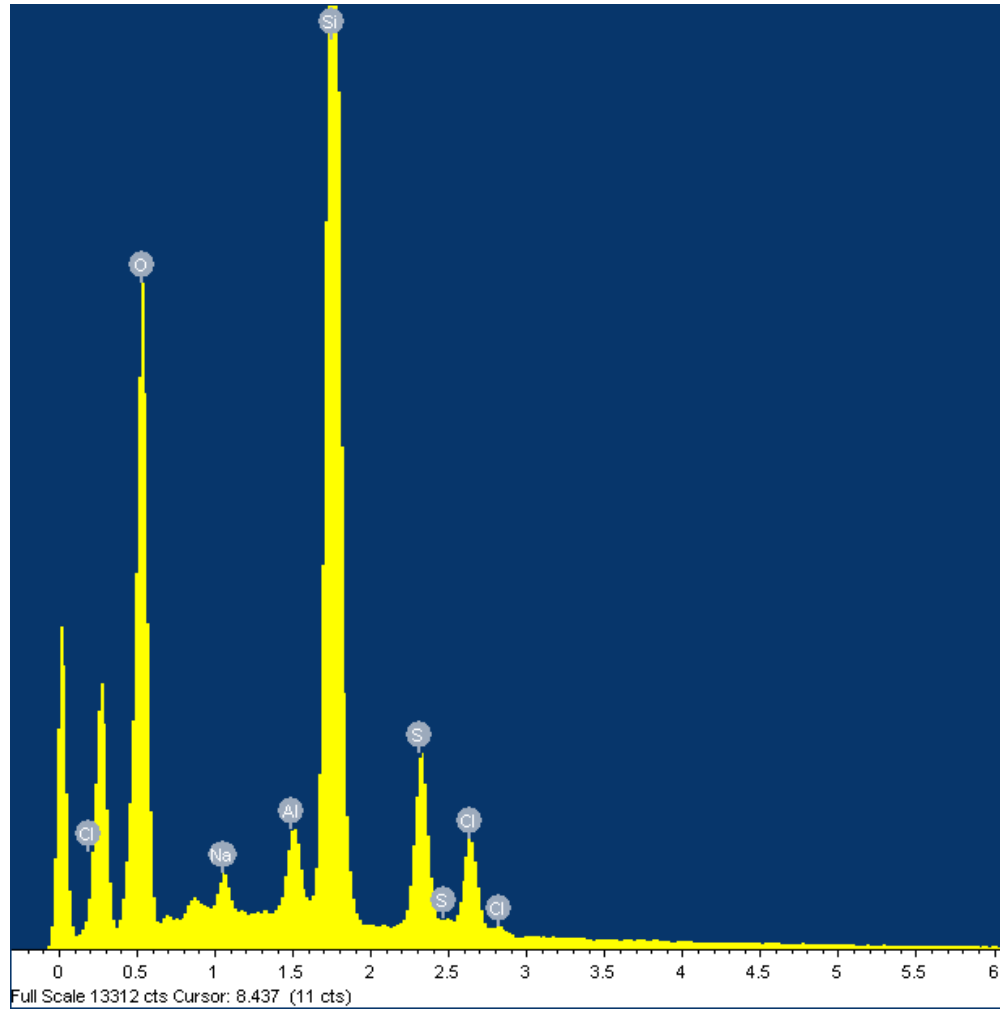


Figure 50: EDX spectrum of undoped terthiophene functionalised SiNPs

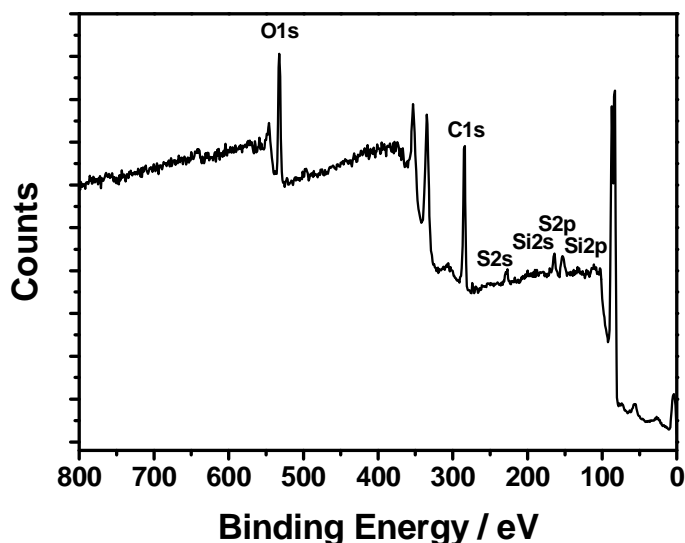
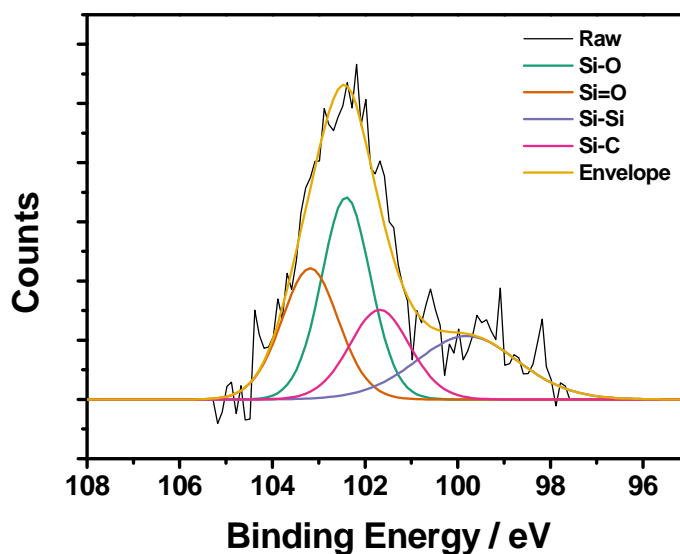


Figure 51: XPS survey spectrum obtained from undoped terthiophene functionalised SiNPs.

Photoelectron spectrum was collected with incident photon energy of 1486.6 eV.

In **Figure 52** the high resolution XPS for Si2p can be fitted to 4 components at 99.7, 101.4, 102.53 and 103.59 eV representing contributions from Si-Si, Si-C, Si-O and SiO<sub>2</sub> respectively. The peak at 99.92 eV representing the Si-Si bonding within the centre of the nanoparticles contributes 22.1 % of the total spectrum area within the fitted energy window. The remaining 77.9 % is from Si-C, Si-O and SiO<sub>2</sub> at the particle surface, 18.7 % is from Si-C and the remainder 59.4 % is from Si-O and SiO<sub>2</sub> combined. An estimated 23.5 % of the available surface has undergone capping. This is low when compared with hydrogen terminated Si (111) surfaces bound by organic monolayers using hydrosilylation, where 50 % surface coverage is typical.<sup>111, 112</sup>





**Figure 52:** High resolution XPS spectrum obtained from undoped terthiophene functionalised SiNPs showing Si2p region. Photoelectron spectrum was collected with incident photon energy of 1486.6 eV.

In **Figure 53** the C1s spectrum for terthiophene SiNPs is fitted with three components at 283.44 eV, 284.40 eV and 285.38 eV representing C-C, C-Si, and C-S respectively. 61.3 % of the spectrum area is from C-C and 32.9 % is from C-S within the ligand and the remaining 5.8% is made up by the C-Si where the passivating layer is bound to the silicon centre. The ratio of the area of the spectrum represented by each component is close to 1:5.7:10.7, which is close to the ratio of Si-C to C-C to C-S carbons in functionalised SiNPs (1:6:11).

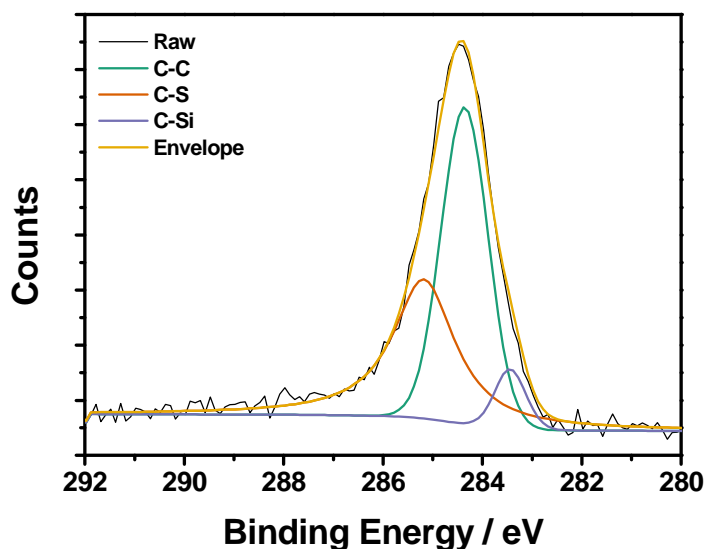


**Figure 53:** High resolution XPS spectrum obtained from undoped terthiophene functionalised SiNPs showing C1s region. Photoelectron spectrum was collected with incident photon energy of 1486.6 eV.

#### 5.4. Thermal Stability

The TGA and DSC shows an initial degradation temperature of the ligands at approximately 325 °C shown as a steep decrease in weight % on the TGA paired with a peak at 325 °C. This indicates the maximum operation temperature of this material is 300 °C and this would also be the maximum temperature in which they can be processed. After this initial degradation there is a secondary degradation at approximately 500 °C. This is observed by a second step decrease in weight % on the TGA which is again accompanied by a positive peak on the DSC.

In addition to this the surface coverage of the particles can also be estimated from the TGA. The initial weight drop is related to naphthalene in the sample. Assuming that all the reduction in mass is related to the decomposition of the surface ligands the percentage mass of ligand to silicon can be estimated. The percentage mass of ligand in the sample is approximately 65%, giving a molar ratio of ligand to silicon of 1 molecule to 5 silicon atoms. However this is a rough estimation of the coverage as it assumes all remaining material is solely silicon and all weight loss is as a result of degradation of ligands, which may also be related to other processes such as desorption of physisorbed ligands, loss of organic impurities and the evaporation of functionalised SiNPs.<sup>85</sup> XPS offers a more accurate and complete estimation of surface coverage.

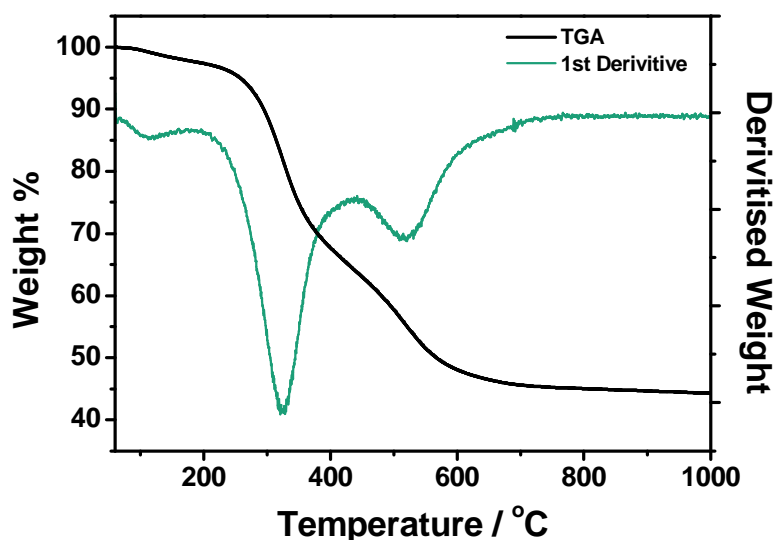


Figure 54: TGA curve and first derivative for terthiophene functionalised SiNPs

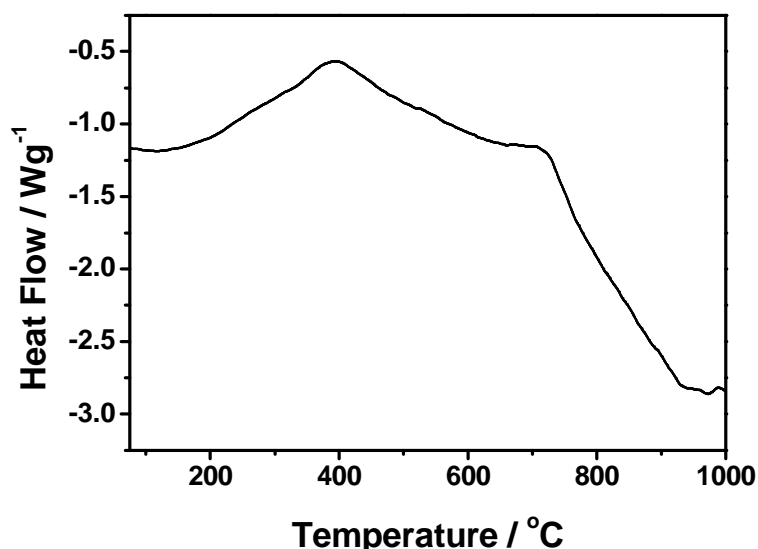


Figure 55: DSC curve of terthiophene functionalised SiNPs

### 5.5. Doping of Terthiophene Functionalised SiNPs

Terthiophene functionalised SiNPs were doped using the chemical oxidant  $\text{NOBF}_4$  which is commonly used as a dopant for polythiophene-based polymers.<sup>211-213</sup> Different  $\text{NOBF}_4$  to SiNPs particle mass ratios were used in dichloromethane. During the reaction effervescence of NO gas was observed and a colour change from yellow to dark green blue.

Once the oxidising agent was introduced a fluorine signal appeared in addition to the signals observed in the undoped sample observed in EDX (**Figure 56**). This is due to the  $\text{BF}_4^-$  counter ion

which stabilises the radical cation species formed. This can clearly be observed on the spectrum for doped terthiophene functionalised SiNPs with a terthiophene functionalised SiNPs/ $\text{NOBF}_4$  mass ratio of 0.5 (**Figure 56**). Additionally, the nitrogen of the  $\text{NO}^+$  cannot be observed suggesting that all the oxidising agent had reacted to form  $\text{NO}$  gas.

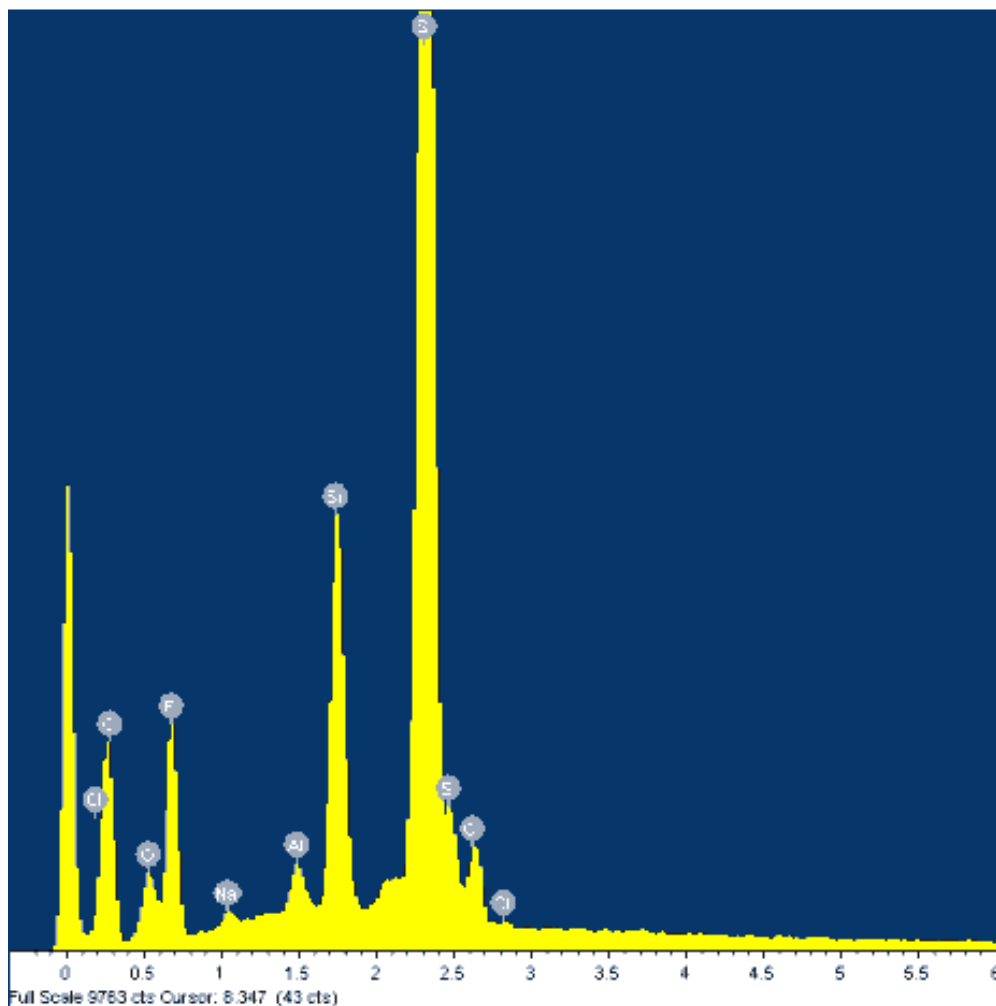


**Figure 56: EDX spectrum of doped terthiophene functionalised SiNPs**

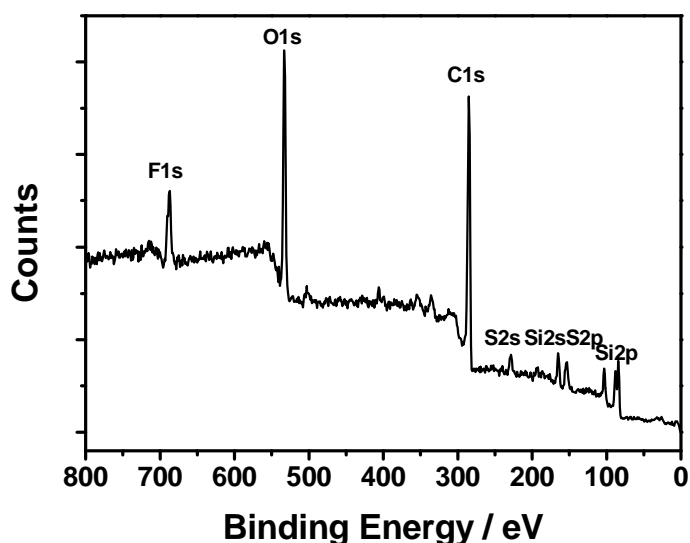


**Figure 57: XPS survey spectrum obtained from doped terthiophene functionalised SiNPs showing Survey spectrum. Photoelectron spectrum was collected with incident photon energy of 1486.6 eV.**

The observations made using EDX are also visible in the XPS survey spectrum, where the O1s, F1s, C1s, S2p and S2s, and Si2p and Si2s can be observed. As in the EDX the boron peak cannot be seen but the fluorine is clear and is evidence of the presence of the counter ion. As in the EDX spectrum an N1s peak is not observed, offering further evidence of full reaction of the reducing agent.

## 5.6. Thermoelectric Measurements

### 5.6.1. Electrical Conductivity

The effects of the doping ratio on the electrical resistivity can be observed in **Figure 58**. On doping of the ligands with  $\text{NOBF}_4$ , a sharp initial decrease in electrical resistivity can be observed between a ratio of 0 and 0.4 after this point the improvements in conductivity begin to plateau as all oxidisable sites are oxidised. The electrical resistivity at high levels of doping show small increases as unreacted oxidant is incorporated in the material with no additional charge carriers being introduced. Similar behaviour to this can be observed in the preparation of conductive polymers such as polythiophene or polyaniline.<sup>214</sup>

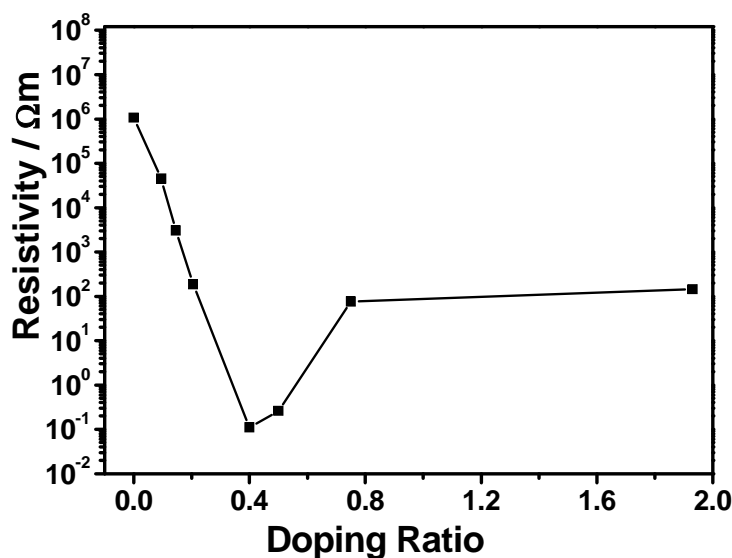


Figure 58 : Electrical resistivity against doping ratio (Mass Terthiophene functionalised SiNPs/Mass NOBF4)

The electrical resistivity obtained from these materials is much too high to incorporate in to a thermoelectric device. This would need to be decreased by at least a factor of  $10^2$ . However these results do demonstrate how the introduction of charge carriers on the surface ligands can enhance the electrical conductivity, in this case by 7 orders of magnitude over the undoped form.

There are a number of factors that could be adding to the high electrical resistivity. These include the high levels of surface oxide, low density and low surface coverage, in addition to the ligand particle system not being optimised. The ligand particle system could be altered by changing the ligand used or using a different dopant.<sup>180</sup>

### 5.6.2. Aging of Electrical Conductivity

Despite the relatively high resistivity of the materials produced, aging studies on the pellets with doping ratios of 0.4 and 0.5 show relatively good stability with the resistivity doubling after 1 week and then remaining relatively constant for up to 4 weeks. The initial rise could be related to evaporation of residual solvent. However this is a good indication of the stability of the doped ligands and how effective the counter ions are at stabilising the radical cations formed. This is a much better stability than that shown by phenylacetylene functionalised SiNPs processed under the same conditions. If this same stability can be translated into a better performing nanocomposite, this could lead to a significant move forward in silicon-organic nanocomposite thermoelectric materials. However, better stability could possibly be achieved using different counter ions.<sup>97, 215</sup> This was highlighted by Bubnova *et. al.* who achieved very stable conductive PEDOT using tosylate as the counter ion for the doped polymer.<sup>153</sup> This counter ion is much larger than  $\text{BF}_4$  and as a result stabilise the counter cation better.<sup>216</sup> Another example of this is the use

of the polymeric counter ion system PSS which forms a conductive co polymer when suitably doped.<sup>123</sup>

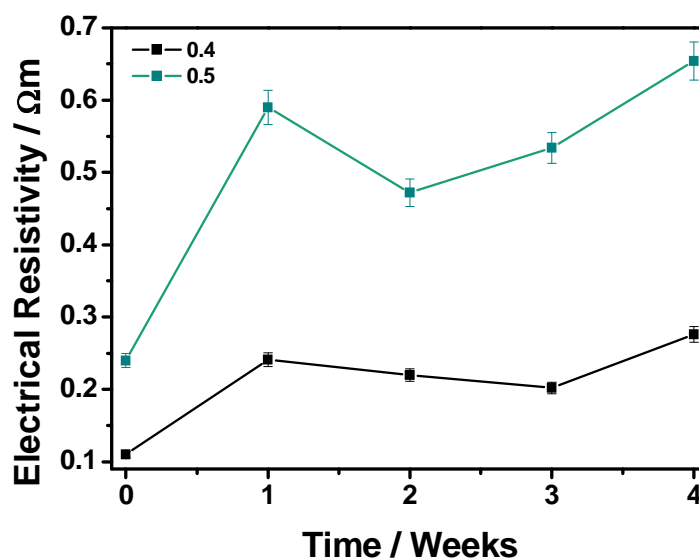


Figure 59: Electrical resistivity against time for the doping ratio of 0.4 and 0.5.

### 5.6.3. Seebeck Coefficient and Power factor

The measurement of the Seebeck coefficient gives a value more than one order of magnitude larger than other silicon based materials. This is in part due to the relatively high resistivity discussed earlier. In addition, this value is an order of magnitude higher than that measured for polythiophene at a comparable resistivity, suggesting that there may be an influence on the Seebeck coefficient as a result of the attachment of terthiophene to SiNPs.<sup>158, 217</sup> This is comparable with nanocomposites such as polythiophene-silver nanocomposites.<sup>218</sup> It is also worth noting that this could be related to the inhomogeneity of the material. In materials of this nature there are 2 components. This makes understanding the Seebeck coefficient obtained more difficult. This inhomogeneity was highlighted when comparing the fluctuation in Seebeck coefficient measurements from different parts of the pellet.

Table 3: Seebeck coefficient measurements at different points on pellet

Position	Edge	Near Edge	Near Middle	Middle
Seebeck Coefficient / $\mu\text{VK}^{-1}$	-4238	5822	-46851	-6439

The homogeneity may also be an explanation for the unexpected sign of the material. As the material is n-doped it would be expected that the Seebeck coefficient would be positive however

it is negative. From the measurements above it is clear to see that the sign of the Seebeck coefficient changes at random depending on measurement position.

Using the measurements taken at the edges for each pellet the Seebeck coefficient decreases as the doping ratio increases and as a doping ratio of 0.4 is reached a drop in Seebeck coefficient is observed. This is to be expected as a result of the relationship between the electrical resistivity and the Seebeck coefficient. Increases and decreases in electrical resistivity are generally mirrored in the measurement of the Seebeck coefficient. However in these results a change in sign and a large increase in the magnitude are observed for the Seebeck coefficient for the pellet with a doping ratio of 0.5. Once again this may be as a result of inhomogeneity. When the power factor is calculated from these values we see an increase with increasing levels of dopant addition. The power factors obtained are fairly high for an organic containing material and comparable to a number of polymeric thermoelectric materials studies such as emeraldine.<sup>219, 123, 153, 220</sup>

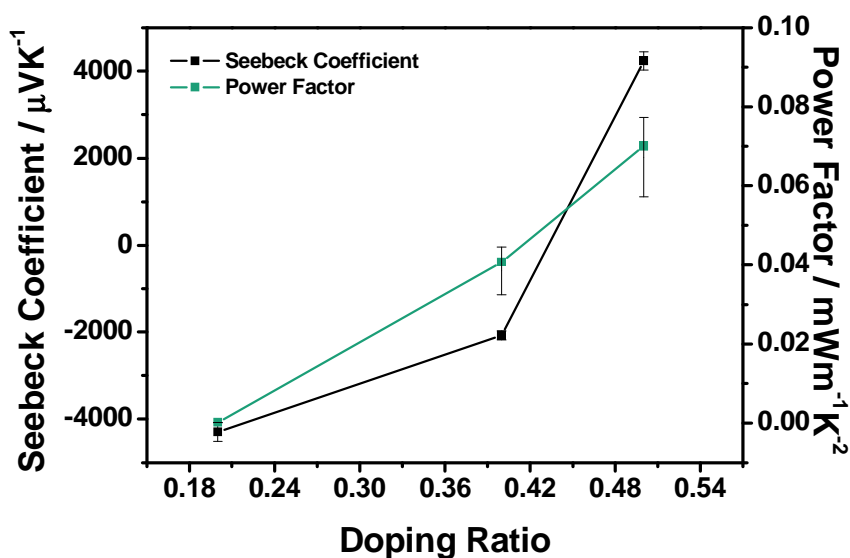
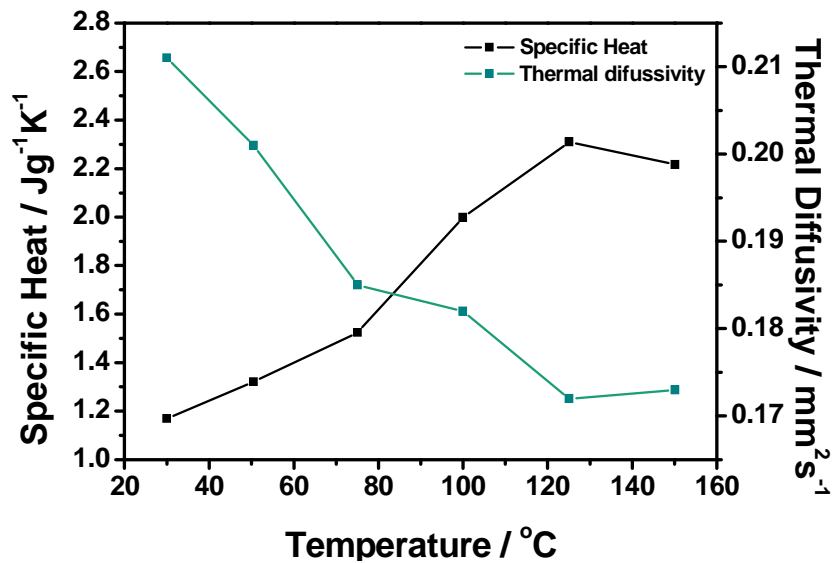


Figure 60: Seebeck coefficient and power factor against doping ratio (Mass Terthiophene functionalised SiNPs/Mass NOBF4)

#### 5.6.4. Thermal Conductivity

The thermal conductivity of a pellet of doped thiophene functionalised SiNPs shows a linear increase between 30 and 75 °C then increases rapidly between 75 and 100 °C before the increase in thermal conductivity plateaus as the temperature increases further towards 150 °C. This trend mirrors that of the specific heat capacity despite the decreasing thermal diffusivity (Figure 61).





**Figure 61: Specific heat and thermal diffusivity against temperature for terthiophene functionalised SiNPs with a doping ratio of 0.5.**

The thermal conductivities obtained from this material are very low when compared to many inorganic materials and are comparable to that of conductive polymers. There are a number of reasons for this. Firstly the density of this material is very low and less than 50 % that of bulk silicon. It is not surprising that this is observed as this material combines organics and silicon so the theoretical density is much higher than what can realistically be achieved. Additionally the processing conditions are likely to lead to a lower density, and both a higher pressure and a slightly raised temperature would lead to further densification. Regardless of the density the ligands should naturally reduce the thermal conductivity to levels more comparable with polymeric materials.<sup>123</sup>

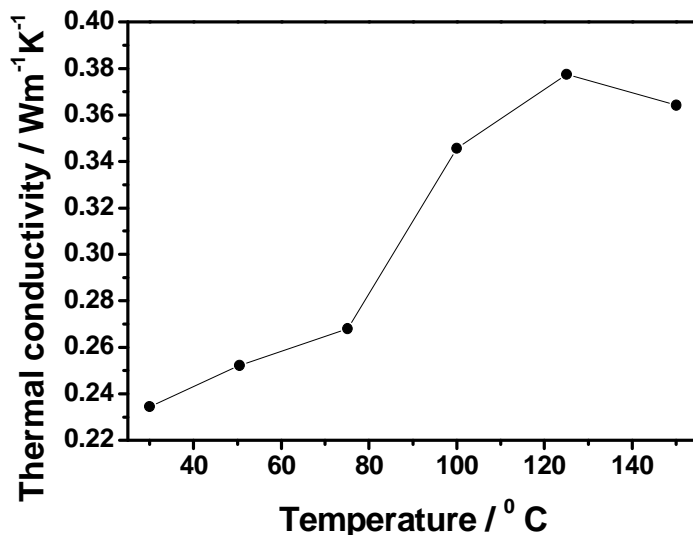
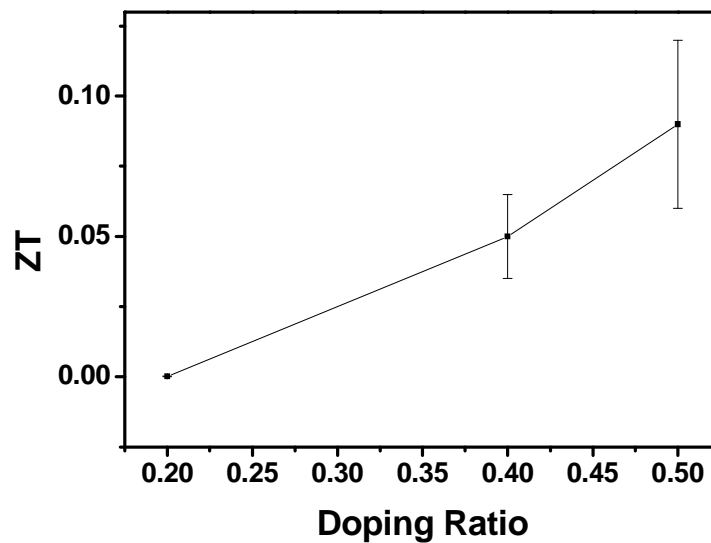


Figure 62: Temperature dependant thermal conductivity of a doped pellet of terthiophene functionalised SiNPs.

#### 5.6.5. Figure of Merit

The ZT of the material as the doping ratio increase shows a linear increase following the trends observed in the power factor measurements as would be expected. The ZT values obtained for pellets with doping ratios of 0.4 and 0.5 shows a significant improvement on those of bulk and nanostructured silicon. Although these values are nowhere near those of silicon nanowires and more relevantly those of phenylacetylene functionalised SiNPs, this material offers some valuable insights into the doping of organic ligands in such semiconductor-organic composite materials. Moreover this offers some evidence that ligand selection may have a vital role in the production of more effective silicon-organic composite thermoelectric materials. This is highlighted by the comparison with the phenylacetylene functionalised SiNPs describe in Chapter 4.



**Figure 63: ZT against doping ratio (Mass Terthiophene functionalised SiNPs/Mass NOBF4)**

The ZT values at ambient temperature show the same pattern as observed for the power factor showing an increase from 0.2 to 0.5 doping ratio. This is because the thermal conductivity remains constant as the doping ratio changes. The values obtained for the ZT have an error of approximately 15 % however for 0.4 and 0.5 we see an increase of at least 5 times that of the value of bulk silicon.<sup>104</sup>

Even though the ZT is very promising it is important to note that like with phenylacetylene functionalised SiNPs this is not the full picture. The materials main downfalls lie in its high resistivity and low power factor and ligand doping is only half the story

## 5.7. Summary

Terthiophene functionalized SiNPs have been successfully synthesised and this opens up potential for the introduction of larger oligomers on to the surface of such particles. However this work also highlights that with increased chain length the achievable surface coverage may be reduced further.

Furthermore a large decreasing resistivity was observed when a suitable oxidant was used to dope the ligands showing that doping attached ligands can lead to improvements in electrical conductivity. The minimum resistivity was observed at a doping ratio of 0.4 and the trends observed in the electrical resistivity as the dopant concentration was increased are similar to those observed in conductive polymers.

The Seebeck coefficients measured are very large. This can be mainly attributed to the high resistivity but it is also apparent that inhomogeneity in the material also plays a significant role in

the magnitude and the sign of this value. Both of these need to be addressed to move forward with such nanocomposite materials.

However based on these measurements the ZT values obtained are promising. However they do not tell the full story about the material with regards to its suitability for incorporation into a device and improvements to the power factor and more specifically the electrical resistivity need to be achieved before the application of this material can be considered.

**Chapter 6:**  
Electrochemical Etching  
Approach to the  
Synthesis of  
Phenylacetylene  
Functionalised Silicon  
Nanoparticles

## 6.1. Overview

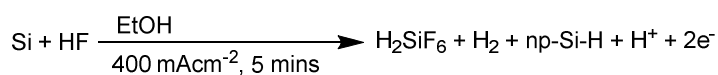
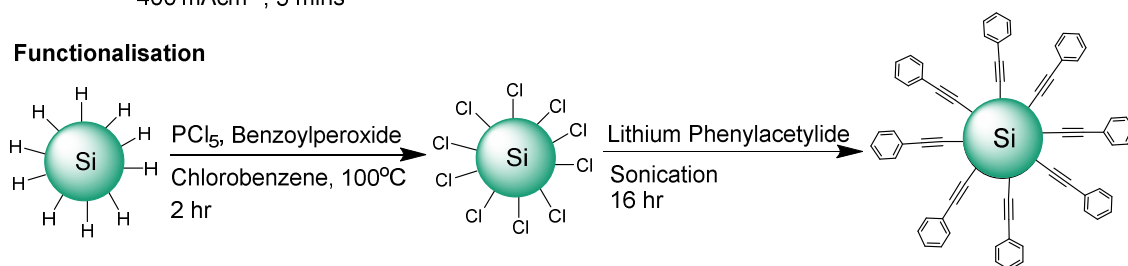
Despite the advantages discussed in chapter 4, solution approaches to SiNPs have two major drawbacks limiting their application in thermoelectrics: The first of these is the crystallinity of the particles, which is vital for good electronic performance.<sup>221</sup> The major issue with bottom up approaches to SiNPs is that highly crystalline particles can be difficult to obtain. Secondly, doping these materials so they are suitable for electronic applications is difficult. This generally requires high temperature processing.<sup>222</sup> When using surface functionalization to enhance the thermoelectric performance heating the sample to these temperatures is not desirable.

However with top down approaches the composition of the raw material can be transferred to the particles. This way it is possible to control the carrier concentration and as a result enhance the conductivity of the silicon based material discussed in Chapter 4. Electrochemical etching or ball milling are the most common approaches to producing such particles. Ball milling produces large volumes of material at low cost but with much higher particle sizes than bottom up approaches, generally no smaller than 60 nm, although crystal sizes lower than 10 nm from such methods have been documented.<sup>223</sup> With electrochemical etching it is difficult to obtain particles on a large scale, making the use of such particles in the fabrication of materials more difficult. However the particles produced by this method are generally much smaller and display quantum confinement effects.<sup>41, 80, 81, 186</sup>

Hydrogen terminated SiNPs were produced via electrochemical etching, using a method published by Wang *et al.*<sup>73</sup> These freshly etched H terminated SiNPs were chlorinated using thermally induced radical halogenation using phosphorus pentachloride and benzoyl chloride, followed by alkylation using lithium phenylacetylide to produce phenylacetylene functionalised SiNPs.<sup>171, 224</sup> This product was characterised by FTIR, <sup>1</sup>HNMR, <sup>13</sup>CNMR, <sup>31</sup>PNMR, TEM and XPS. The thermal stability of this material was also analysed using TGA and DSC.

## 6.2. Synthesis of Phenylacetylene Functionalised SiNPs

Silicon chips were etched at a current density  $400 \mu\text{Acm}^{-2}$ , for 5 min. These were chlorinated by heating a mixture of benzoyl peroxide and phosphorus pentachloride at 90 °C for 2 h in dry chlorobenzene. After drying lithium phenylacetylide was added and the mixture was heated at 50 °C for 16 hours. See **Scheme 18**:

**Particle Synthesis by Electrochemical Etching****Functionalisation****Scheme 22: Functionalisation of hydrogen functionalised SiNPs using a chlorination- alkylation approach.**

After washing and the removal of solvent 20 mg of a dark orange solid was obtained. This low yield meant that insufficient material was produced to make the pellets required to run thermoelectric measurements.

**6.3. Characterisation of Phenylacetylene Functionalised SiNPs**

FTIR confirmed the presence of the phenylacetylene functionalization as it showed a peak at  $3054 \text{ cm}^{-1}$  for the aromatic C-H stretches and a sharp peak at  $2170 \text{ cm}^{-1}$  which is characteristic of a  $\text{C}\equiv\text{C}$  stretch. Also, C-C and Si-C stretches at  $1488$  and  $1442 \text{ cm}^{-1}$  and C=C aromatic stretches were observed at  $1598 \text{ cm}^{-1}$  and Si-C stretching at  $1206 \text{ cm}^{-1}$ . This spectrum also shows a broad peak in the region of  $1000$  and  $1100 \text{ cm}^{-1}$  which is characteristic of Si-O stretching. This is as a result of the working up process which requires washing in water, which results in the oxidation of any unfunctionalised surface. Strong evidence for the attachment of phenylacetylene to the particle surface is provided by the lack of a strong peak at  $3200 \text{ cm}^{-1}$ , which would otherwise correspond to a terminal C-H group on the alkyne and provide evidence of free (unbound) phenylacetylene.

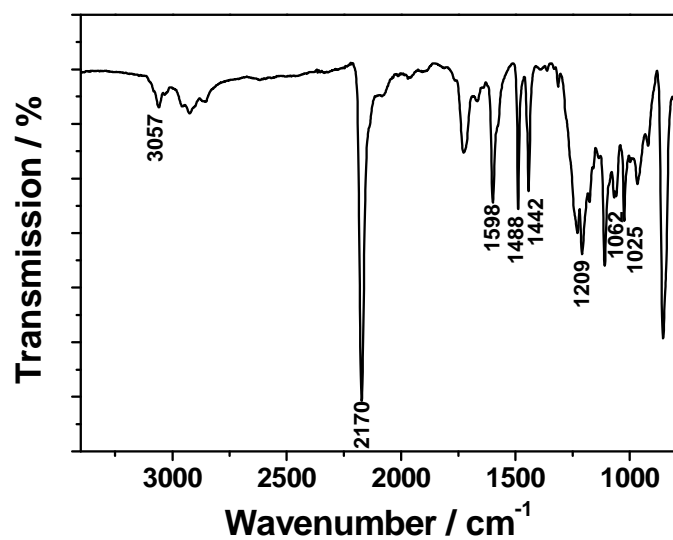


Figure 64: FTIR of phenylacetylene functionalised SiNPs synthesised by electrochemical etching.

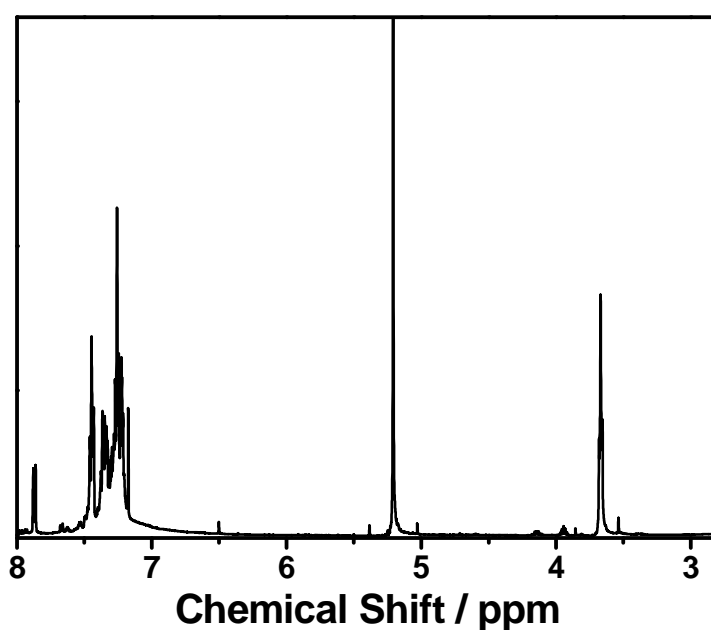


Figure 65: <sup>1</sup>H-NMR of phenylacetylene functionalised SiNPs synthesised by electrochemical etching.

<sup>1</sup>H-NMR shows aromatic peaks between 7.75 and 7 ppm. These peaks are characteristic of the phenyl ring on phenylacetylene. More importantly the absence of a peak at a chemical shift of 3 ppm, which is representative of the proton on the alkyne, supports the successful functionalisation with phenylacetylene.



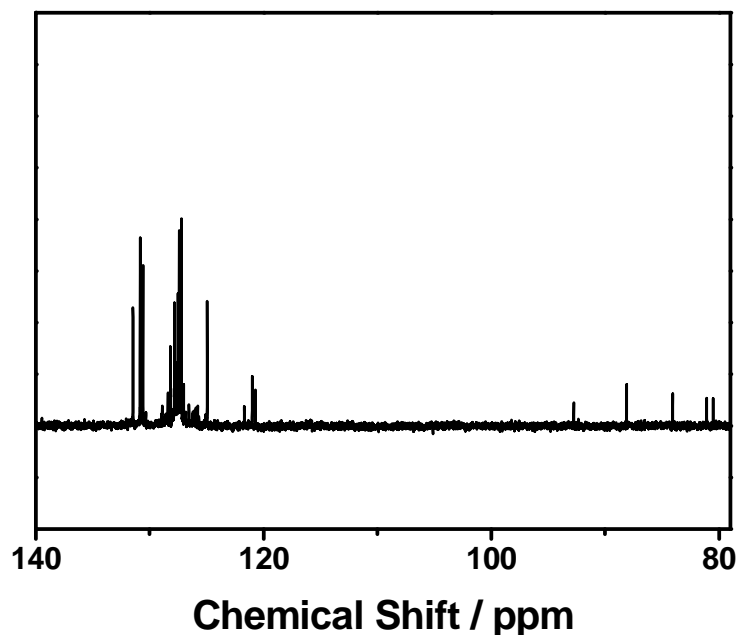
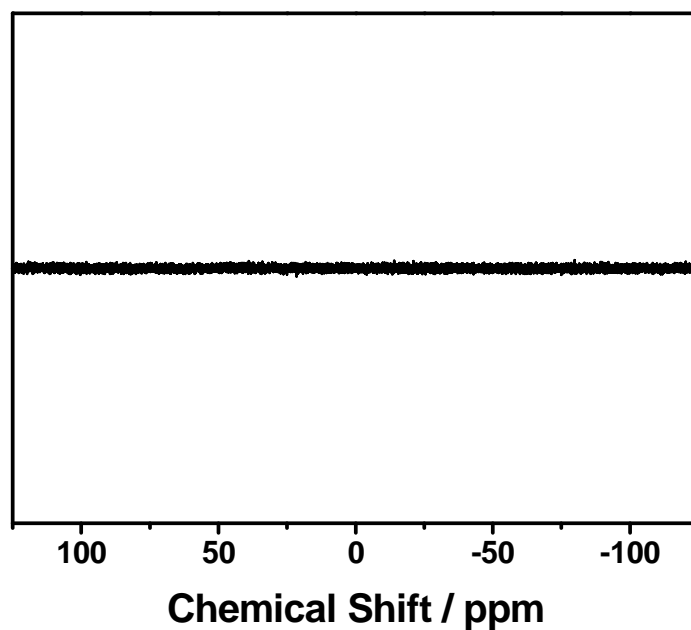


Figure 66:  $^{13}\text{C}$ -NMR of phenylacetylene functionalised SiNPs synthesised by electrochemical etching.

$^{13}\text{C}$ -NMR shows a number of alkyne carbons ranging from 95 to 80 to ppm. There is a higher number of peaks when compared to the  $^{13}\text{C}$ -NMR for the bottom up phenylacetylene functionalised SiNPs. This could have been attributed to phosphorus based by-products from the functionalisation process. However the  $^{31}\text{P}$  NMR does not show any signs of phosphorous impurities so this can be neglected. This suggests that the bonding environments may differ on the surface of silicon. It is documented that there are a number of different surface environments on the surface of porous silicon including;  $\text{SiH}$ ,  $\text{SiH}_2$ ,  $\text{SiH}_3$  and a number environments related to bridging oxide species.<sup>225</sup>

In addition to this peaks are also observed in the aromatic region. These peaks between 132 and 120 ppm are in similar positions to the carbons of the phenyl ring of phenylacetylene and offer further evidence of successful functionalisation. The same unexpected high number of peaks is also observed in the aromatic region.



**Figure 67:**  $^{31}\text{P}$ -NMR of phenylacetylene functionalised SiNPs synthesised by electrochemical etching.

The XPS survey spectrum (**Figure 68**) shows intense peaks for O1s, C1s, Si2s and Si2p, showing that the elemental composition of the phenylacetylene functionalised SiNPs does not include any of the potential by-products from the functionalization reaction, such as Li, Cl and P. The O1s peak is more intense than would be expected from the intensity of the Si-O stretch on the FTIR, but this can be attributed to the x-ray induced oxidation of the particle surface.<sup>185</sup>

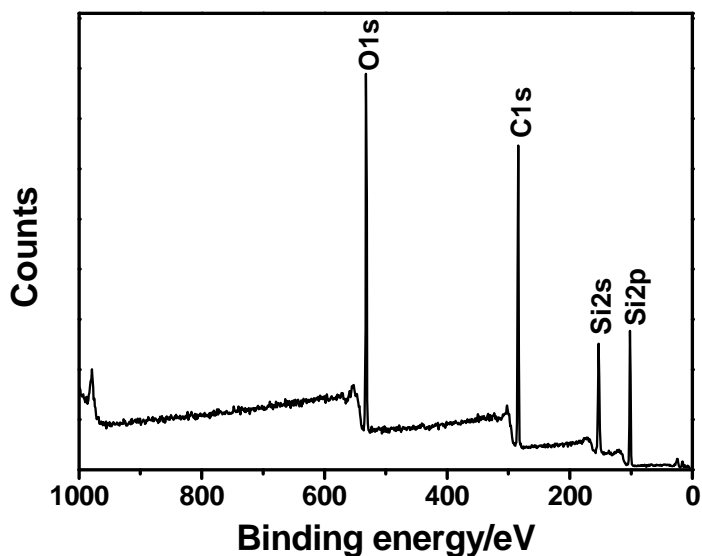


**Figure 68: XPS Survey Spectrum of top down phenylacetylene functionalised SiNPs synthesised by electrochemical etching.**

In **Figure 69** the Si2p spectrum for phenylacetylene functionalised SiNPs is fitted with two components: at 101.59 eV, and 102.12 eV representing contributions from Si-C and Si-O respectively<sup>185, 186</sup>. There is no visible peak at approximately 100 eV representing the Si-Si bonding within the centre of the nanoparticles. This is likely to be as a result of the penetration depth of the X-rays as a result of the oxide and ligands present on the particles surface. As a result 100% of the peak area is as a result of Si-C and Si-O at the particle surface, 38.0 % is from Si-C and the remainder 62.0 % is from Si-O and SiO<sub>2</sub> meaning an estimated 38 % of the available surface has undergone capping. This is low when compared with H-terminated Si(111) surfaces bound by organic monolayers using hydrosilylation, where approximately 50 % surface coverage is typical<sup>111, 112</sup> although when attaching conjugated ligands using hydrosilylation, the surface coverage is much lower, as discussed by Veinot *et. al.*<sup>102</sup>

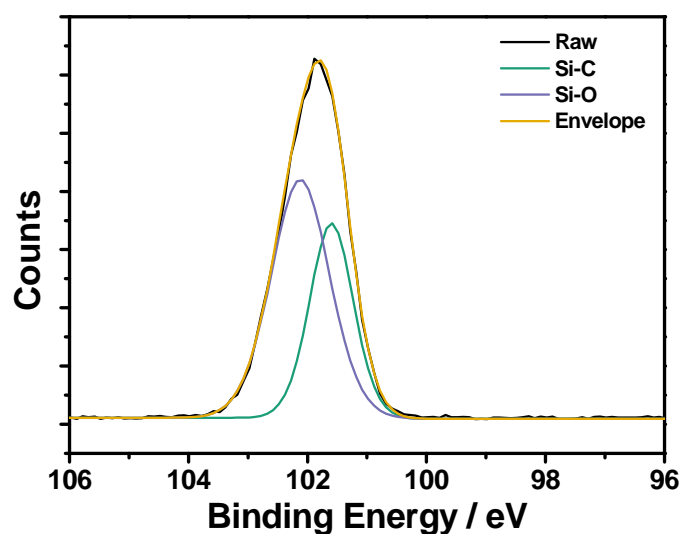


**Figure 69: XPS spectra obtained for phenylacetylene functionalised SiNPs showing high resolution spectrum of Si2p region. Photoelectron spectrum was collected with incident photon energy of 1486.6 eV.**

In **Figure 70** the C1s spectrum for terthiophene SiNPs is fitted with two components: C-C at 284.4 eV, Si-C at 283.8 eV. 86.5 % of the spectrum area is from C-C within the carbon chains and the remaining 13.5 % is made up by the Si-C where the passivating layer is bound to the silicon centre. The ratio of the area of the spectrum represented by each component is close to 1:6.5, which is close to the ratio of Si-C to C-C bonds in the functionalised SiNPs. Some of the discrepancy in this value could be attributed to the attachment of small amounts of butyl groups as a result of unreacted n-butyllithium in the preparation of lithiumphenylacetylide.

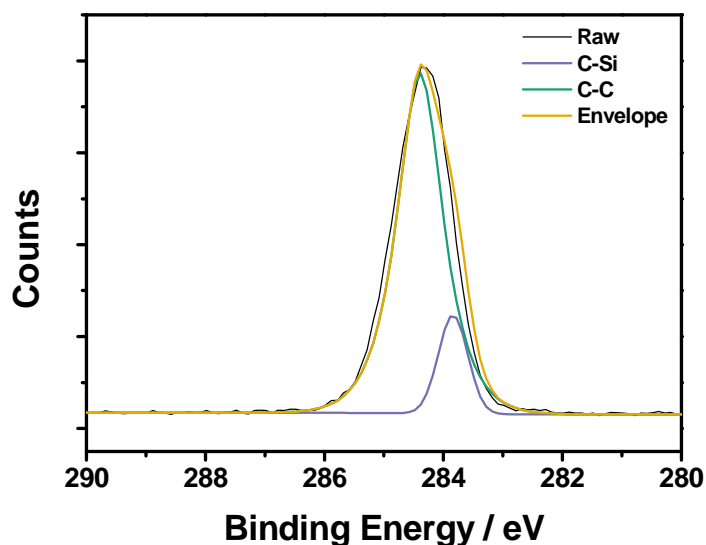


**Figure 70: XPS spectra obtained for phenylacetylene functionalised SiNPs showing high resolution spectrum of O1s region. Photoelectron spectrum was collected with incident photon energy of 1486.6 eV.**

TEM micrographs of phenylacetylene functionalised SiNPs produced by electrochemical etching show irregular due to their porous nature, as can be observed in **Figure 71**. The average particle diameter is taken as approximately 7 nm with a standard deviation of 1.4 nm. This size distribution can also be observed from the size distribution chart (see insert **Figure 71**) which shows particle sizes ranging from 3 to 10 nm in diameter. Narrow particle size distributions in electrochemical etching of SiNPs result from maintenance of a constant charge density throughout the process.<sup>73</sup> This distribution is narrower than for SiNPs produced via the micelle reduction approach as previously documented. This is not surprising as the synthetic approach used does not use surfactants. In micelle reduction processes a suitable surfactant greatly reduces the size distribution.

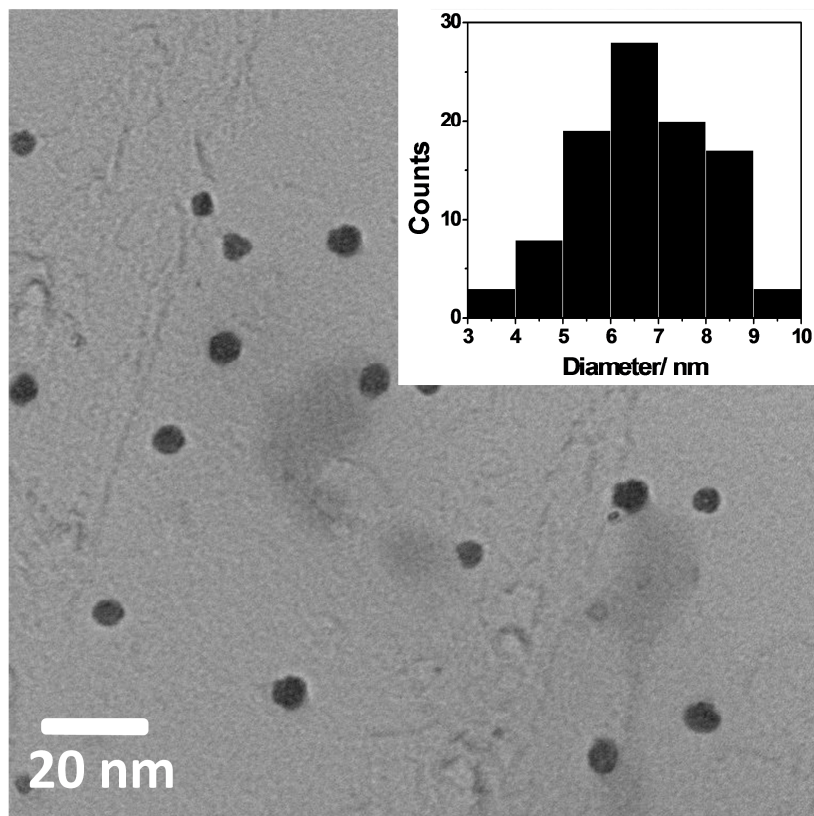


**Figure 71: TEM image of phenylacetylene functionalised SiNPs synthesized by electrochemical etching. Inset histogram showing particle size distribution**

#### 6.4. Thermal Stability

The DSC trace (Figure 73) has a general downward trend throughout the measurement. Initially the weight on the TGA trace (Figure 72Error! Reference source not found.) remains close to 100 %. After this feature there is a small shoulder on the heat flow, which suggests that the sample is beginning to undergo degradation. In this region a minima is observed in the derivative of the TGA showing a higher rate of weight loss at this point. However the weight loss observed is much smaller than observed on the bottom up sample. The DSC trace reaches a maximum at 320 °C showing completion of the initial degradation. After 330 °C the heat flow into the sample returns to the initial downward trend and the TGA trace shows that the weight continues to decrease slowly. At 500 °C a rapid weight loss can be observed, as depicted by another sharper minimum on the derivative. This is likely to be due to continued degradation. This corresponds to the start of a broad shoulder in the DSC. After 650 °C little change in weight occurs on the TGA which suggests that degradation is complete. The overall percentage weight loss at 1000 °C is 90 %. Assuming that all remaining material is silicon as a result of heating in an inert atmosphere, the ligand to silicon ratio is 3 to 1 suggesting a very high surface coverage. However this is a rough estimation of the coverage as it assumes all remaining material is solely silicon and all weight loss is as a result of

degradation of ligands which may also be related to other processes such as desorption of physisorbed ligands and the evaporation of functionalised SiNPs.<sup>80, 85, 168</sup> XPS offers a more accurate and complete estimation of surface coverage.

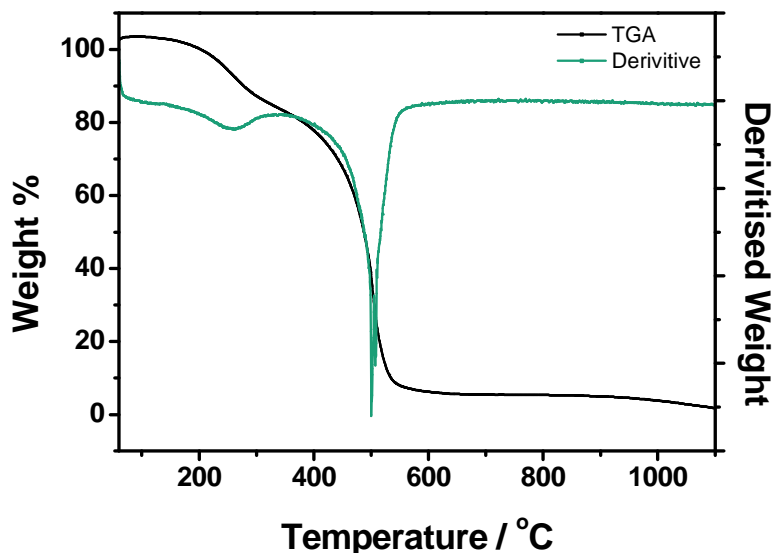


Figure 72: TGA trace and derivative between 50 and 1000 °C for phenylacetylene functionalised SiNPs synthesized by electrochemical etching.

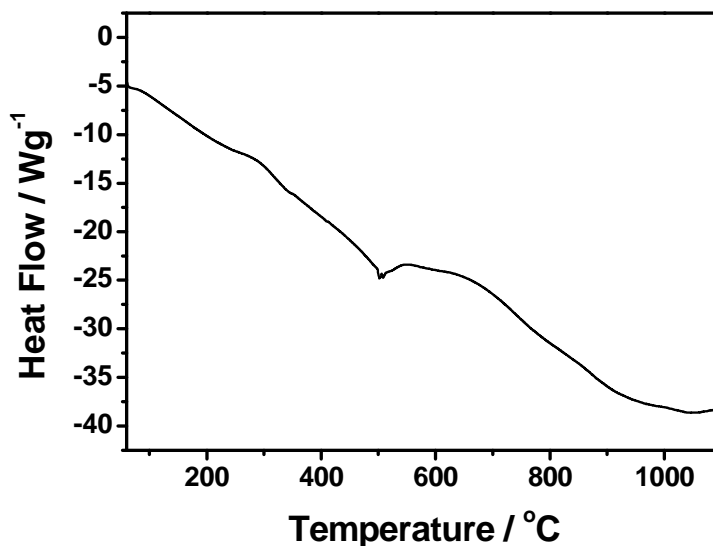


Figure 73: DSC trace between 50 and 1000 °C for phenylacetylene functionalised SiNPs synthesized by electrochemical etching.


## 6.5. Summary

Top down synthesis of PA-SiNPs by electrochemical etching is a viable synthetic method and produces suitably functionalised particles. This method, if scaled up, might allow significant study

of the effect of the charge carrier concentration of the PA-SiNPs on their thermoelectric performance. Furthermore, the thermal stability studies suggest that this material is better suited to a wider range of thermoelectric applications than its bottom up counterpart.

The ability to produce phenylacetylene functionalised SiNPs by this method is a significant step towards being able to produce a material where the SiNPs are suitably doped. As a result this will aid the study of how doping the nanoparticles would affect the thermoelectric performance of materials based on this system. However the scalability is a significant barrier as our typical electrochemical etching only offers a maximum of 2- 4 mg of material per chip when at least 250 - 500 mg is required to produce a pellet suitable for measurement and considerably higher quantities are required for fabrication of a device





# Chapter 7:

## Conclusions and Future Work

## 7.1. Conclusions

The one-pot synthesis of alkyl- functionalised SiNPs, as outlined in Chapter 3 is easy and viable for a wide range of capping (surfactant) chains, offering a wide range of potential functionalisation such as amine or allyl end groups. In this work the level of alkyl capping, despite initial appearances, is broadly consistent for all capping layers, although some experiments show a raised level of Si-O. This is because the quenching solvent used in this method reacts with the unfunctionalised Si-H on the surface of the particle. It has been shown that the SiNPs produced by this method are silicon rich, crystalline, luminescent, and functionalised with alkyl chains. Additionally these particles can be produced in higher yields and with higher surface coverage than those produced by other methods and as a result make them a more viable candidate for the mass production of functionalised SiNPs.

Phenylacetylene functionalised SiNPs as synthesised in chapter 4 show a solution reduction method to produce more versatile chlorine terminated SiNPS and demonstrates how it is possible to functionalise them by nucleophilic substitution using a suitable organometallic or nucleophile. In this case the use of a conjugated ligand was highly attractive with regards to its ability to transport electrons. A number of other conjugated ligands, such as oligothiophenes, would be interesting candidates for fine tuning this system and this approach opens up the potential to produce such SiNPS.

The ZT of 0.6 obtained for a pellet of phenylacetylene functionalised SiNPS is very high for an organic inorganic nanocomposite material. Although the materials after the processing are not suitable for use in a device in their current state, due to low thermal stability and high resistivity, some key advancements have been made.

Firstly the pellet produced shows a higher conductivity than purely silicon materials, of comparable porosity, which has been achieved without any control of charge carriers. This would allow further optimisation of the system. Additionally the thermal conductivity has been reduced to a level comparable with organic materials, which is a key advantage of combining organics with inorganic nanostructures.

The high resistivity on the material described in chapter 4 is likely to be related to insufficient charge carriers. However in this composite material there are two components and the effects of doping each of these components must be considered separately. These components are the ligand and the nanoparticle.

The investigation of doping the ligands was carried out on a different ligand as a consequence of the difficulty of doping phenylacetylene. The synthesis of terthiophene functionalised SiNPs allowed for the attachment of a form of ligand in which the doping was well documented.

In materials doped with different levels of  $\text{NOBF}_4$  it was clear to see that as the level of doping of the ligands increased so did the electrical conductivity. An optimum doping concentration was obtained when a mass ratio of 0.4  $\text{NOBF}_4$  to terthiophene functionalised SiNPs was used. This material unsurprisingly behaves in a similar way to conductive polymers with regards to the level of doping.

As described in chapter 4 for phenylacetylene functionalised SiNPs produced by the same method, terthiophene functionalised SiNPs also display a high and unstable Seebeck coefficient. However unlike the undoped material described previously this material would be expected to be n-doped however the sign of the Seebeck coefficient on some measurements suggested that it had been p-doped. This evidence further supports inhomogeneity in the sample.

However based on these measurements the ZT values obtained are promising, although as mentioned previously do not tell the full story about the material with regards to its suitability for incorporation into a device as once again the electrical resistivity is much too high for commercial use.

The effects of ligand doping is one step toward understanding these inorganic-organic nanocomposites but for the full picture it is important to understand the effects of doping the nanoparticle. This is synthetically more complicated than ligand doping and bottom up methods generally require high temperature processing after the introduction of the impurity, which is unpractical with organic surface ligands. Electrochemical etching is a way to produce nanoparticles with charge carriers as this can be transferred directly from the starting material. Being able to functionalise the particles is essential, before they can be tested.

The successful production of phenylacetylene functionalised SiNPs by electrochemical etching offers a significant step towards optimising phenylacetylene functionalised SiNP based materials. However the scalability does offer a significant barrier as our typical electrochemical etching only offers a maximum of 2- 4 mg of material per chip when at least 250 - 500 mg is required to produce a pellet suitable for measurement.

The body of work in this thesis describes steps toward understanding and developing organic inorganic nanocomposite materials using functionalised SiNPs. However, to date the fundamental understanding of both; the potential and the optimisation of such materials are very limited.

These types of materials in the future may offer a more versatile alternative for low temperature thermoelectrics than the more traditional solid state inorganic materials.

## 7.2. Future Work

Future work on SiNP-organic nanocomposites will mainly relate to a number of variables which would lead to improving the electrical resistivity the system. As highlighted by the theoretical work by Wang *et. al.*<sup>226</sup> matching the band gaps suitably between the organic chain and the quantum dot is vital so unsurprisingly the ligand is central to producing an effective system. However changes to the particle itself may also aid the fine tuning of this system.

### 7.2.1. Doping SiNPs

During this work it was not possible to investigate the effect of the doping SiNPs component of the material on the thermoelectric properties. Only a synthetic approach was developed. This is something which would be vital for better understanding of these systems. It has been documented by See *et. al.*<sup>166</sup> that the n-doping of BiTe nanorods is transferred to the material more strongly than the p-doping in PEDOT:PSS in this particular nanocomposite. This could mean that both n and p-type materials can be produced without changing the doping method for the polymer. If the same phenomenon is observed in these SiNP based materials, this would make these materials a more viable option for use in thermoelectric devices.

### 7.2.2. Ligands and Surface Coverage

For terthiophene functionalised SiNPs, it was apparent that the surface coverage was low and as a result the level of oxide on the surface was high. A coating of oxide will have detrimental effects on the electrical conductivity of the material. It appears that in this case, there is a trade-off between the length of the chain and the surface coverage obtained when we compare the surface coverage to that of phenylacetylene functionalised particles. Current work in the Chao group has also shown that this is the case for thiophene functionalised SiNPS as well. This suggests that the introduction of a monomer rather than an oligomer is a more attractive route for the development of a SiNP organic nanocomposite material as it reduces the surface oxide. Although thiophene has already been attached to SiNPs, other potential candidates include ethyldioxythiophene and aniline.

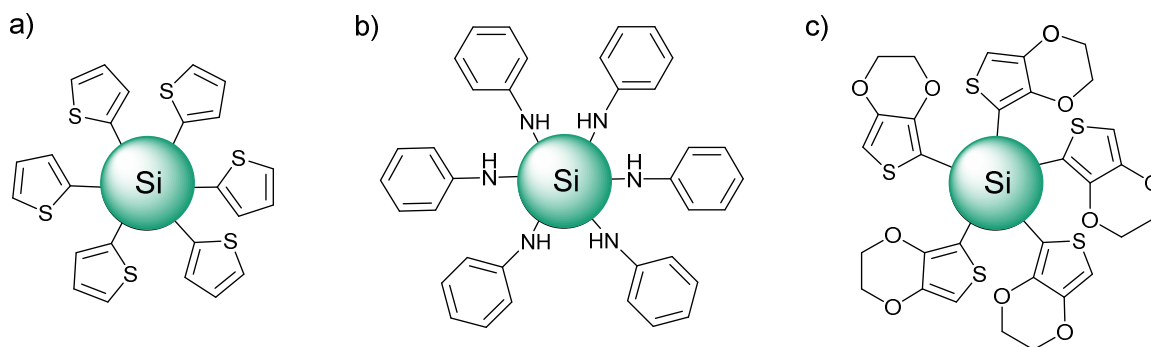
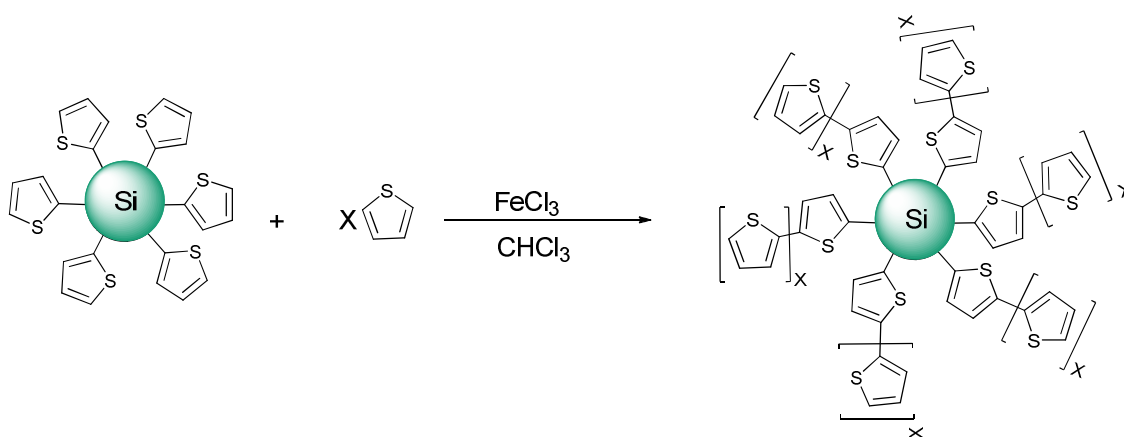


**Figure 74: SiNPs functionalised with different monomers, a) thiophene b) aniline c) ethylenedioxythiophene.**

These monomers are relatively easy to attach, however these materials rely on good overlap between organic chains to provide sufficient conductivity. As a result single aromatic rings are unlikely to offer sufficient overlap. These monomers are interesting in that they can undergo oxidative polymerisation. If a controlled amount of monomer and an oxidising agent are introduced, polymerisation of the nanoparticle surface may occur. This is demonstrated below for thiophene functionalised SiNPs.



**Scheme 23: Oxidative polymerisation on the surface of thiophene functionalised SiNPs**

Although this is demonstrated as a clean reaction above, it is far from such as there are a number of other species that may make up the material including; SiNPs cross-linked with poly or oligothiophenes and free unattached oligothiophenes. This is something that would be difficult to control.

For the surface functionalisation and potential crosslinking described above optimisation of the doping of the organic species is going to be essential for optimising material performance. Chapter 5 shows that the doping of the ligands can have a significant effect on the electrical

resistivity. As a result optimisation of doping for any organic component is going to be paramount to the success of these types of material.

### 7.2.3. Theoretical Understanding

It was mentioned earlier that a study has been carried out by Wang *et. al.*<sup>226</sup> This offered some very helpful insights into the potential and the optimisation of organic-inorganic nanocomposite systems. This work is a significant step forward but, otherwise, there is very little published work on understanding these materials. It is clear that a greater depth of theoretical understanding would aid the design of materials that could compete with their solid state counterparts. Such studies are outside of the scope of this work but would have a significant bearing on the future success of these types of materials.



# References

1. Dowling A, Clift R, Grobert N, Hutton D, Oliver R, O'neill O, Pethica J, Pidgeon N, Porritt J, Ryan J. Nanoscience and nanotechnologies: opportunities and uncertainties. London: The Royal Society & The Royal Academy of Engineering Report 2004: 61-64.
2. Pitcher MW. Nanochemistry - A chemical approach to nanomaterials. *Science* 2006;313(5785): 300-00.
3. Lindsay S. Introduction to nanoscience. Oxford: Oxford University Press, 2010.
4. Lee J-H, Galli GA, Grossman JC. Nanoporous Si as an Efficient Thermoelectric Material. *Nano Letters* 2008;8: 3750-54.
5. Lertsatitthanakorn C, Rungsiyopas M, Therdyothin A, Soponronnarit S. Performance Study of a Double-Pass Thermoelectric Solar Air Collector with Flat-Plate Reflectors. *Journal of Electronic Materials* 2012;41: 999-1003.
6. Mauter MS, Elimelech M. Environmental applications of carbon-based nanomaterials. *Environmental Science & Technology* 2008;42(16): 5843-59.
7. Li H, Liu S, Dai Z, Bao J, Yang X. Applications of Nanomaterials in Electrochemical Enzyme Biosensors. *Sensors* 2009;9(11): 8547-61.
8. Chen X, Mao SS. Titanium dioxide nanomaterials: synthesis, properties, modifications, and applications. *Chemical Reviews* 2007;107(7): 2891-959.
9. Barreto JA, O'Malley W, Kubeil M, Graham B, Stephan H, Spiccia L. Nanomaterials: Applications in Cancer Imaging and Therapy. *Advanced Materials* 2011;23(12): H18-H40.
10. Novoselov KS, Geim AK, Morozov SV, Jiang D, Zhang Y, Dubonos SV, Grigorieva IV, Firsov AA. Electric Field Effect in Atomically Thin Carbon Films. *Science* 2004;306(5696): 666-69.
11. Lalmi B, Oughaddou H, Enriquez H, Kara A, Vizzini S, Ealet B, Aufray B. Epitaxial growth of a silicene sheet. *Applied Physics Letters* 2010;97(22): -.
12. Liu H, Neal AT, Zhu Z, Luo Z, Xu X, Tománek D, Ye PD. Phosphorene: An Unexplored 2D Semiconductor with a High Hole Mobility. *ACS Nano* 2014;8(4): 4033-41.
13. Dreyer DR, Ruoff RS, Bielawski CW. From Conception to Realization: An Historical Account of Graphene and Some Perspectives for Its Future. *Angewandte Chemie International Edition* 2010;49(49): 9336-44.
14. Sun Y, Wu Q, Shi G. Graphene based new energy materials. *Energy & Environmental Science* 2011;4(4): 1113-32.
15. Pumera M. Graphene in biosensing. *Materials Today* 2011;14(7-8): 308-15.



16. Park S, Ruoff RS. Chemical methods for the production of graphenes. *Nat Nano* 2009;4(4): 217-24.
17. Novoselov KS. Graphene: Materials in the Flatland (Nobel Lecture). *Angewandte Chemie International Edition* 2011;50(31): 6986-7002.
18. Bonaccorso F, Sun Z, Hasan T, Ferrari AC. Graphene photonics and optoelectronics. *Nat Photon* 2010;4(9): 611-22.
19. Nair RR, Blake P, Grigorenko AN, Novoselov KS, Booth TJ, Stauber T, Peres NMR, Geim AK. Fine Structure Constant Defines Visual Transparency of Graphene. *Science* 2008;320(5881): 1308.
20. Bonanni A, Pumera M. Graphene platform for hairpin-DNA-based impedimetric genosensing. *ACS Nano* 2011;5(3): 2356-61.
21. Mao S, Lu G, Yu K, Bo Z, Chen J. Specific protein detection using thermally reduced graphene oxide sheet decorated with gold nanoparticle-antibody conjugates. *Advanced Materials* 2010;22(32): 3521-26.
22. Eda G, Chhowalla M. Chemically Derived Graphene Oxide: Towards Large-Area Thin-Film Electronics and Optoelectronics. *Advanced Materials* 2010;22(22): 2392-415.
23. Cui J. Zinc oxide nanowires. *Materials Characterization* 2012;64(0): 43-52.
24. Gudixsen MS, Wang J, Lieber CM. Size-Dependent Photoluminescence from Single Indium Phosphide Nanowires. *The Journal of Physical Chemistry B* 2002;106(16): 4036-39.
25. Heitsch AT, Akhavan VA, Korgel BA. Rapid SFLS Synthesis of Si Nanowires Using Trisilane with In situ Alkyl-Amine Passivation. *Chemistry of Materials* 2011;23: 2697-99.
26. Heitsch AT, Fanfair DD, Tuan H-Y, Korgel BA. Solution-Liquid-Solid (SLS) Growth of Silicon Nanowires. *Journal of the American Chemical Society* 2008;130(16): 5436-37.
27. Chan CK, Patel RN, O'Connell MJ, Korgel BA, Cui Y. Solution-Grown Silicon Nanowires for Lithium-Ion Battery Anodes. *ACS Nano* 2010;4(3): 1443-50.
28. Dasgupta NP, Sun J, Liu C, Brittman S, Andrews SC, Lim J, Gao H, Yan R, Yang P. 25th Anniversary Article: Semiconductor Nanowires – Synthesis, Characterization, and Applications. *Advanced Materials* 2014;26: 2137-84.
29. Peng K, Xu Y, Wu Y, Yan Y, Lee S-T, Zhu J. Aligned Single-Crystalline Si Nanowire Arrays for Photovoltaic Applications. *Small* 2005;1: 1062-67.

30. Xia Y, Yang P, Sun Y, Wu Y, Mayers B, Gates B, Yin Y, Kim F, Yan H. One-Dimensional Nanostructures: Synthesis, Characterization, and Applications. *Advanced Materials* 2003;15: 353-89.
31. Ahire JH, Chambrier I, Mueller A, Bao Y, Chao Y. Synthesis of D-mannose capped silicon nanoparticles and their interactions with MCF-7 human breast cancerous cells. *ACS Applied Materials & Interfaces* 2013;5: 7384-91.
32. Jana NR, Gearheart L, Murphy CJ. Wet Chemical Synthesis of High Aspect Ratio Cylindrical Gold Nanorods. *The Journal of Physical Chemistry B* 2001;105: 4065-67.
33. Jana NR, Gearheart L, Murphy CJ. Wet Chemical Synthesis of High Aspect Ratio Cylindrical Gold Nanorods. *The Journal of Physical Chemistry B* 2001;105(19): 4065-67.
34. Xia Y, Yang P, Sun Y, Wu Y, Mayers B, Gates B, Yin Y, Kim F, Yan H. One-Dimensional Nanostructures: Synthesis, Characterization, and Applications. *Advanced Materials* 2003;15(5): 353-89.
35. Iijima S. Helical microtubules of graphitic carbon. *Nature* 1991;354(6348): 56-58.
36. Guldi DM, Rahman GMA, Prato M, Jux N, Qin S, Ford W. Single-Wall Carbon Nanotubes as Integrative Building Blocks for Solar-Energy Conversion. *Angewandte Chemie* 2005;117(13): 2051-54.
37. Zhang M, Fang S, Zakhidov AA, Lee SB, Aliev AE, Williams CD, Atkinson KR, Baughman RH. Strong, Transparent, Multifunctional, Carbon Nanotube Sheets. *Science* 2005;309(5738): 1215-19.
38. Bear JC, Hollingsworth N, McNaughter PD, Mayes AG, Ward MB, Nann T, Hogarth G, Parkin IP. Copper-Doped CdSe/ZnS Quantum Dots: Controllable Photoactivated Copper(I) Cation Storage and Release Vectors for Catalysis. *Angewandte Chemie International Edition* 2014;53(6): 1598-601.
39. Zorman B, Ramakrishna MV, Friesner RA. Quantum Confinement Effects in CdSe Quantum Dots. *The Journal of Physical Chemistry* 1995;99: 7649-53.
40. Bear JC, Yu B, Blanco-Andujar C, McNaughter PD, Southern P, Mafina M-K, Pankhurst QA, Parkin IP. A low cost synthesis method for functionalised iron oxide nanoparticles for magnetic hyperthermia from readily available materials. *Faraday Discussions* 2014.
41. Bouaïcha M, Khardani M, Bessaïs B. Evaluation of the electrical conductivity of nano-porous silicon from photoluminescence and particle size distribution. *Materials Science and Engineering: B* 2008;147: 235-38.

- 
42. Gesele G, Linsmeier J, Drach V, Fricke J, Arens-Fischer R. Temperature-dependent thermal conductivity of porous silicon. *Journal of Physics D: Applied Physics* 1997;30: 2911.
43. Xie YH, Wilson WL, Ross FM, Mucha JA, Fitzgerald EA, Macaulay JM, Harris TD. Luminescence and structural study of porous silicon films. *Journal of Applied Physics* 1992;71: 2403-07.
44. Joshi G, Lee H, Lan Y, Wang X, Zhu G, Wang D, Gould RW, Cuff DC, Tang MY, Dresselhaus MS, Chen G, Ren Z. Enhanced Thermoelectric Figure-of-Merit in Nanostructured p-type Silicon Germanium Bulk Alloys. *Nano Letters* 2008;8: 4670-74.
45. Poudel B, Hao Q, Ma Y, Lan Y, Minnich A, Yu B, Yan X, Wang D, Muto A, Vashaee D, Chen X, Liu J, Dresselhaus MS, Chen G, Ren Z. High-Thermoelectric Performance of Nanostructured Bismuth Antimony Telluride Bulk Alloys. *Science* 2008;320: 634-38.
46. O'Farrell N, Houlton A, Horrocks BR. Silicon nanoparticles: applications in cell biology and medicine. *International Journal of Nanomedicine* 2006;1(4): 451-72.
47. Pavese L, Dal Negro L, Mazzoleni C, Franzo G, Priolo F. Optical gain in silicon nanocrystals. *Nature* 2000;408: 440-44.
48. Reboredo FA, Galli G. Theory of alkyl-terminated silicon quantum dots. *Journal Of Physical Chemistry B* 2005;109(3): 1072-78.
49. Rosso-Vasic M, Spruijt E, van Lagen B, De Cola L, Zuilhof H. Alkyl-Functionalized Oxide-Free Silicon Nanoparticles: Synthesis and Optical Properties. *Small* 2008;4(10): 1835-41.
50. Semonin OE, Luther JM, Beard MC. Quantum dots for next-generation photovoltaics. *Materials Today* 2012;15(11): 508-15.
51. Kairdolf BA, Smith AM, Stokes TH, Wang MD, Young AN, Nie S. Semiconductor Quantum Dots for Bioimaging and Bidiagnostic Applications. *Annual review of analytical chemistry (Palo Alto, Calif.)* 2013;6(1): 143-62.
52. Rosso-Vasic M, Spruijt E, Popovic Z, Overgaag K, van Lagen B, Grandidier B, Vanmaekelbergh D, Dominguez-Gutierrez D, De Cola L, Zuilhof H. Amine-terminated silicon nanoparticles: synthesis, optical properties and their use in bioimaging. *Journal of Materials Chemistry* 2009;19: 5926-33.
53. Woggon U, Gaponenko S, Langbein W, Uhrig A, Klingshirn C. Homogeneous linewidth of confined electron-hole-pair states in II-VI quantum dots. *Physical Review B* 1993;47(7): 3684-89.
54. Fendler JH, Meldrum FC. The Colloid Chemical Approach to Nanostructured Materials\*\*. *Advanced Materials* 1995;7(7): 607-32.

55. Henglein A. Small-particle research: physicochemical properties of extremely small colloidal metal and semiconductor particles. *Chemical Reviews* 1989;89(8): 1861-73.
56. Alivisatos AP. Perspectives on the Physical Chemistry of Semiconductor Nanocrystals. *The Journal of Physical Chemistry* 1996;100(31): 13226-39.
57. Hagfeldt A, Graetzel M. Light-Induced Redox Reactions in Nanocrystalline Systems. *Chemical Reviews* 1995;95(1): 49-68.
58. Brus LE. Electron–electron and electron-hole interactions in small semiconductor crystallites: The size dependence of the lowest excited electronic state. *The Journal of Chemical Physics* 1984;80(9): 4403-09.
59. Zorman B, Ramakrishna MV, Friesner RA. Quantum Confinement Effects in CdSe Quantum Dots. *The Journal of Physical Chemistry* 1995;99(19): 7649-53.
60. Rama Krishna MV, Friesner RA. Quantum confinement effects in semiconductor clusters. *The Journal of Chemical Physics* 1991;95(11): 8309-22.
61. Nirmal M, Brus L. Luminescence Photophysics in Semiconductor Nanocrystals. *Accounts of Chemical Research* 1998;32(5): 407-14.
62. Einevoll GT. Confinement of excitons in quantum dots. *Physical Review B* 1992;45(7): 3410-17.
63. Kang Z, Liu Y, Lee S-T. Small-sized silicon nanoparticles: new nanolights and nanocatalysts. *Nanoscale* 2011;3(3): 777-91.
64. Pavesi L, Turan R. Introduction. *Silicon Nanocrystals: Wiley-VCH Verlag GmbH & Co. KGaA*, 2010:1-4.
65. Pavesi L, Dal Negro L, Mazzoleni C, Franzo G, Priolo F. Optical gain in silicon nanocrystals. *Nature* 2000;408(6811): 440-44.
66. Chao Y, Houlton A, Horrocks BR, Hunt MRC, Poolton NRJ, Yang J, Šiller L. Optical luminescence from alkyl-passivated Si nanocrystals under vacuum ultraviolet excitation: Origin and temperature dependence of the blue and orange emissions. *Applied Physics Letters* 2006;88(26): 263119.
67. Dasog M, Yang Z, Regli S, Atkins TM, Faramus A, Singh MP, Muthuswamy E, Kauzlarich SM, Tilley RD, Veinot JG. Chemical insight into the origin of red and blue photoluminescence arising from freestanding silicon nanocrystals. *ACS Nano* 2013;7(3): 2676-85.
68. Fuzell J, Thibert A, Atkins TM, Dasog M, Busby E, Veinot JG, Kauzlarich SM, Larsen DS. Red States versus Blue States in Colloidal Silicon Nanocrystals: Exciton Sequestration into Low-Density Traps. *The Journal of Physical Chemistry Letters* 2013;4(21): 3806-12.

- 
69. Moore D, Krishnamurthy S, Chao Y, Wang Q, Brabazon D, McNally PJ. Characteristics of silicon nanocrystals for photovoltaic applications. *Physica Status Solidi a-Applications and Materials Science* 2011;208(3): 604-07.
70. Alsharif NH, Berger CEM, Varanasi SS, Chao Y, Horrocks BR, Datta HK. Alkyl-Capped Silicon Nanocrystals Lack Cytotoxicity and have Enhanced Intracellular Accumulation in Malignant Cells via Cholesterol-Dependent Endocytosis. *Small* 2009;5(2): 221-28.
71. Nishiguchi K, Oda S. Ballistic transport in silicon vertical transistors. *Journal of Applied Physics* 2002;92(3): 1399-405.
72. Ostraat ML, De Blauwe JW, Green ML, Bell LD, Brongersma ML, Casperson J, Flagan RC, Atwater HA. Synthesis and characterization of aerosol silicon nanocrystal nonvolatile floating-gate memory devices. *Applied Physics Letters* 2001;79(3): 433-35.
73. Wang Q, Ni H, Pietzsch A, Hennies F, Bao Y, Chao Y. Synthesis of water-dispersible photoluminescent silicon nanoparticles and their use in biological fluorescent imaging. *Journal of Nanoparticle Research* 2011;13(1): 405-13.
74. Warner JH, Hoshino A, Yamamoto K, Tilley RD. The synthesis of silicon nanoparticles for biomedical applications. In: Cartwright ANOM, editor. *Nanobiophotonics and Biomedical Applications II*, 2005:52-59.
75. Wang Q, Bao Y, Zhang X, Coxon PR, Jayasooriya UA, Chao Y. Uptake and Toxicity Studies of Poly-Acrylic Acid Functionalized Silicon Nanoparticles in Cultured Mammalian Cells. *Advanced Healthcare Materials* 2012;1: 189-98.
76. Chao Y, Wang Q, Coxon P, Walton A. Evaporation and decomposition of acrylic acid grafted luminescent silicon quantum dots in ultrahigh vacuum. In: Inglesfield JE, editor. *Condensed Matter and Materials Physics Conference*, 2011.
77. Rosso-Vasic M, Spruijt E, Popovic Z, Overgaag K, van Lagen B, Grandidier B, Vanmaekelbergh D, Dominguez-Gutierrez D, De Cola L, Zuilhof H. Amine-terminated silicon nanoparticles: synthesis, optical properties and their use in bioimaging. *Journal of Materials Chemistry* 2009;19(33): 5926-33.
78. Warner JH, Hoshino A, Yamamoto K, Tilley RD. Water-soluble photoluminescent silicon quantum dots. *Angewandte Chemie-International Edition* 2005;44(29): 4550-54.
79. Veinot J. Surface Passivation and Functionalization of Si Nanocrystals. *Silicon Nanocrystals: Wiley-VCH Verlag GmbH & Co. KGaA*, 2010:155-72.

80. Coxon PR, Ahire JH, Ashby SP, Frogley MD, Chao Y. Amine-terminated nanoparticle films: pattern deposition by a simple nanostencilling technique and stability studies under X-ray irradiation. *Physical Chemistry Chemical Physics* 2014;16: 5817-23.
81. Lie LH, Duerdin M, Tuite EM, Houlton A, Horrocks BR. Preparation and characterisation of luminescent alkylated-silicon quantum dots. *Journal of Electroanalytical Chemistry* 2002;538: 183-90.
82. Conibeer G. Applications of Si Nanocrystals in Photovoltaic Solar Cells. *Silicon Nanocrystals: Wiley-VCH Verlag GmbH & Co. KGaA*, 2010:555-82.
83. Cronin BV. Silicon Germanium. *CRC Handbook of Thermoelectrics: CRC Press*, 1995.
84. Crispin DX. Retracted article: Towards Polymer-based Organic Thermoelectric Generators. *Energy & Environmental Science* 2012.
85. Chao Y, Siller L, Krishnamurthy S, Coxon PR, Bangert U, Gass M, Kjeldgaard L, Patole SN, Lie LH, O'Farrell N, Alsop TA, Houlton A, Horrocks BR. Evaporation and deposition of alkyl-capped silicon nanocrystals in ultrahigh vacuum. *Nature Nanotechnology* 2007;2(8): 486-89.
86. Baldwin RK, Pettigrew KA, Ratai E, Augustine MP, Kauzlarich SM. Solution reduction synthesis of surface stabilized silicon nanoparticles. *Chemical Communications* 2002;0(17): 1822-23.
87. Baldwin RK, Pettigrew KA, Garno JC, Power PP, Liu G-y, Kauzlarich SM. Room Temperature Solution Synthesis of Alkyl-Capped Tetrahedral Shaped Silicon Nanocrystals. *Journal of the American Chemical Society* 2002;124(7): 1150-51.
88. Pettigrew KA, Liu Q, Power PP, Kauzlarich SM. Solution synthesis of alkyl- and alkyl/alkoxy-capped silicon nanoparticles via oxidation of Mg(2)Si. *Chemistry of Materials* 2003;15(21): 4005-11.
89. Wilcoxon JP, Samara GA, Provencio PN. Optical and electronic properties of Si nanoclusters synthesized in inverse micelles. *Physical Review B* 1999;60(4): 2704-14.
90. Veinot J. Surface Passivation and Functionalization of Si Nanocrystals. *Silicon Nanocrystals: Wiley-VCH Verlag GmbH & Co. KGaA*, 2010:155-72.
91. Wang J, Sun S, Peng F, Cao L, Sun L. Efficient one-pot synthesis of highly photoluminescent alkyl-functionalised silicon nanocrystals. *Chemical Communications* 2011;47(17): 4941.
92. Ashby S, Thomas J, Coxon P, Bilton M, Brydson R, Pennycook T, Chao Y. The effect of alkyl chain length on the level of capping of silicon nanoparticles produced by a one-pot synthesis route based on the chemical reduction of micelle. *Journal of Nanoparticle Research* 2013;15(2): 1-9.

- 
93. Dung MX, Jeong H-D. Synthesis of Styryl-Terminated Silicon Quantum Dots: Reconsidering the Use of Methanol. *BULLETIN OF THE KOREAN CHEMICAL SOCIETY* 2012;33(12): 4185-87.
94. Neiner D, Chiu HW, Kauzlarich SM. Low-temperature solution route to macroscopic amounts of hydrogen terminated silicon nanoparticles. *Journal of the American Chemical Society* 2006;128(34): 11016-17.
95. Ashby S, García-Cañadas J, Min G, Chao Y. Measurement of Thermoelectric Properties of Phenylacetylene-Capped Silicon Nanoparticles and Their Potential in Fabrication of Thermoelectric Materials. *Journal of Electronic Materials* 2012: 1-4.
96. Shirahata N, Furumi S, Sakka Y. Micro-emulsion synthesis of blue-luminescent silicon nanoparticles stabilized with alkoxy monolayers. *Journal of Crystal Growth* 2009;311(3): 634-37.
97. Veinot JGC. Synthesis, surface functionalization, and properties of freestanding silicon nanocrystals. *Chemical Communications* 2006: 4160-68.
98. Holmes JD, Ziegler KJ, Doty RC, Pell LE, Johnston KP, Korgel BA. Highly luminescent silicon nanocrystals with discrete optical transitions. *Journal of the American Chemical Society* 2001;123(16): 3743-48.
99. English DS, Pell LE, Yu Z, Barbara PF, Korgel BA. Size Tunable Visible Luminescence from Individual Organic Monolayer Stabilized Silicon Nanocrystal Quantum Dots. *Nano Letters* 2002;2(7): 681-85.
100. Li X, He SS, Talukdar SS, Swihart MT. Preparation of luminescent silicon nanoparticles by photothermal aerosol synthesis followed by acid etching. *Phase Transitions* 2004;77(1-2): 131-37.
101. Li X, He Y, Swihart MT. Surface Functionalization of Silicon Nanoparticles Produced by Laser-Driven Pyrolysis of Silane followed by HF-HNO<sub>3</sub> Etching. *Langmuir* 2004;20(11): 4720-27.
102. Kelly JA, Shukaliak AM, Fleischauer MD, Veinot JGC. Size-dependent reactivity in hydrosilylation of silicon nanocrystals. *Journal of the American Chemical Society* 2011;133(46): 19015-6.
103. Belomoin G, Therrien J, Smith A, Rao S, Twesten R, Chaieb S, Nayfeh MH, Wagner L, Mitas L. Observation of a magic discrete family of ultrabright Si nanoparticles. *Applied Physics Letters* 2002;80: 841-43.
104. Bux SK, Blair RG, Gogna PK, Lee H, Chen G, Dresselhaus MS, Kaner RB, Fleurial J-P. Nanostructured Bulk Silicon as an Effective Thermoelectric Material. *Advanced Functional Materials* 2009;19: 2445-52.

105. Heintz AS, Fink MJ, Mitchell BS. Mechanochemical Synthesis of Blue Luminescent Alkyl/Alkenyl-Passivated Silicon Nanoparticles. *Advanced Materials* 2007;19: 3984-88.
106. Ahire JH, Wang Q, Coxon PR, Malhotra G, Brydson R, Chen R, Chao Y. Highly Luminescent and Nontoxic Amine-Capped Nanoparticles from Porous Silicon: Synthesis and Their Use in Biomedical Imaging. *ACS Applied Materials & Interfaces* 2012;4: 3285-92.
107. Veinot JGC. Synthesis, surface functionalization, and properties of freestanding silicon nanocrystals. *Chemical Communications* 2006(40): 4160-68.
108. Buriak JM. Organometallic chemistry on silicon and germanium surfaces. *Chemical Reviews* 2002;102: 1271-308.
109. Warner JH, Hoshino A, Yamamoto K, Tilley RD. Water-soluble photoluminescent silicon quantum dots. *Angewandte Chemie-International Edition* 2005;44: 4550-54.
110. Kelly JA, Shukaliak AM, Fleischauer MD, Veinot JGC. Size-dependent reactivity in hydrosilylation of silicon nanocrystals. *Journal of the American Chemical Society* 2011;133: 19015-16.
111. Sieval AB, van den Hout B, Zuilhof H, Sudholter EJR. Molecular modeling of covalently attached alkyl monolayers on the hydrogen-terminated Si(111) surface. *Langmuir* 2001;17(7): 2172-81.
112. Wallart X, de Villeneuve CH, Allongue P. Truly quantitative XPS characterization of organic monolayers on silicon: Study of alkyl and alkoxy monolayers on H-Si(111). *Journal of the American Chemical Society* 2005;127(21): 7871-78.
113. Bansal A, Li X, Lauermaun I, Lewis NS, Yi SI, Weinberg WH. Alkylation of Si Surfaces Using a Two-Step Halogenation/Grignard Route. *Journal of the American Chemical Society* 1996;118: 7225-26.
114. Baldwin RK, Pettigrew KA, Garno JC, Power PP, Liu G-y, Kauzlarich SM. Room Temperature Solution Synthesis of Alkyl-Capped Tetrahedral Shaped Silicon Nanocrystals. *Journal of the American Chemical Society* 2002;124: 1150-51.
115. He J, Patitsas SN, Preston KF, Wolkow RA, Wayner DDM. Covalent bonding of thiophenes to Si(111) by a halogenation/thienylation route. *Chemical Physics Letters* 1998;286: 508-14.
116. DiSalvo FJ. Thermoelectric Cooling and Power Generation. *Science* 1999;285(5428): 703-06.
117. Rowe DM. General Principles and Basic Considerations. *Thermoelectrics Handbook*: CRC Press, 2005:1-14.



- 
118. Seebeck TJ. Magnetisch polarisation der metalle und erze durch temperatur differenz, . Abh. Akad. Wiss. 1822;1820–1821: 289–346.
119. Oersted HC. Experimenta circa effectum conflictus electrici in acum magneticam. . Typis Schultzianis 1920.
120. Blundell SJ, Blundell KM. Concepts in Thermal Physics. 2nd ed: Oxford University Press, 2009.
121. David MR. Introduction. CRC Handbook of Thermoelectrics: CRC Press, 1995.
122. Peltier CJA. Nouvelles expériences sur la calorité des courants électrique. Annales de Chimie et de Physique, 1834; 56 371-86.
123. Bubnova O, Crispin X. Towards polymer-based organic thermoelectric generators. Energy & Environmental Science 2012;5: 9345-62.
124. Venkatasubramanian R, Siivola E, Colpitts T, O'Quinn B. Thin-film thermoelectric devices with high room-temperature figures of merit. Nature 2001;413: 597-602.
125. Zhu GH, Lee H, Lan YC, Wang XW, Joshi G, Wang DZ, Yang J, Vashaee D, Guilbert H, Pillitteri A, Dresselhaus MS, Chen G, Ren ZF. Increased Phonon Scattering by Nanograins and Point Defects in Nanostructured Silicon with a Low Concentration of Germanium. Physical Review Letters 2009;102: 196803.
126. Bhandari CM. Minimizing the Thermal Conductivity. CRC Handbook of Thermoelectrics: CRC Press, 1995.
127. Chen G, Dames C. Thermal Conductivity of Nanostructured Thermoelectric Materials. Thermoelectrics Handbook: CRC Press, 2005:42-1-42-16.
128. Kanatzidis MG. Nanostructured Thermoelectrics: The New Paradigm?†. Chemistry of Materials 2009;22: 648-59.
129. Dresselhaus MS, Chen G, Tang MY, Yang RG, Lee H, Wang DZ, Ren ZF, Fleurial JP, Gogna P. New Directions for Low-Dimensional Thermoelectric Materials. Advanced Materials 2007;19: 1043-53.
130. Balberg I. Electrical Transport Mechanisms in Ensembles of Silicon Nanocrystallites. Silicon Nanocrystals: Wiley-VCH Verlag GmbH & Co. KGaA, 2010:69-104.
131. Mangolini L, Kortshagen U. Nonthermal Plasma Synthesis of Silicon Nanocrystals. Silicon Nanocrystals: Wiley-VCH Verlag GmbH & Co. KGaA, 2010:309-48.
132. Bansal A, Lewis NS. Stabilization of Si Photoanodes in Aqueous Electrolytes through Surface Alkylation. The Journal of Physical Chemistry B 1998;102: 4058-60.

133. Blundell SJ, Blundell KM. Concepts in Thermal Physics 2009.
134. Minnich AJ, Dresselhaus MS, Ren ZF, Chen G. Bulk nanostructured thermoelectric materials: current research and future prospects. *Energy & Environmental Science* 2009;2: 466-79.
135. Rogl G, Grytsiv A, Melnychenko-Koblyuk N, Bauer E, Laumann S, Rogl P. Compositional dependence of the thermoelectric properties of  $(\text{Sr}_x \text{Ba}_x \text{Yb}_{1-2x})_y \text{Co}_4 \text{Sb}_{12}$  skutterudites. *Journal of Physics: Condensed Matter* 2011;23: 275601.
136. Rogl G, Grytsiv A, Rogl P, Bauer E, Hochenhofer M, Anbalagan R, Mallik RC, Schafler E. Nanostructuring of p- and n-type skutterudites reaching figures of merit of approximately 1.3 and 1.6, respectively. *Acta Materialia* 2014;76: 434-48.
137. Rogl P. Formation and Crystal Chemistry of Clathrates. *Thermoelectrics Handbook*: CRC Press, 2005:32-1-32-24.
138. Rogl G, Aabdin Z, Schafler E, Horky J, Setman D, Zehetbauer M, Kriegisch M, Eibl O, Grytsiv A, Bauer E, Reinecker M, Schranz W, Rogl P. Effect of HPT processing on the structure, thermoelectric and mechanical properties of  $\text{Sr}_{0.07}\text{Ba}_{0.07}\text{Yb}_{0.07}\text{Co}_4\text{Sb}_{12}$ . *Journal of Alloys and Compounds* 2012;537: 183-89.
139. Zaitsev VK, Ktitorov SA, Fedorov MI. Low Carrier Mobility Materials for Thermoelectric Applications. *CRC Handbook of Thermoelectrics*: CRC Press, 1995.
140. Zaitsev VK. Thermoelectric Properties of Anisotropic MnSi. *CRC Handbook of Thermoelectrics*: CRC Press, 1995.
141. Bley RA, Kauzlarich SM, Davis JE, Lee HWH. Characterization of Silicon Nanoparticles Prepared from Porous Silicon. *Chemistry of Materials* 1996;8: 1881-88.
142. Bux SK, Yeung MT, Toberer ES, Snyder GJ, Kaner RB, Fleurial J-P. Mechanochemical synthesis and thermoelectric properties of high quality magnesium silicide. *Journal of Materials Chemistry* 2011;21(33): 12259-66.
143. Binnig G, Rohrer H, Gerber C, Weibel E. Surface Studies by Scanning Tunneling Microscopy. *Physical Review Letters* 1982;49: 57-61.
144. Hochbaum AI, Chen RK, Delgado RD, Liang WJ, Garnett EC, Najarian M, Majumdar A, Yang PD. Enhanced thermoelectric performance of rough silicon nanowires. *Nature* 2008;451: 163-67.
145. Boukai AI, Bunimovich Y, Tahir-Kheli J, Yu JK, Goddard WA, Heath JR. Silicon nanowires as efficient thermoelectric materials. *Nature* 2008;451: 168-71.

- 
146. Peng KQ, Yan YJ, Gao SP, Zhu J. Synthesis of Large-Area Silicon Nanowire Arrays via Self-Assembling Nanoelectrochemistry. *Advanced Materials* 2002;14(16): 1164-67.
147. Assael MJ, Botsios S, Gialou K, Metaxa IN. Thermal Conductivity of Polymethyl Methacrylate (PMMA) and Borosilicate Crown Glass BK7. *International Journal of Thermophysics* 2005;26: 1595-605.
148. Ashby S, Chao Y. Use of Electrochemical Etching to Produce Doped Phenylacetylene Functionalized Particles and Their Thermal Stability. *Journal of Electronic Materials* 2014;43: 2006-10.
149. Ashby S, Thomas JA, Garcia-Canadas J, Min G, Corps J, Powell AV, Xu H, Shen W, Chao Y. FD 176: Bridging Silicon Nanoparticles and Thermoelectrics: Phenylacetylene Functionalization. *Faraday Discussions* 2014.
150. Liu W, Ren Z, Chen G. Nanostructured Thermoelectric Materials. In: Koumoto K, Mori T, editors. *Thermoelectric Nanomaterials*: Springer Berlin Heidelberg, 2013:255-85.
151. Bhandari CM. Thermoelectric Transport Theory. *CRC Handbook of Thermoelectrics*: CRC Press, 1995.
152. Baldwin RK, Zou J, Pettigrew KA, Yeagle GJ, Britt RD, Kauzlarich SM. The preparation of a phosphorus doped silicon film from phosphorus containing silicon nanoparticles. *Chemical Communications* 2006: 658-60.
153. Bubnova O, Khan ZU, Malti A, Braun S, Fahlman M, Berggren M, Crispin X. Optimization of the thermoelectric figure of merit in the conducting polymer poly(3,4-ethylenedioxythiophene). *Nat Mater* 2011;10: 429-33.
154. McCullough RD. The Chemistry of Conducting Polythiophenes. *Advanced Materials* 1998;10: 93-116.
155. Alivisatos AP. Perspectives on the physical chemistry of semiconductor nanocrystals. *Journal of Physical Chemistry* 1996;100: 13226-39.
156. Moore D, Krishnamurthy S, Chao Y, Wang Q, Brabazon D, McNally PJ. Characteristics of silicon nanocrystals for photovoltaic applications. *Physica Status Solidi a-Applications and Materials Science* 2011;208: 604-07.
157. Nogami Y, Kaneko H, Ishiguro T, Takahashi A, Tsukamoto J, Hosoi N. On the metallic states in highly conducting iodine-doped polyacetylene. *Solid State Communications* 1990;76(5): 583-86.

158. Du Y, Shen SZ, Cai K, Casey PS. Research progress on polymer–inorganic thermoelectric nanocomposite materials. *Progress in Polymer Science* 2012;37(6): 820-41.
159. Yan H, Toshima N. Thermoelectric Properties of Alternately Layered Films of Polyaniline and (–)-10-Camphorsulfonic Acid-Doped Polyaniline. *Chemistry Letters* 1999;28(11): 1217-18.
160. Toshima N. Conductive polymers as a new type of thermoelectric material. *Macromolecular Symposia* 2002;186(1): 81-86.
161. Gao X, Uehara K, Klug DD, Patchkovskii S, Tse JS, Tritt TM. Theoretical studies on the thermopower of semiconductors and low-band-gap crystalline polymers. *Physical Review B* 2005;72(12): 125202.
162. Xuan Y, Liu X, Desbief S, Leclère P, Fahlman M, Lazzaroni R, Berggren M, Cornil J, Emin D, Crispin X. Thermoelectric properties of conducting polymers: The case of poly(3-hexylthiophene). *Physical Review B* 2010;82(11): 115454.
163. Milan HC. Calculations of Generator Performance. *CRC Handbook of Thermoelectrics*: CRC Press, 1995.
164. Søndergaard RR, Hösel M, Espinosa N, Jørgensen M, Krebs FC. Practical evaluation of organic polymer thermoelectrics by large-area R2R processing on flexible substrates. *Energy Science & Engineering* 2013;1(2): 81-88.
165. Liu H, Neal AT, Zhu Z, Luo Z, Xu X, Tománek D, Ye PD. Phosphorene: An Unexplored 2D Semiconductor with a High Hole Mobility. *ACS Nano* 2014;8: 4033-41.
166. See KC, Feser JP, Chen CE, Majumdar A, Urban JJ, Segalman RA. Water-Processable Polymer–Nanocrystal Hybrids for Thermoelectrics. *Nano Letters* 2010;10: 4664-67.
167. Zhang B, Sun J, Katz HE, Fang F, Opila RL. Promising Thermoelectric Properties of Commercial PEDOT:PSS Materials and Their Bi<sub>2</sub>Te<sub>3</sub> Powder Composites. *ACS Applied Materials & Interfaces* 2010;2(11): 3170-78.
168. Coxon PR, Ashby SP, Frogley MD, Chao Y. Thermal evaporation and x-ray photostability of dodecyl-passivated silicon nanoparticles. *Journal of Physics D: Applied Physics* 2012;45: 355303.
169. Lie LH, Duerdin M, Tuite EM, Houlton A, Horrocks BR. Preparation and characterisation of luminescent alkylated-silicon quantum dots. *Journal of Electroanalytical Chemistry* 2002;538-539: 183-90.
170. Nishiguchi K, Zhao X, Oda S. Nanocrystalline silicon electron emitter with a high efficiency enhanced by a planarization technique. *Journal of Applied Physics* 2002;92: 2748-57.

- 
171. Mangolini L, Thimsen E, Kortshagen U. High-yield plasma synthesis of luminescent silicon nanocrystals. *Nano Letters* 2005;5: 655-59.
172. Ramirez E, Jansat S, Philippot K, Lecante P, Gomez M, Masdeu-Bultó AM, Chaudret B. Influence of organic ligands on the stabilization of palladium nanoparticles. *Journal of Organometallic Chemistry* 2004;689(24): 4601-10.
173. Zou J, Baldwin RK, Pettigrew KA, Kauzlarich SM. Solution Synthesis of Ultrastable Luminescent Siloxane-Coated Silicon Nanoparticles. *Nano Letters* 2004;4(7): 1181-86.
174. Willard HH, Merritt Jr LL, Dean JA, Settle Jr FA. *Instrumental methods of analysis* 1988.
175. Williams ATR, Winfield SA, Miller JN. Relative fluorescence quantum yields using a computer-controlled luminescence spectrometer. *Analyst* 1983;108(1290): 1067-71.
176. Ashby SP, Thomas JA, Coxon PR, Bilton M, Brydson R, Pennycook TJ, Chao Y. The effect of alkyl chain length on the level of capping of silicon nanoparticles produced by a one-pot synthesis route based on the chemical reduction of micelle. *Journal of Nanoparticle Research* 2013;15: 1-9.
177. Gaal PS, Apostolescu SP. US, 2002.
178. Thermitus M-A, Gaal PS. Proceedings of the 24th International Thermal Conductivity Conference. In: Uher C, Morelli D, editors. 24th International Thermal Conductivity Conference. Lancaster: Technomic Publishing Co., 1997:340.
179. García-Cañadas J, Min G. Multifunctional probes for high-throughput measurement of Seebeck coefficient and electrical conductivity at room temperature. *Review of Scientific Instruments* 2014;85(4): -.
180. Lopenen MT, Taka T, Laakso J, Väkiparta K, Suuronen K, Valkeinen P, Österholm JE. Doping and dedoping processes in poly (3-alkylthiophenes). *Synthetic Metals* 1991;41: 479-84.
181. Wilcoxon JP, Samara GA. Tailorable, visible light emission from silicon nanocrystals. *Applied Physics Letters* 1999;74(21): 3164-66.
182. Pereira RN, Rowe DJ, Anthony RJ, Kortshagen U. Oxidation of freestanding silicon nanocrystals probed with electron spin resonance of interfacial dangling bonds. *Physical Review B* 2011;83: 155327.
183. Pettigrew KA, Liu Q, Power PP, Kauzlarich SM. Solution synthesis of alkyl- and alkyl/alkoxy-capped silicon nanoparticles via oxidation of Mg<sub>2</sub>Si. *Chemistry Of Materials* 2003;15(21): 4005-11.
184. Morales AM, Lieber CM. A Laser Ablation Method for the Synthesis of Crystalline Semiconductor Nanowires. *Science* 1998;279(5348): 208-11.
-

185. Chao Y, Wang Q, Pietzsch A, Hennies F, Ni H. Soft X-ray induced oxidation on acrylic acid grafted luminescent silicon quantum dots in ultrahigh vacuum. *Physica Status Solidi a-Applications and Materials Science* 2011;208(10): 2424-29.
186. Coxon PR, Wang Q, Chao Y. An abrupt switch between the two photoluminescence bands within alkylated silicon nanocrystals. *Journal of Physics D: Applied Physics* 2011;44(49): 495301.
187. Sham TK, Naftel SJ, Kim PSG, Sammynaiken R, Tang YH, Coulthard I, Moewes A, Freeland JW, Hu YF, Lee ST. Electronic structure and optical properties of silicon nanowires: A study using x-ray excited optical luminescence and x-ray emission spectroscopy. *Physical Review B* 2004;70(4): 045313.
188. Holroyd RA, Sham TK. Ion yields in hydrocarbon liquids exposed to x-rays of 5-30-keV energy. *The Journal of Physical Chemistry* 1985;89(13): 2909-13.
189. Šiller L, Krishnamurthy S, Kjeldgaard L, Horrocks BR, Chao Y, Houlton A, Chakraborty AK, Hunt MRC. Core and valence exciton formation in x-ray absorption, x-ray emission and x-ray excited optical luminescence from passivated Si nanocrystals at the Si L<sub>2,3</sub> edge. *Journal of Physics: Condensed Matter* 2009;21(9): 095005.
190. Hu YF, Boukherroub R, Sham TK. Near edge X-ray absorption fine structure spectroscopy of chemically modified porous silicon. *Journal of Electron Spectroscopy and Related Phenomena* 2004;135(2-3): 143-47.
191. Sammynaiken R, Naftel SJ, Sham TK, Cheah KW, Averboukh B, Huber R, Shen YR, Qin GG, Ma ZC, Zong WH. Structure and electronic properties of SiO<sub>2</sub>/Si multilayer superlattices: Si K edge and L<sub>3,2</sub> edge x-ray absorption fine structure study. *Journal of Applied Physics* 2002;92(6): 3000-06.
192. Arinaga K, Rant U, Knežević J, Pringsheim E, Tornow M, Fujita S, Abstreiter G, Yokoyama N. Controlling the surface density of DNA on gold by electrically induced desorption. *Biosensors and Bioelectronics* 2007;23(3): 326-31.
193. Harp GR, Saldin DK, Tonner BP. Finite-size effects and short-range crystalline order in Si and SiO<sub>2</sub> studied by X-ray absorption fine structure spectroscopy. *Journal of Physics: Condensed Matter* 1993;5(31): 5377.
194. Zhou Z, Brus L, Friesner R. Electronic Structure and Luminescence of 1.1- and 1.4-nm Silicon Nanocrystals: Oxide Shell versus Hydrogen Passivation. *Nano Letters* 2003;3(2): 163-67.
195. Dickinson FM, Alsop TA, Al-Sharif N, Berger CEM, Datta HK, Šiller L, Chao Y, Tuite EM, Houlton A, Horrocks BR. Dispersions of alkyl-capped silicon nanocrystals in aqueous media: photoluminescence and ageing. *Analyst* 2008;133(11): 1573-80.

- 
196. Terry J, Linford MR, Wigren C, Cao R, Pianetta P, Chidsey CED. Alkyl-terminated Si(111) surfaces: A high-resolution, core level photoelectron spectroscopy study. *Journal of Applied Physics* 1999;85(1): 213-21.
197. Lehmann V, Hofmann F, Möller F, Grüning U. Resistivity of porous silicon: a surface effect. *Thin Solid Films* 1995;255(1–2): 20-22.
198. Anatyckuk LI. Thermoelectrically Cooled Radiation Detectors. *CRC Handbook of Thermoelectrics*: CRC Press, 1995.
199. Boyer A, Cisse E. PROPERTIES OF THIN-FILM THERMOELECTRIC-MATERIALS - APPLICATION TO SENSORS USING THE SEEBECK EFFECT. *Materials Science and Engineering B-Solid State Materials for Advanced Technology* 1992;13: 103-11.
200. Coxon PR, Ashby SP, Frogley MD, Chao Y. Thermal evaporation and x-ray photostability of dodecyl-passivated silicon nanoparticles. *Journal of Physics D: Applied Physics* 2012;45(35): 355303.
201. Aroutiounian VM, Ghulinyan MZ. Electrical conductivity mechanisms in porous silicon. *physica status solidi (a)* 2003;197(2): 462-66.
202. Bux SK, Yeung MT, Toberer ES, Snyder GJ, Kaner RB, Fleurial J-P. Mechanochemical synthesis and thermoelectric properties of high quality magnesium silicide. *Journal of Materials Chemistry* 2011;21: 12259-66.
203. Klemens PG. Thermal conductivity of inhomogeneous media. *High Temperatures - High Pressures* 1991;23: 241-48.
204. Schlichting KW, Padture NP, Klemens PG. Thermal conductivity of dense and porous yttria-stabilized zirconia. *Journal of Materials Science* 2001;36(12): 3003-10.
205. Nishiguchi K, Oda S. Electron transport in a single silicon quantum structure using a vertical silicon probe. *Journal of Applied Physics* 2000;88: 4186-90.
206. Nishida IA. Measurements of Electrical Properties. *CRC Handbook of Thermoelectrics*: CRC Press, 1995.
207. Neiner D, Chiu HW, Kauzlarich SM. Low-temperature solution route to macroscopic amounts of hydrogen terminated silicon nanoparticles. *Journal of the American Chemical Society* 2006;128: 11016-17.
208. Nair RR, Blake P, Grigorenko AN, Novoselov KS, Booth TJ, Stauber T, Peres NMR, Geim AK. Fine Structure Constant Defines Visual Transparency of Graphene. *Science* 2008;320: 1308.

209. Liu W, Ren Z, Chen G. Nanostructured Thermoelectric Materials. In: Koumoto K, Mori T, editors. Thermoelectric Nanomaterials: Springer Berlin Heidelberg, 2013:255-85.
210. Connelly NG, Geiger WE. Chemical Redox Agents for Organometallic Chemistry. *Chemical Reviews* 1996;96(2): 877-910.
211. Chicart P, Corriu RJP, Moreau JJE, Garnier F, Yassar A. Selective synthetic routes to electroconductive organosilicon polymers containing thiophene units. *Chemistry of Materials* 1991;3: 8-10.
212. Bartuš J. Electrically Conducting Thiophene Polymers. *Journal of Macromolecular Science: Part A - Chemistry* 1991;28: 917-24.
213. Peulon V, Barbey G, Malandain J-J. Influence of doping anion on electrochemical and physical properties of polyselenienyl thiophene polymer. *Synthetic Metals* 1996;82(2): 111-17.
214. Zotti G. Doping-level dependence of conductivity in polypyrroles and polythiophenes. *Synthetic Metals* 1998;97(3): 267-72.
215. Brie M, Turcu R, Mihut A. Stability study of conducting polypyrrole films and polyvinylchloride-polypyrrole composites doped with different counterions. *Materials Chemistry and Physics* 1997;49(2): 174-78.
216. Wang Y, Levon K. Influence of Dopant on Electroactivity of Polyaniline. *Macromolecular Symposia* 2012;317-318(1): 240-47.
217. Shinohara Y, Imai Y, Isoda Y, Hiraishi K, Nakanishi H. A new challenge of polymer thermoelectric materials as ecomaterials. *Materials Science Forum*, 2007:2329-32.
218. Pintér E, Fekete ZA, Berkesi O, Makra P, Patzkó Á, Visy C. Characterization of Poly(3-octylthiophene)/Silver Nanocomposites Prepared by Solution Doping. *The Journal of Physical Chemistry C* 2007;111(32): 11872-78.
219. Yan H, Toshima N. Thermoelectric Properties of Alternately Layered Films of Polyaniline and (&plusmn;)-10-Camphorsulfonic Acid-Doped Polyaniline. *Chemistry Letters* 1999;28: 1217-18.
220. Du Y, Shen SZ, Cai K, Casey PS. Research progress on polymer-inorganic thermoelectric nanocomposite materials. *Progress in Polymer Science* 2012;37: 820-41.
221. Bahl SK, Chopra KL. Electrical and Optical Properties of Amorphous vs Crystalline GeTe Films. *Journal of Vacuum Science & Technology* 1969;6(4): 561-65.



222. Baldwin RK, Zou J, Pettigrew KA, Yeagle GJ, Britt RD, Kauzlarich SM. The preparation of a phosphorus doped silicon film from phosphorus containing silicon nanoparticles. *Chemical Communications* 2006(6): 658-60.
223. Švrček V, Rehspringer JL, Gaffet E, Slaoui A, Muller JC. Unaggregated silicon nanocrystals obtained by ball milling. *Journal of Crystal Growth* 2005;275(3–4): 589-97.
224. Burkov AT, Vedernikov MV. Thermoelectric Properties of Metallic Materials. *CRC Handbook of Thermoelectrics*: CRC Press, 1995.
225. Mawhinney DB, Glass JA, Yates JT. FTIR Study of the Oxidation of Porous Silicon. *The Journal of Physical Chemistry B* 1997;101(7): 1202-06.
226. Wang Y, Liu J, Zhou J, Yang R. Thermoelectric Transport Across Nanoscale Polymer–Semiconductor–Polymer Junctions. *The Journal of Physical Chemistry C* 2013;117: 24716-25.

